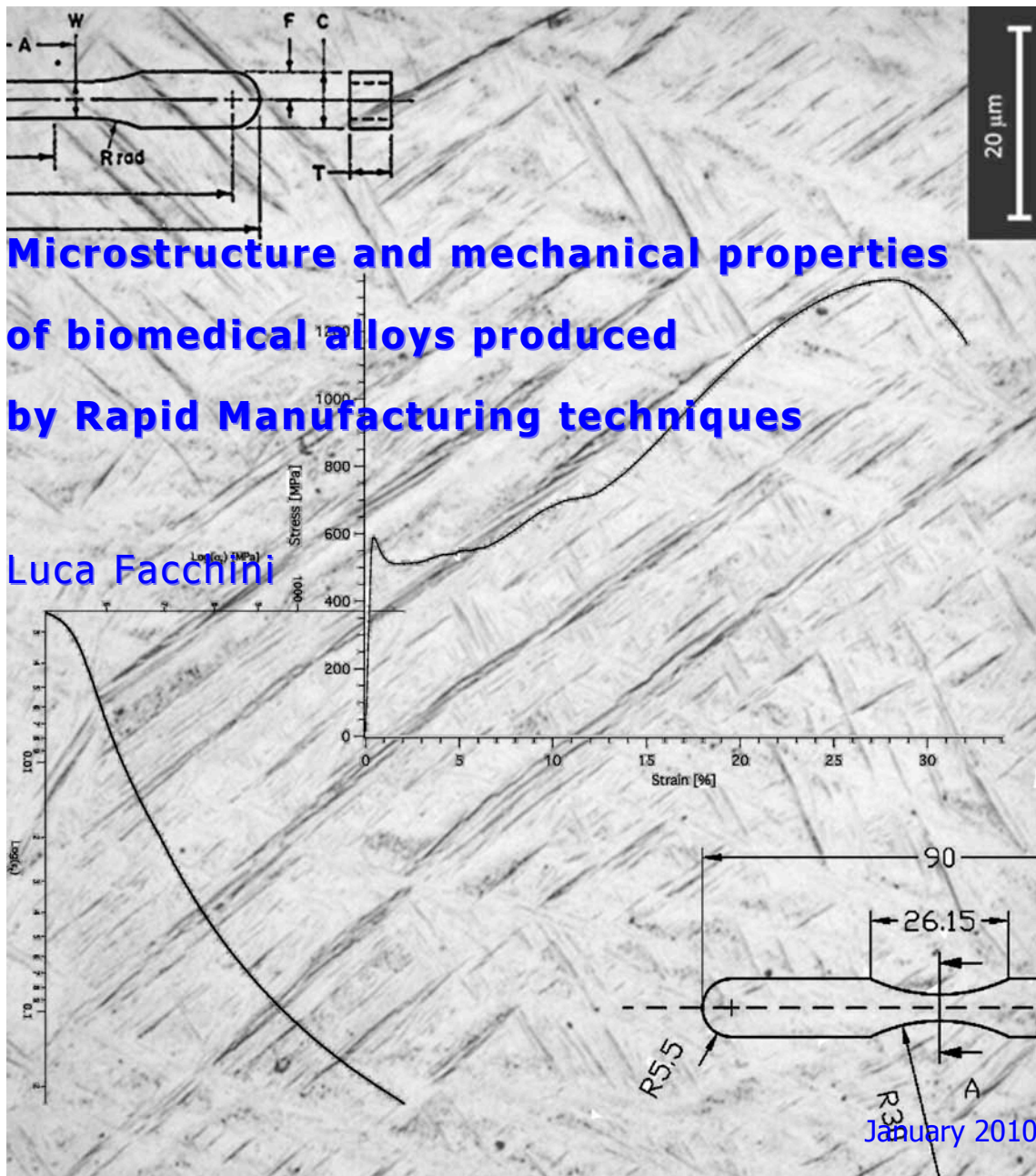




UNIVERSITY  
OF TRENTO - Italy

Department of Materials Engineering  
and Industrial Technologies

Doctoral School in Materials Engineering – XXII cycle





Doctoral thesis

**Microstructure and mechanical properties  
of biomedical alloys produced  
by Rapid Manufacturing technologies**

Luca Facchini

Tutor: Prof. Ing. Alberto Molinari

*Doctoral Committee:*

*Prof. Alberto Molinari, Università degli Studi di Trento, Italy (President)*

*Prof. Marjorie Olivier, Faculté Polytechnique de Mons, Belgium*

*Prof. Nikolaos E. Zafeiropoulos, University of Ioannina, Greece*

Date of dissertation: January 21st, 2010



*to the memory of Giulia*



# Index

## Introduction

### Chapter 1: Rapid Manufacturing technologies

1.1 The technologies: an overview.....	3
1.2 Going to a fully dense material: the process parameters.....	6
1.3 Incomplete homologous wetting and balling.....	6
1.4 Vaporization and volatilization.....	8
1.5 Epitaxial solidification.....	12
1.6 Fine grains.....	13
1.7 Scanning strategy.....	14
1.8 Selective Laser Melting.....	15
1.9 Electron Beam Melting.....	17

## Chapter 2: The materials

2.1 Metallic powder for Rapid Manufacturing.....	21
2.2 Ti-6Al-4V alloy.....	22
2.2.1 <i>Ti-6Al-4V alloy: microstructure.....</i>	23
2.2.2 <i>Ti-6Al-4V alloy: mechanical properties.....</i>	27
2.2.3 <i>Ti-6Al-4V alloy: application and corresponding required properties.....</i>	30
2.3 ASTM F75 alloy.....	30
2.3.1 <i>ASTM F75 alloy: microstructure.....</i>	31
2.3.2 <i>ASTM F75 alloy: mechanical properties.....</i>	33
2.3.3 <i>ASTM F75 alloy: application and corresponding required properties.....</i>	36
2.4 17-4 PH Stainless Steel.....	37
2.4.1 17-4 PH Stainless Steel: microstructure.....	38
2.4.2 17-4 PH Stainless Steel: mechanical properties.....	39
2.4.3 <i>17-4 PH Stainless Steel: application and corresponding required properties.....</i>	45

## Chapter 3: Requirements for the application

3.1 The biomedical standards.....	48
3.2 Requirements on chemical composition.....	49

3.3. Requirements on mechanical properties.....	50
3.3.1 ISO 5832-3 standard for Ti-6Al4V alloy.....	50
3.3.2 ISO 5832-4 standard for ASTM F75 alloy.....	51
3.3.3 ASTM A564-02 standard for 17-4 PH Stainless Steel.....	52
3.4 Microstructure.....	52
3.5 Density of the alloys produced by Rapid Manufacturing techniques.....	54

#### **Chapter 4: Materials and experimental procedures**

4.1 Powders.....	55
4.2 Process parameters.....	57
4.3 Microhardness and hardness.....	58
4.4 Light Optical Microscopy (LOM) .....	58
4.5 Scanning Electron Microscopy (SEM) and Transmission Electron Microscopy (TEM) .....	59
4.6 Differential Scanning Calorimetry (DSC) .....	60
4.7 Dilatometry.....	60
4.8 Heat treatments.....	61
4.9 X-Ray Diffraction (XRD) and neutron diffraction spectroscopy (SMARTS) .....	61
4.10 Tensile testing.....	63

4.11 Fatigue testing.....	64
4.12 Density.....	65

**Chapter 5: Ti-6Al-4V in Rapid Manufacturing**

5.1 Microstructures.....	67
5.2 Mechanical properties of the as-built material.....	74
5.2.1 Tensile properties.....	74
5.2.2 Fatigue behaviour of the as-built materials.....	83
5.3 Thermal stability of the microstructures.....	84
5.3.1 Microstructural thermal stability of Ti-6Al-4V produced by Selective Laser Melting.....	85
5.3.2 Microstructural thermal stability of Ti-6Al-4V produced by Electron Beam Melting.....	93
5.4 Final remarks.....	104

**Chapter 6: ASTM F75 alloy produced by Electron Beam Melting**

6.1 Microstructures.....	106
6.2 Mechanical properties of the as-built and hipped materials.....	113
6.2.1 Tensile properties.....	114
6.2.2 Fatigue properties.....	117

6.3 Modification on heating of the as-built micro-structure and related mechanical properties.....	119
6.3.1 Phase transformations on heating and solution treatment on the as-built material.....	119
6.3.2 Partial solution treatment on the as-built material.....	131
6.4 Final remarks.....	142

**Chapter 7: 17-4 PH Stainless Steel produced by Selective Laser Melting**

7.1 Microstructure.....	145
7.2 Hardness and tensile properties.....	154
7.3 Final remarks.....	166

**Conclusions**

On Ti-6Al-4V alloy.....	168
On ASTM F75 alloy.....	170
On 17-4 PH Stainless Steel.....	171



# Introduction

Three years ago, Eurocoating s.p.a., a company specialized in the plasma spray coating process applied to biomedical prostheses, started to spread its interests on the production of the prostheses themselves. The project was ambitious. The biomedical industry, in fact, is a demanding field, for several reasons. First of all, the employed materials must satisfy careful and close requirements concerning mechanical properties and corrosion resistance in the biological environment. Biocompatibility is indeed a complex issue. The concept of biological and chemical inertness is overtaken: at the present time, the implanted material is not simply called for it. The implanted material has to interact and communicate with the human body, favouring the integration of the prosthesis. Then, the task of the producer is not trivial: the functionalization of the surfaces has acquired a fundamental role. Such a surface engineering can follow a biological way (i.e., the tissue engineering involving proteins and cell implants) or a geometrical way (i.e., the creation of an interconnected porosity that allows the human cells to adhere and tissues to grow on the implant). Eurocoating s.p.a. chose to embark on the route of the geometrical functionalization of the prosthesis surface. Consistently, two Rapid Manufacturing (RM) machines were acquired. They allow complex shapes to be formed directly from 3D models, in a layer-wise process. In particular, these technologies are able to produce an interconnected porosity, with definite size and distribution, on the surface of the parts. Hence, they are suitable for the production of implants and, in particular, for the manufacturing of stems and acetabular cups for hip prostheses. Nevertheless, because of their ability to reproduce 3D models in a fast near-net shape way, the Rapid Manufacturing techniques are also fit for the purpose of producing other biomedical parts, such as knee prostheses and dental screws.

---

The Rapid Manufacturing techniques are quite new and have had a recent significant development. On the other hand, the metallic alloys used in the biomedical field have a long history and are well-known. Usually, they are alloys lent by other application fields, e.g. the aeronautical field. They are commonly produced by casting or by hot working, and are characterized by well-known properties. This is the starting point for the present Ph.D. thesis work. The biomedical metallic alloys produced by the employment of Rapid Manufacturing technologies, in fact, result to have very peculiar features. Because of the large undercoolings intrinsic of the processes, the materials present very fine microstructures. In certain cases, these microstructures are metastable. Furthermore, such peculiar microstructures are associated to distinctive mechanical properties.

As stated above, nevertheless, the biomedical field has definite restrictions. These can regard tensile properties as well as microstructural morphologies. The metallic alloys produced with the aim of implanting them in the human body, then, undergo a strict control. From the point of view of the material soundness, the problem is not put. If the process parameters are properly adjusted, in fact, the alloys result to have full density. Better, the question concerns microstructures and ductility. In several cases, the former do not match the standard prescriptions; the latter, on the other hand, often result unfit for practical application. Consequently, customers' requirements are disappointed. This is associated, furthermore, to a lacking in literature about the microstructural characteristics of these alloys and their mechanical behaviour.

The demanding purpose of the present Ph.D. thesis work has then been the investigation of the peculiar as-built materials and the study of their possible modification by heat treatment.

In the first two chapters of this thesis, an account of the Rapid Manufacturing processes (i.e., Electron Beam Melting and Selective Laser Melting) and the involved metallic alloys will be provided. Afterwards, an overview of the requirements for the biomedical application will be given in Chapter 3. After a brief description of the employed metallic powders and the experimental procedures, then, the attention will be concentrated on three different chapters concerning Ti-6Al-4V alloy, ASTM F75 cobalt alloy and 17-4 PH Stainless Steel produced by RM techniques.

# Chapter 1

## Rapid Manufacturing technologies

### 1.1 The technologies: an overview

In the last few years, Rapid Prototyping (RP) technologies have vastly spread in different fields of application. “Rapid Prototyping” means the production of prototypes or simulacra in a one-step process; the rapidity of the process is due to the possibility to obtain near-net shape objects directly from virtual models.

More recently, RP has become Rapid Manufacturing (RM), since the techniques previously used in the production of prototypes are being industrially employed for the mass production.

Beyond the differences from process to process, these technologies are mainly joined by the same assumption: the production of fully dense, complex shaped parts starting from powders.

The second important characteristic of these techniques, if nothing as if else for biomedical applications, is the possibility to create complex networks with open and interconnected porosity [1-6], both in the core material and onto the surface (Fig. 1.1).

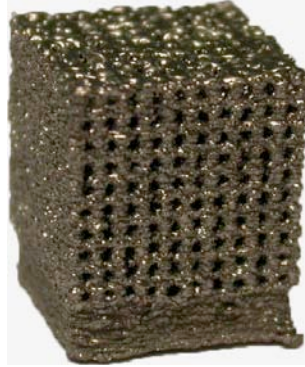


*Figure 1.1. Example of controlled interconnected porosity produced by Electron Beam Melting of Ti-6Al-4V alloy.*

Starting from the consideration that human bones have an elastic modulus much smaller than those typical of metals, advantages in having a trabecular structure instead of a bulk one are evident. In fact, the wide difference between the elastic moduli makes the load distribution unhomogeneous, because the largest part is borne by the prosthesis. As a consequence, the bone is unloaded and this can be responsible of bone resorption. A trabecular structure reduces the prosthesis stiffness, and then preserves loading on the bone.

Another important issue regarding metallic prostheses is cell adhesion. Since a few years, tissue engineering is studying interactions between human cells and implanted substrates. Whilst some time ago chemical and biological inertness was considered the only requirement for prostheses, today functionalization of the surfaces is recognized to be of big assistance for implant success. From this point of view, RM is a very versatile and useful technology, allowing the production of porous surfaces with an interconnected porosity suitable for cell adhesion.

From a technological point of view, some common steps associate the whole different RM technologies.

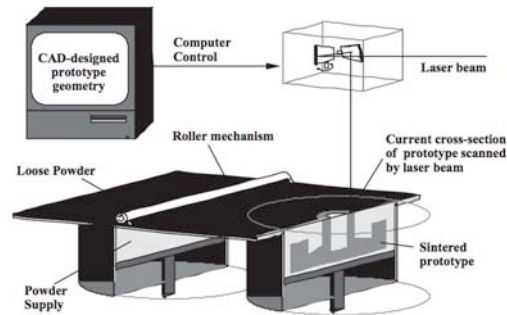


Figure 1.2. Example: sequence of production by Rapid Manufacturing [3].

At first, 3D CAD design of the part is separately drawn through a CAD (Computer Aided Design) software (Fig. 1.2). Then, the management software of the RM machine divides the design in several layers with a thickness of a few tens of microns, varying depending on the technology. Each layer will be locally melted in a powder bed, making the object grow up layer by layer.

In biomedical applications, the 3D CAD model can be borrowed directly from Computed Axial Tomography (CAT) and Nuclear Magnetic Resonance (NMR).

The first step of the technological process is then the spreading of a powder bed on a working plate by mean of a mobile rake. The delicacy of this step consists in the uniformity of the bed, important for the proper melting of the layer and for the preservation of the rake, which can be damaged in presence of not controlled harshness.

After spreading, a laser beam or an electron beam provides the energy for the consolidation of the powder: passing on the bed at a constant speed, it locally melts the powder. Working in a substantially cold chamber, a quick solidification, with large undercooling, follows.

Then the working plate is lowered on a piston of a distance equal to a layer thickness: another powder bed is spread and the melting process goes on.

The deflection of the beam is accomplished by electromagnetic (in the case of EBM) or optical (in the case of SLM) lenses, resulting in high scanning speed and spotting accuracy.

---

## 1.2 Going to a fully dense material: the process parameters

The production of a fully dense material (except for the porous surface layers, when needed) goes through the proper combination of the four main process parameters: the power of the energy source ( $P$ ), the scan speed ( $v$ ), the distance between every single scan (hatch distance,  $d$ ) and the thickness of the single layer ( $l$ ) using a fixed beam diameter. These four parameters are related to the specific energy input (the total energy input per volume of each melted track) through the following equation [7,8]:

$$\psi = \frac{P}{vdl}$$

Some observations are immediate. First of all, the layer thickness has to be opportunely chosen in order to allow the complete melting of the powder bed. The same is worth for the hatch distance and the scan speed. Processes in which low powers are used must necessary be slower to warrant the full density of the material.

## 1.3 Incomplete homologous wetting and balling

The energy involved in the process is related to a phenomenon called “incomplete homologous wetting”, which can strongly affect the soundness of the produced part. The phenomenon is describable as follows.

First of all, we have to start from the consideration that in Rapid Manufacturing of metals, where generally high temperatures are reached in order to melt the powder, oxidation can easily occur, especially on the surface of very reactive alloys. As afterwards discussed, oxidation represents a serious problem in terms of interlayer bonding and melting defects.

The concept of “homologous wetting”, on its own, is introduced when a molten material has to wet a substrate of the same solid material; it involves simultaneously

fluid flow (by spreading), heat transfer to the solid bulk and rapid solidification [9]. As a liquid droplet spreads on a metallic substrate with a dynamic contact angle  $\theta_a$ , a solidification front grows with a dynamic angle  $\theta_s$  which is lower than  $\theta_a$ . When the two angles coincide, spreading stops. Furthermore, the critical angle of contact (where  $\theta_a$  and  $\theta_s$  coincide) is a function of the Stefan number ( $S$ ),

$$S = c \frac{T_f - T_t}{L}$$

where  $T_f$  is the temperature of the fusion front,  $T_t$  is the temperature of the subcooled solid substrate,  $c$  is the specific heat and  $L$  is the latent heat of fusion. Moreover, the spreading behaviour of the molten metal accords the Tanner law,

$$Ca = \frac{\mu U}{\gamma}$$

where  $Ca$  is the Capillary number,  $\mu$  is the viscosity,  $U$  is the spreading velocity and  $\gamma$  is the surface tension.

If an oxide layer is present, wetting is not optimal. Poor wetting of an oxide substrate by a liquid metal can be explained in terms of interfacial energies. The equilibrium between liquid, solid and gaseous phases is represented, for such short interaction times, by the equation of Young for the contact angle:

$$\gamma_{SG} - \gamma_{SL} = \gamma_{LG} \cos(\theta)$$

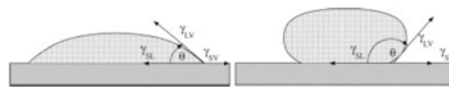


Figure 1.3. Equilibrium between liquid, solid and gaseous phases at different surface free energies.

Since surface free energies of solid metal oxides are much lower than the liquid and gaseous ones, the contact angle increases: the liquid metal does not properly wet the oxide surface (Fig. 1.3). As a consequence, defects can form between layers. If the

poor wetting is carried to extreme end, it results in a phenomenon called “balling”. It consists in the formation of spherical particles: the surface tension makes the contact angle as high as it drive the wettability to zero [10,11]. From a geometrical point of view, J.P. Kruth et al. [10] suggest to approximate the molten pool by a half cylinder (Fig. 1.4). When the total surface of the half-cylindrical molten pool exceeds that of a sphere with the same volume, balling takes place, because spherical shape becomes favoured. The result is a rough and bead-shaped surface, which can make difficult the deposition of a smooth layer and then cause defects.

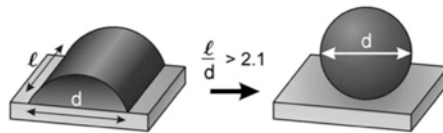


Figure 1.4. Approximation of the molten pool by a half cylinder.

The control of the working chamber atmosphere can reduce the probability of the oxide to form. In order to prevent poor wetting, anyhow, the crucial issue is remelting. In fact, partial remelting of the just consolidated layer (Fig. 1.5) seems to be necessary to ensure full density of the part: it can break down the surface oxide and assist the contact between liquid and solid.

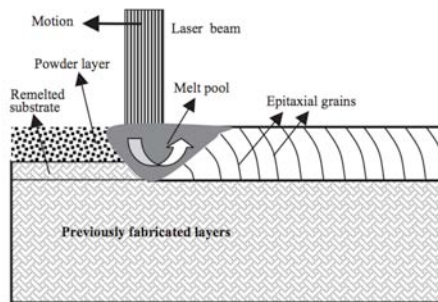


Figure 1.5. Melting procedure during Rapid Manufacturing [8].

## 1.4 Vaporization and volatilization

In RM technologies, an incident beam makes the temperature raise above the melting point in a very short time; the control of the reached temperature is difficult and sometimes not precisely recognizable. If the temperature of the powder particles increases well above the melting temperature, the material can evaporate. The rapidly moving evaporated material expand and generate a recoil pressure on the molten pool. This pressure can flatten the melt and make the surface to be less rough, but if it is too high can cause material removal by volatilization.

The evaporation of metal from the melt pool in RM takes place in four steps: (i) mass transport of atoms in the melt, (ii) phase transformation at the surface, (iii) mass transport in the gaseous phase and (iv) condensation.

The evaporation of a pure liquid metal in equilibrium with its vapour is subordinated to the Hertz-Knudsen equation [12]; applied to the vaporization from free solid surfaces, the maximum vaporization rate ( $\Gamma$ ) takes the form of Langmuir equation,

$$\Gamma = \sqrt{\frac{m}{2\pi kT}} P_v$$

where  $m$  is the mass of an individual atom/molecule,  $k$  is the Boltzmann constant,  $T$  is the absolute temperature and  $P_v$  is the vapour pressure at the liquid's surface temperature.

If the latent heat of vaporization can be assumed constant, the integration of the Clausius-Clapeyron equation furnishes the relation for  $P_v$ ; the previous equation then assumes the form

$$\Gamma = P_0 \sqrt{\frac{m}{2\pi kT}} e^{\frac{-L}{RT}}$$

where  $P_0$  is the limit value at 0 K for the vapour pressure,  $L$  is the molar latent heat of vaporization and  $R$  is the molar gas constant.

Concerning alloys, mass transport of the solute from the bulk of the melted metal to the surface has to be considered in addition to evaporation from the surface. As a

---

consequence, the rate limiting step comes from one of the two mechanisms. The flux of solute to the surface is regulated by

$$j_A = \sqrt{2 \frac{D}{\pi \theta}} (C_{A,\infty} - C_A^s) = k_{m,l} (C_{A,\infty} - C_A^s)$$

where  $D$  is the diffusion coefficient of the solute in the liquid,  $\theta$  is a fictitious “resident time” calculated from the ratio between the melt pool characteristic length and the surface velocity of the flowing melted metal,  $C_{A,\infty}$  is the volumetric concentration of the solute in the bulk and  $C_A^s$  is the volumetric concentration of the solute at the surface. The term  $k_{m,l}$  is the average mass transfer coefficient in a stirred melted metal.

The evaporation flux of an alloying element in an alloy is given by

$$j_A = \frac{\gamma_A P_A^0 C_A^s}{\rho \sqrt{2\pi M R T}} = k_{m,e} C_A^s$$

where  $\gamma_A$  is the activity coefficient of the element,  $P_A^0$  is the vapour pressure of the pure element at the considered temperature,  $\rho$  is the molar density of the alloy and  $M$  is the alloy’s molecular weight.

Langmuir demonstrated that, for low pressures, the resistance to mass transport in the gaseous phase is negligible, and so the two fluxes are in equilibrium:

$$k_{m,l} (C_{A,\infty} - C_A^s) = k_{m,e} C_A^s$$

and then, substituting  $C_A^s$ , the flux results to be

$$j_A = \frac{k_{m,l} k_{m,e}}{k_{m,l} + k_{m,e}} C_{A,\infty}$$

So, the limiting step depends on the two factors  $1/k_{m,l}$  and  $1/k_{m,e}$ . If the stirring effect is appreciable,  $k_{m,l}$  is high and then the mass transfer rate has a small effect; on

the other hand,  $k_{m,e}$  becomes considerable when the value of  $P_A^0$  is high.

As an approximation, based on a very conservative estimate of the flow velocity at the pool surface, the stirring in SLM is about ten times the stirring in EBM (which has a value in the order of the one expected in a inductively stirred melt). The beam scan speed is assumed to be representative of the surface velocity in the melt pool, while the beam diameter is comparable to the melt pool size.

The volatilization of alloying elements from the melted metal can be cause of a lowering in the beam power; this power loss can be quantified by

$$P_{L,A} = \Gamma_A(L_A - \Delta H_A)$$

where  $P_{L,A}$  is the power lost because of the evaporation of element A,  $\Gamma_A$  is the evaporation rate of element A,  $L_A$  is the latent heat of evaporation of A and  $\Delta H_A$  is the partial molar heat of mixing of A in the alloy.

Since generally in a vacuum range between  $10^{-6}$  bar and  $10^{-5}$  bar the vaporization temperature is comparable with the melting point, many elements can evaporate; the worse effect of this phenomenon is the condensation of the volatile elements on the cool surfaces of the chamber and particularly on the optical system. Furthermore, a secondary negative effect of volatilization is the depletion of the alloying components in the solidified part.

The mean free path of the volatilized gaseous molecules ( $\lambda$ ) is defined as the average distance between subsequent collisions, and is represented by

$$\lambda = \frac{kT}{\sqrt{2}P\pi\sigma^2}$$

where  $k$  is the Boltzmann constant,  $T$  is the absolute temperature,  $P$  is the pressure and  $\sigma$  is the molecular diameter. Collisions create a barrier that inhibits the condensation of the volatile elements on the cool parts.

Considering reasonable values of these parameters, the mean free path results to be comparable with the chamber dimensions only for pressures above  $10^{-8}$  bar. Pressures above  $10^{-5}$  bar generally make the mean free path two orders of magnitude lower than the chamber dimensions, substantially reducing the condensation on the cool surfaces. For this reason, a partial pressure can be applied at the work chamber instead of high

---

vacuum. In fact, RM technologies such as SLM work in purged atmosphere, with a partial pressure of highly pure inert gas. If the partial pressure is dynamic, under flowing gas, volatile elements can be removed from the chamber. The same is not true for EBM, which works in high vacuum; however, the problem of condensation is less critical because no glass lenses are present.

## 1.5 Epitaxial solidification

An other implication of remelting, or “meltback”, concerns the grain growth occurring, during solidification of a new layer, at the interface between solid and molten metal. Solidification is epitaxial, through a mechanism of heterogeneous nucleation.

Das [9] furnished an approach at the subject from the point of view of free energies. Retrieving the equation of Young, the balance of interfacial forces between the substrate, the solid nucleus and the liquid becomes

$$\gamma_{ML} = \gamma_{NM} + \gamma_{NL} \cos(\psi)$$

where  $\gamma_{ML}$  is the free energy between the metallic substrate and the liquid,  $\gamma_{NM}$  is the free energy between the nucleus and the metallic substrate and  $\gamma_{NL}$  is the free energy between the solid nucleus and the liquid, while  $\psi$  is the contact angle of the nucleus.

The solid nucleus and the substrate have the same composition, and then the interfacial energy between them is negligible, while the interfacial energies between both of them and the liquid should be about the same.

So,  $\psi$  results to be about 0.

The formation of the solid nucleus is associated with a change in free energy represented by

$$\Delta G_{het} = S(\psi) \left[ -\frac{4}{3} \pi r^3 \Delta G_v + 4 \pi r^2 \gamma_{SL} \right]$$

where  $r$  is the radius of the nucleus,  $\Delta G_v$  is the free energy change per unit volume

and  $S(\psi)$  is a shape factor dependent on the contact angle,

$$S(\psi) = \frac{[2 + \cos(\psi)][1 - \cos(\psi)]^2}{4}$$

The critical radius to favour a heterogeneous nucleation,  $r^*$ , results by setting equal to 0 the differentiation of the previous equation for change in free energy; it is

$$r^* = \frac{2\gamma_{SL}}{\Delta G_v}$$

and then, putting it into the previous equation,

$$\Delta G_{het}^* = \frac{16\pi}{3} \frac{\gamma_{SL}^3}{\Delta G_v^3} S(\psi)$$

It is then evident that in epitaxial solidification, where  $\psi$  is about 0,  $S(\psi) \rightarrow 0$  and then the energy barrier for heterogeneous nucleation is small.

As a consequence, epitaxial solidification is favoured in processes like SLM and EBM. The partial remelting of the substrate, then, can promote epitaxial growth from the prior grains, such as in the production of monolithic silicon for electronic applications. This can also cause a microstructural anisotropy.

## 1.6 Fine grains

Epitaxial solidification results as well in fine grain size.

As previously said, the critical radius of the nucleus  $r^*$  depends on the interfacial free energy between solid and liquid. Starting from the consideration that solid and liquid in Rapid Manufacturing have almost the same composition (neglecting contamination and segregation),  $\gamma_{SL}$  is very small. As a consequence,  $r^*$  is very small.

Therefore, under identical processing conditions (e.g. temperature gradients, cooling rates...) the material coming from Rapid Manufacturing processes has a finer grain in comparison with conventional casting.

---

## 1.7 Scanning strategy

Thermal deformations during RM involve different mechanisms [10].

First of all, the Temperature Gradient Mechanism (TGM). It results from the large thermal gradients that spring in the area of the laser spot. The very rapid heating of the top layer, combined with a rather slow heat conduction, is the cause of the temperature gradient. The expansion of the heated top layer is obstructed by the cool underlying material, resulting in compressive strain in the layer. The compression becomes plastic when the material reaches and exceeds its yield stress; then, on cooling the plastically strained area shrinks, becomes shorter than the bottom material and makes the part bending towards the laser beam (Fig. 1.6). The solidified layers of the part are subjected to such a mechanism each time a new powder layer is melted.

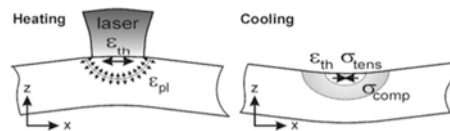


Figure 1.6. Obstructed expansion of the heated top layer and part bending on cooling.

Moreover, the shrinkage of the molten pool during cooling adds additional tensile stresses on top of the layers underneath, supporting in its turn the bending towards the beam. The molten top layer tends to shrink during cooling, but the shrinkage is inhibited by the underlying bulk. As a result, the top layer undergoes a tensile stress, while the previously solidified material is subjected to compressive stress.

Another source of internal stress is the difference of processing temperature in the part related to the geometry of the part itself and the scan strategy employed. Concerning this, the dimension of the area to be scanned is crucial for two reasons. Since the layers are scanned with vectors parallel to each other, if the area to be scanned is small adjacent vectors are scanned rapidly; this results in little cool down time between scans, and then in a higher temperature. Moreover, small scanning areas are surrounded by more loose powder, and then the heat sink is less. As a consequence of both these considerations, the thermal gradient is reduced.

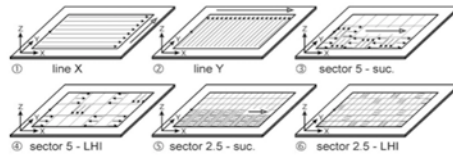


Figure 1.7. Examples of different scanning strategies.

Kruth et al. [10] scanned some specimens with different strategies, in order to investigate their different deflections. At first they scanned the whole surface of the specimen in the two direction perpendicular to the layering one; then, they divided the surface in small square sectors and scanned them successively (changing the direction of  $90^\circ$  and the starting corner for every scan) or randomly (Fig. 1.7). They also varied the dimension of the square sectors and the working plane (direct base plate vs. powder layer). The obtained results indicate that the division in square sectors is preferable to the scanning on whole the surface, but the dimension of the squares seems to be not critical. The successive scanning method is better than the random one, probably because in the successive method the sectors are somehow pre-heated and then the thermal gradient is lowered.

## 1.8 Selective Laser Melting

Selective Laser Melting is a Rapid Manufacturing technique that directly follows Selective Laser Sintering (SLS). In the latter, the power of a laser beam is transmitted to a powder bed in order to sinter the powder itself. In Selective Laser Melting, on the contrary, the metal powder fully melts. This results in a fully dense material, coupled with better mechanical properties, but at the same time the process control becomes much more difficult.

In both the cases, however, the involved energies are quite low.

Table 1.1. Process parameters of Selective Laser Melting process.

Parameter	Dimensions
effective building volume	250x250x215 mm <sup>3</sup>
building speed	2-20 mm <sup>3</sup> /s
layer thickness	2-100 μm
laser type	Yb-fibre laser, 200 W
precision optics	F-theta-lens, high speed scanner
scan speed	up to 7 m/s
variable focus diameter	100-500 μm
power supply	32 A
power consumption	max. 5.5 kW
compressed air supply	7000 hPa; 20 m <sup>3</sup> /h
machine size	~2000x1050x1940 mm <sup>3</sup>
machine weight	1130 kg
certification	CE, NFPA

The Selective Laser Melting process is carried out on pre-alloyed powders. Consequently, no binders are present and then no additives are to be removed by heating.

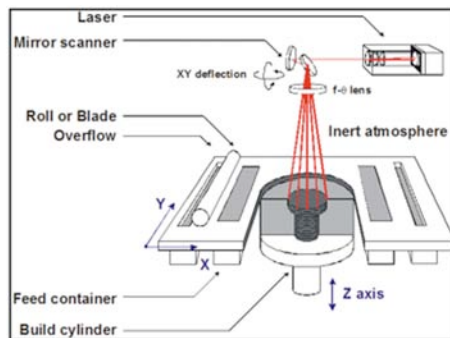


Figure 1.8. Mechanism of Selective Laser Melting [13].

The process is carried on in an inert gas atmosphere; no pre-heating is applied. So, the temperature of the working chamber remains in the neighborhood of the room temperature, and then the part undergoes a severe thermal gradient and a large undercooling during the cooling step. As a consequence, the solidification rate is high, carrying to a fine microstructure. But there is a second effect of the substantial thermal gradients which are inherently present in laser processes. In fact, laser technologies are historically bound to the arising of residual stresses in the parts. Large residual stresses can affect the resistance of the material (by delamination or cracking) and cause geometrical deformations in the part. As anticipated in paragraph 1.7, two mechanisms have been individuated to be responsible of residual stresses [14]: the so-called Temperature Gradient Mechanism and the mechanism related to the cool-down phase of the molten top layers.

## 1.9 Electron Beam Melting

During the Electron Beam Melting process, metal powders are selectively molten, layer by layer, through an electron beam. In comparison with Selective Laser Melting, the energy density is significantly higher.

Related to the involved energies, one of the most considerable difference between EBM and SLM consists in the pre-heating of the powder. In Electron Beam Melting, in fact, before melting the gun preheats the powder layer using a relatively low beam current and a relatively high scan speed. This results in two effects. The most important is the reduction of the thermal gradient between the just-melted layer and the already built up body of the part [5]; as a consequence, the substantial high temperature maintenance allows the reduction of residual stresses. Preheating also allows the partial sintering of the powder, which holds it in place during the subsequent melting.

Pre-heating has another eminent effect: it assists, in terms of energy, the remelting of the just-consolidated underlying substrate, allowing the incomplete homologous wetting due to oxide films to be avoided [8].

Moreover, Electron Beam Melting process takes place under high vacuum. This prevent a loss of energy that would be caused by the collision between the fast moving electrons and the gas molecules (making the process 95% energy efficient).

---

As an immediate result, vacuum prevents the absorption of atmospheric impurities. The focusing system is an electron optical one substantially similar to a scanning electron microscope; an electron gun, operating in vacuum, generates a focused beam. The electrons are emitted by a filament heated at a temperature above 2500 °C, and accelerated through an anode. A first system of coils (magnetic field lens) bring the beam into focus, while a second system of deflection coils steers the beam. The beam deflection occurs in absence of moving parts: the electron beam gun is stationary. This delivers very high scanning speeds.

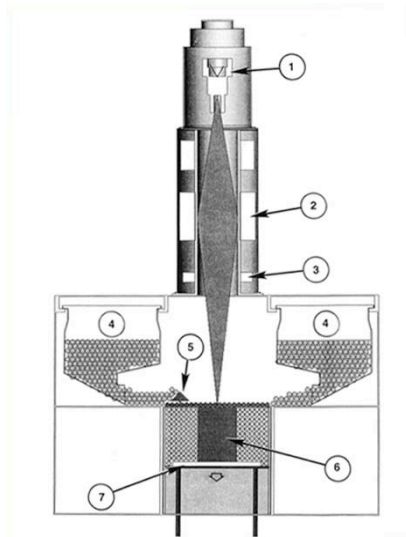


Figure 1.9. Mechanism of Electron Beam Melting [15]; (1) electron gun assembly, (2) EB focusing lens, (3) Eb deflection coils, (4) powder cassettes, (5) powder layer rake, (6) specimen, (7) working plate.

Electron Beam Melting works with quite high potentials, and then with quite high energy densities. The power of the beam is controlled by altering the current.

*Table 1.2. Process parameters of Electron Beam Melting process.*

<b>Parameter</b>	<b>Dimensions</b>
building tank volume	250x250x200 mm <sup>3</sup>
maximum build size	200x200x200 mm <sup>3</sup>
accuracy	±0.4 mm
melting speed	0.3-0.5 m/s
layer thickness	50-200 μm
electron beam scan speed	>1000 m/s
electron beam positioning accuracy	±0.05 mm
maximum electron beam output	4 kW
power supply	3x400 V, 32 A, 7 kW
machine size	~1800x900x2200 mm <sup>3</sup>
machine weight	1350 kg
certification	CE

Because of the dimension of the melting pool and the accuracy of the beam, the surface finishing of the part produced by EBM is less refined than the one obtained by SLM. A finishing is actually put into practice through a sand blasting after the process; this remove from the surface the partially sintered particles. The blasting is carried out using the same powder involved in the EBM process, in order to avoid contamination and recover the removed powder, which is sieved and recycled (up to 95%) in the process. Parts are built up on supports, for helping the removal of the parts themselves after the building. Because they are constituted by partially sintered powder, the supports are easy to remove (also by hand).

The powder employed in EBM, as well as that used in SLM, is pre-alloyed and does not contain additives or binders (as a consequence, no heat treatment is required for removing them; after building, the part has full density). The powder has a retained chemical composition due to the vacuum level in the chamber, the very small melted volume and the rapid cooling from melted metal to solid state.

Layer thickness in EBM technologies is usually larger than in SLM.

---

## References

- [1] Hollander D.A., von Walter M., Wirtz T., Sellei R., Schmidt-Rohlfing B., Paar O., Erli H., *Biomaterials* 27 (2006) 955
- [2] Ponader S., Vairaktaris E., Heini P., von Wilmsowky C., Rottmair A., Körner C., Singer R.F., Holst S., Schlegel K.A., Neukam F.W., Nkenke E., *J. Biomed. Mater. Res.* 84A(4) (2007) 1111
- [3] Bourell D., Wohlert M., Harlan N., Das S., Beaman J., *Adv. Eng. Mat.* 9(4) (2002) 663
- [4] Over C., Meiners W., Wissenbach K., Hutfless J., Lindemann M., "Rapid manufacturing of metal parts and tools using laser melting", working paper, Proceedings of the Second International WLT-Conference on Lasers in Manufacturing, Munich, Germany, June 2003
- [5] Cormier D., Harrysson O., West H., *Rapid Prototyping J.* 10(1) (2002) 35
- [6] Mitchell A., *Mat. Sci. Eng.* 263A (1999) 217
- [7] Simchi A., *Mat. Sci. Eng.* 428A (2006) 148
- [8] Vandenbroucke B., Kruth J.P., *Rapid Prototyping J.* 13(4) (2007) 196
- [9] S. Das, *Adv. Eng. Mat.* 10(5) (2003) 701
- [10] Kruth J.P., Froyen L., Van Vaerenbergh J., Mercelis P., Rombouts M., Lawers B., *Journal Mater. Process. Tech.* 149 (2004) 616
- [11] Tolochko N.K., Mozzharov S.E., Yadroitsev I.A., Laoui T., Froyen L., Titov V.I., Ignatiev M.B., *Rapid Prototyping J.* 10(2) (2004) 78
- [12] R. Glang, "Handbook of thin film technology", chapter 1, McGraw-Hill, 1970
- [13] J. Van Vaerenbergh, "Process optimization in Selective Laser Melting", University of Twente, The Netherlands
- [14] Mercelis P., Kruth J.P., *Rapid Prototyping J.* 12(5) (2006) 254
- [15] Murr L.E., Quinones S.A., Gaytan S.M., Lopez M.I., Rodela A., Martinez E.Y., Hernandez D.H., Martinez E., Medina F., Wicker R.B., *Journal Mech. Behavior Biomed. Mat.* 2 (2009) 20

## Chapter 2

# The materials

### 2.1 Metallic powder for Rapid Manufacturing

Rapid Manufacturing technologies are flexible in terms of employed materials. However, the soundness of the as-built material is strictly related to the control of process parameters, which is specific for every single powder. So, depending on the parameters and conditions discussed in the previous chapter (e.g., working atmosphere), different metallic powder can be more or less suitable to be used in a RM process.

During the process, the powder has to be melted and rapidly solidified. Starting from an atomized condition, it undergoes sudden changes in its state; the resulting microstructure is consequently process-related, intrinsic and peculiar.

The three alloys presented in the following are nowadays successfully produced by Rapid Manufacturing; anyhow, their microstructures are heavily different from the studied ones, usually referred to as-cast or wrought material. As a consequence, mechanical properties are distinctive of the material produced by RM.

In the following paragraphs, the three materials on which the present thesis work has been developed will be presented. These are Ti-6Al-4V alloy, ASTM F75 alloy and 17-4 PH Stainless Steel. Moreover, each of them will represent the starting point to discuss characteristics that are important for the biomedical applications, such as fatigue behaviour, wear resistance and hardening mechanisms.

---

## 2.2 Ti-6Al-4V alloy

Ti-6Al-4V (Ti grade 5) is the most widely used Titanium alloy. It is relatively expensive, because of intrinsic raw material, fabricating and metal removal costs. As a consequence, its employment in near-net shape technologies becomes consistent in order to reduce the costs.

The combination of chemical and biological inertness, high strength-to-weight ratio, excellent mechanical properties and corrosion resistance (by passivation) makes this titanium alloy the natural choice for many applications [1]. Consequently, Ti-6Al-4V has been employed in the production of parts for racing and aerospace industry, of turbines and, recently, of biomedical prostheses. Concerning the field of biomedical applications, Ti-6Al-4V alloy is involved in the production of hip prostheses (femoral stems), screws for dental implants and knee prostheses.

Ti grade 5 is a biphasic alloy. This means that both hcp ( $\alpha$ ) and bcc ( $\beta$ ) phases are present at room temperature. Unalloyed Ti is hcp at room temperature; some elements, such as Al, Ga, Sn and the interstitial elements O, N and C, act as stabilizer for this phase. Other alloy elements, such as V, Nb, Mo and W can enlarge the  $\beta$  field. As a consequence, in the Ti-6Al-4V alloy aluminum and vanadium operate as  $\alpha$ -stabilizer and  $\beta$ -stabilizer, respectively. In particular, Al raises the transus between  $\beta$  and  $\alpha+\beta$  field, while V lowers the transus between the biphasic and the  $\alpha$  fields. The composition of Ti-6Al-4V alloy fixes the transus from  $\alpha$  to biphasic field at 970 °C and the entry in the whole  $\beta$  field at about 1010 °C [2]. The presence of the two phases depends on thermodynamic factors as well as on kinetic factors. First of all, the bcc structure is more open than the hcp, and then its vibrational entropy is higher. As a consequence, the free energy of the bcc lattice decrease more rapidly on heating (and this explains why the bcc structure is the stable one at high temperature). But not only diffusive mechanisms are involved in the formation of different phases. Also martensite can form on rapid cooling from  $\beta$  or  $\alpha+\beta$  fields. It has an hcp structure, such as  $\alpha$  phase, but different lattice parameters, as discussed in the following.

The properties of the biphasic alloy are strictly related to its microstructure. A proper heat treatment can control these properties, adjusting the form in which the  $\beta$  phase is arranged.

### 2.2.1 Ti-6Al-4V alloy: microstructure

Traditionally, the different microstructures of the alloy are produced by thermomechanical treatments, which combines deformation and heating. During these treatments, recrystallization and aging take place.

There are three main parameters controlling the processes: the temperature, the cooling rate and the strain rate.

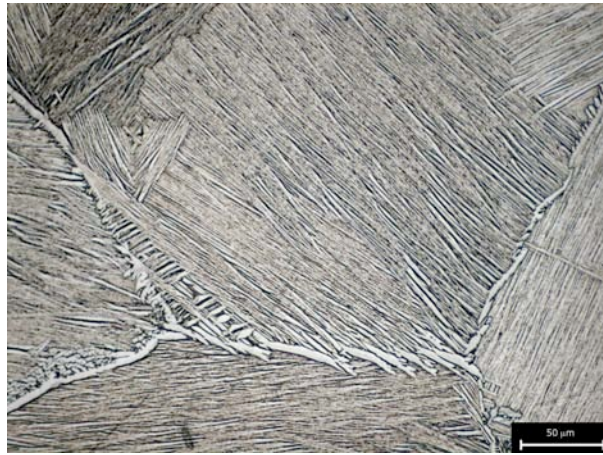


Figure 2.1. Example of lamellar microstructure, obtained by cooling from the  $\beta$  field.

Concerning the first one, a central point is the  $\beta$ -transus temperature,  $T_\beta$ , which separates the biphasic from the  $\beta$  field. In fact, cooling from above  $T_\beta$  results in a lamellar microstructure, in which  $\alpha$  phase nucleates at grain boundaries and then grows as lamellae into the prior  $\beta$  grains. Original  $\beta$  grain boundaries are still well recognizable after cooling (Fig. 2.1). The dimensions of the  $\alpha$  lamellae colonies are strictly related to the original dimension of the  $\beta$  grains: the colonies cannot grow larger than the prior grains. Lamellae colonies can form when cooling rates are relatively slow. The  $\alpha$  platelets orientation is related to the parent  $\beta$  phase orientation through the relation

$$\begin{aligned} \{110\}_\beta &\rightarrow (0001)_\alpha \\ \langle 111 \rangle_\beta &\rightarrow \langle 1120 \rangle_\alpha \end{aligned}$$

---

As a first result, the basal planes of  $\alpha$  phase are more distant in comparison with those of  $\beta$  phase: a weak lattice distortion is introduced. Then, the ratio between cell parameters  $c$  and  $a$  is lower than the ideal; on cooling, an increase in volume is observed. Moreover, the basal planes of  $\alpha$  phase derive from the more dense  $\beta$  planes. Since bcc systems have six slip planes and two direction of maximum density, the possible orientation for hcp growth are twelve. As a consequence, twelve are the orientations of  $\alpha$  lamellae in the prior  $\beta$  grains.

It is then reasonable to expect that, under slow cooling conditions, many adjacent  $\alpha$  lamellae take place from the transformation of  $\beta$  into the same, aligned Burger variant. If the alloy is cooled rapidly from the bcc field,  $\beta$  transforms to acicular  $\alpha$ . Hcp phase can nucleate directly from bcc in the form of needles, parallel to  $\{110\}$ , carrying to a basket-weave morphology. The prior  $\beta$  grain boundaries are still recognizable:  $\alpha$  phase takes up them and separates blocks of aligned needles.

When the treatment temperature falls in the  $\alpha+\beta$  field,  $\alpha$  phase is also present at equilibrium. The lower the temperature in the biphasic field, the smaller the volume fraction of  $\beta$  phase, but the higher its stability, thanks to the high concentration of vanadium.

In presence of a deformation, which furnishes a driving force for recrystallization [3-5], the microstructure of alloys treated in the biphasic field becomes equiaxed: globular primary  $\alpha$  grains are distributed in a lamellar matrix (Fig. 2.2). Depending on the cooling rate, lamellae can be constituted by martensitic hcp phase ( $\alpha'$ ) or by a biphasic  $\alpha+\beta$  mixture.

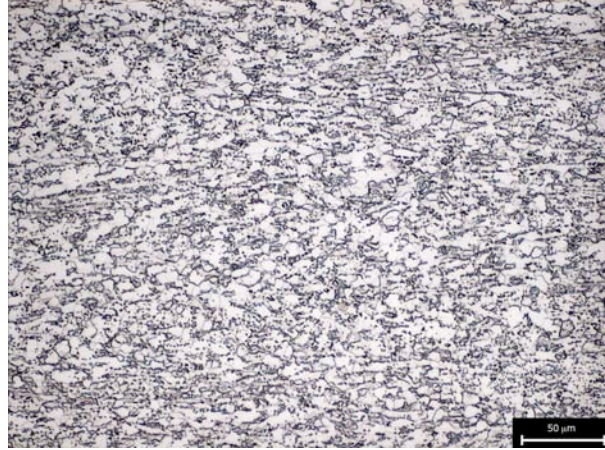


Figure 2.2. Example of  $\alpha$ -globular microstructure, obtained by cooling from  $\alpha+\beta$  field in presence of deformation; equiaxed  $\alpha$  grains are distributed in a biphasic matrix.

In an alloy like Ti-6Al-4V, in fact, a rapid quenching from above the  $\alpha/\alpha+\beta$  transus results (totally or partially) in the formation of a metastable martensitic structure. If the cooling rate is lower,  $\alpha$  phase can nucleate and grow into the prior  $\beta$  grains giving rise to a typical Widmanstätten morphology [2]. In alloys containing transition metals, such as vanadium, the martensitic transformation is of the second order: it is anticipated by a regime of structural fluctuation, in which  $\omega$  phase is present. This transition phase, very brittle, can also exist at room temperature as a consequence of very rapid quenching. In particular, a narrow compositional region in which  $\omega$  phase athermally appears during rapid cooling can be identified. The effective composition range where it can occur, however, is quite broad;  $\omega$  phase can, in fact, precipitate from  $\beta$  phase during isothermal aging at moderate temperature (around 400 °C) for long times, also for compositions outside the range.

Anyhow, it should also be considered that martensite has a free energy well lower than  $\omega$  and then, during its transformation, it tends to consume any  $\omega$ -phase precipitate in the matrix.

The presence of  $\omega$  phase, moreover, is substantially limited to  $\beta$  alloys in which the martensitic reaction is suppressed [6]. For these, the chemical composition (a strong presence of transition metals) assures electron/atom ratios in the range of formation of  $\omega$ .

---

The martensite start temperature for a titanium alloy also depends on the chemical composition of the alloy itself. It is around the  $\alpha+\beta/\alpha$  transus;  $\alpha$ -stabilizers lower  $M_s$ , while  $\beta$ -stabilizers can shift it into the  $\alpha+\beta$  field. The classical athermal diffusion-independent mechanism for martensite formation, involving the cooperative movement of atoms, is imaginable only for pure titanium. Alloy elements, in fact, have both a long-range effect (e.g., changes of the elastic parameters) and a local effect (the inhibition of atomic planes movement, resulting in the reduction of the cooperating atomic regions and in the lowering of transformation speed).

The basic morphology of the martensite in Ti and its alloys is a lath one, organized in packets: large zones (50-100  $\mu\text{m}$ ) containing fine parallel platelets 1  $\mu\text{m}$  wide. When the solute concentration increases, the platelets lose their parallelism: the resulting morphology is muddled and is defined as acicular. A further increase in the solute can make some  $\beta$  phase to be retained; the microstructure has then a Widmanstätten arrangement with acicular  $\alpha$  phase oriented along the  $\{110\}$  plane of the parent retained  $\beta$  phase. The Widmanstätten arrangement is a consequence of a nucleation and growth mechanism and is competitive with the athermal martensitic transformation when the diffusion coefficients are large enough.

Martensite can have two structures: hcp ( $\alpha'$ ) or orthorhombic ( $\alpha''$ ). Hcp is the general, common structure for titanium martensite. When the composition of the alloy reaches a certain level, varying from system to system, orthorhombic martensite can form.

As previously said, an amount of metastable  $\beta$  phase can be retained in alloys with high concentrations of solute elements. Under deformation, a stress-induced martensitic transformation, coupled with twinning, can occur. The martensite that forms by this way, because of the high solute concentration, is orthorhombic.

Finally, concerning the effect of the strain rate, its increasing corresponds to the change from an  $\alpha$ -globular microstructure to a lamellar (Widmanstätten) microstructure [7]. In fact, Semiatin et al. demonstrated [4] that two distinct temperature-strain rate regimes exist with regard to microstructural evolution during deformation in the biphasic field. For the lower regime, deformation is non-uniform (i.e., an intense localized shear makes the Widmanstätten colonies to break up and begin to spheroidize after a large amount of deformation). For the higher temperature regime, on the other hand, this non-uniform deformation does not take place. Since high strain rates make the transition between the regimes to shift towards the  $\alpha+\beta/\beta$  transus, they prevent the non-uniform localized deformation to occur, causing the

formation of a lamellar, rather than globular, microstructure.

### 2.2.2 Ti-6Al-4V alloy: mechanical properties

The microstructure of the alloy has a substantial influence on its properties. A primary rough distinction is related to the size and arrangement of  $\alpha$  and  $\beta$  phases.

As previously said, there are two farthest arrangements: the lamellar microstructure, which is generated by slow cooling down from the  $\beta$  field, and the equiaxed microstructure, which is the consequence of a recrystallization process. Both the extreme typologies can have a fine rather than coarse arrangement of the phases.

Larger dimensions of  $\alpha$  colonies in the lamellar microstructures have a beneficial effect on fracture toughness, creep resistance and fatigue crack propagation resistance, but a detrimental effect on tensile elongation [1]. On the other hand, an equiaxed  $\alpha$ -globular microstructure is associated with good tensile strength and good toughness. There is also an effect of the chemical composition on the mechanical properties. Interstitial chemical elements such as oxygen, nitrogen and carbon are  $\alpha$ -stabilizers. As a consequence, they favour the presence of  $\alpha$  phase, which is more resistant to plastic deformation but also less ductile. Both oxygen and nitrogen distort anisotropically the hcp lattice, limiting the dislocation mobility and then altering the slip behaviour of the alloy, resulting in an embrittlement in front of a hardness improvement. The alloying element Al also produces solution strengthening.

Morphology and arrangement of  $\alpha$  and  $\beta$  phases in the material also influence its fatigue endurance. For lamellar microstructures, cracks generally nucleate at slip bands in the lamellae or in the  $\alpha$  phase at the prior  $\beta$  grain boundaries. The reduction of the average dimension of the lamellae carries to an improvement of the resistance, both for low- and high-cycle fatigue. In equiaxed material, cracks generate along the slip planes of  $\alpha$  grains; fine grains are then preferable. In the case of duplex microstructures, where  $\alpha$ -globular grains lie in a biphasic acicular matrix, cracks can start from the lamellar matrix, the equiaxed grains or from the interfaces. Fine grain dimensions are one more time better for the resistance to crack initiation.

Concerning the propagation of the cracks, a distinction between long and short cracks must be done. In the following, after a brief reference to the classical study of fatigue, a discussion about the short cracks problem will be undertaken.

---

The theory of fatigue crack behaviour is related to the names of Paris and Erdogan [9]. Starting from the considerations accounted by the Linear Elastic Fracture Mechanics (LEFM), Paris and Erdogan suggested that, for a cyclic variation of the imposed stress field, the characterization of the rate of fatigue crack growth  $da/dN$  can be correlated with the range of the stress intensity factor  $\Delta K$  :

$$\frac{da}{dN} = C(\Delta K)^m$$

$$\Delta K = Y\Delta\sigma\sqrt{\pi a}$$

where  $a$  is the crack length,  $N$  is the number of load cycles,  $C$  and  $m$  are scaling constants, depending on material microstructure, environment, temperature and load ratio  $R$ , and  $\Delta\sigma$  is the stress range. The stress intensity factor for fatigue crack growth can lie well below the value of the quasi-static fracture toughness,  $K_{IC}$ .

There is a critical crack size,  $a_0$ , below which the value of the range of the stress intensity factor representing the fatigue threshold decreases with decreasing the crack length, since the critical stress range  $\Delta\sigma$  approaches the fatigue limit for negligible crack sizes. As a consequence,  $\Delta K$  becomes dependent on crack size, while it is independent for crack lengths above  $a_0$ . So, different advances have to be followed in approaching long cracks better than short cracks.

Short cracks, in particular, could represent a major problem in terms of failure probability.

In fact, starting from the same driving force for the growth of the cracks, short cracks can propagate much more rapidly than the long ones: as said, the characteristic parameter,  $\Delta K$ , is not the same for the two different length, and then dimensions and geometry become important. The critical crack size is the smallest length at which the Linear Elastic Fracture Mechanics is valid: under this value, the dimension of the plastic zone at the crack tip is comparable with the crack size.

Some retarding mechanism of the crack growth are active. Four main mechanisms can take place: (i) premature closure of crack faces (related to residual strain at the crack tail, surface roughness of the fracture surfaces, oxidation layers, stress- or strain-induced phase transformations); (ii) periodic deflection of crack path due to microstructural hitches or alteration in the local stress state; (iii) shielding of the crack tips, caused by the residual stress field generated within the cyclic plastic zone or by

stress-induced phase transformations; (iv) bridging between the crack faces.

Starting from these considerations, some consequences are to be inferred.

First of all, it is reasonable to understand that coarse grains are more effective on the deviation of crack path, since the crack walk becomes more roundabout. Moreover, microscopic local defects, such as grain boundaries, inclusions and precipitates can affect the path and the growth rate of small cracks, because their dimensions are comparable. (On the other hand, physically small cracks are less interested by extrinsic retardation mechanisms because of their dimensions, as reported in the following.)

In the study of the crack propagation mechanisms, nevertheless, approaches alternative to LEFM can be adopted. One of these takes into account interactions between microstructural barriers (e.g., grain boundaries) and slip bands at the crack tip [9]. On the basis of this theory, it is possible to understand that the threshold value of the stress intensity factor rises with the increase of grain dimensions for long cracks, and decreases for short cracks. So, grain refining allows a retardation of nucleation and growth for small cracks.

In order to introduce a reference parameter for the evaluation of the cracks length, a characteristic microstructural dimension is defined. In polycrystalline materials, this can be the grain size. Small cracks propagation is quicker than the long crack one when the dimensions of the plastic zone at the crack tip are smaller than this characteristic microstructural dimension. If the two dimensions result to be comparable, there is a behaviour convergence between short and long cracks.

Strictly concerning Ti-6Al-4V, the small cracks sub-critical growth rate seems to be substantially independent to the grains dimensions. The plastic zone at the crack tip is small relative to the crack size, and is also significantly smaller than the grain size. In general, as anticipated, the ratio between plastic zone size and the characteristic microstructural dimension is discriminating for the crack growth behaviour. One more time, we can say that small cracks grow faster than long ones when the ratio is small, while they converge on large cracks behaviour when the ratio approaches the unity.

Of particular relevance are the so-called physically short cracks. They are defined as cracks long less than 1-2 mm. So, they are significantly longer than the plastic zone at the crack tip, and also than the grain dimensions. Nevertheless, they propagate rapidly in comparison with long cracks. In fact, for large crack-tip plastic zones (greater than the LEFM prediction), a crack that is considered long in LEFM can actually be short

---

because of the high stress levels involved. High grow rates for physically short cracks are often attributed to the lack of extrinsic retardation mechanisms activated. Longer the crack, indeed, larger the zero-load crack-tip opening displacement, until a level (200  $\mu\text{m}$ ) beyond which closure becomes crack size independent.

Focusing on EBM and SLM technologies, defects driven by the process can be considered as physically short cracks. In particular, the incomplete homologous wetting phenomenon is responsible for the formation of cracks, with dimensions in hundreds of microns, between the layers. Consequently, considerations about short cracks become interesting.

### **2.2.3 Ti-6Al-4V alloy: application and corresponding required properties**

Ti grade 5 is a corrosion-resistant alloy. As previously stated, its employment in the biomedical field principally involves the production of femoral stems and acetabular cups for total hip replacement. For such applications, effectively, the employed material is required to have low specific weight but significant strength and fatigue endurance. Ti-6Al-4V represents a good compromise between the needed properties, since it is a light and resistant alloy, furthermore characterized by a stiffness lower than that of alloys typically employed (i.e., stainless steels or Co alloys). The low Elastic Modulus helps the stress to be more equally distributed between the prosthesis and the bony tissue, avoiding bone resorption and osteolysis.

### **2.3 ASTM F75 alloy**

CoCrMo ASTM F75 is a well known cobalt alloy.

In the past decades, it has been largely used both in aeronautical and biomedical field. Following the success of cobalt-base “hard-facing” tool materials during World War I, cobalt alloys were then used in weld overlay form to protect surfaces from wear, and then used on plowshares, oil well drilling bits, dredging cutters, hot trimming dies, and internal combustion engine valves and valve seats [1]. In particular, its high hardness,

combined with the hot corrosion and creep resistance, makes it an ideal material for turbine blades, vanes and buckets.

In the 30s and 40s, a corrosion-resistant cobalt-chromium-molybdenum alloy with a moderately low carbon content was developed to satisfy the need for a suitable investment cast dental material. This same alloy, named Stellite 21<sup>1</sup>, also underwent investment casting trials for World War II aircraft turbocharger blades, and, modified in following times to enhance structural stability, was successfully used in high-temperature applications.

ASTM F75 alloy corresponds, for chemical composition, with the “old” Stellite 21. The biomedical use of this alloy mainly concerns the production of femoral heads, knee prostheses and screws for dental implants. Its wear resistance plays a primary role in such applications [10-12], as discussed in the following.

ASTM F75 alloy also has a good corrosion resistance. The presence of chromium, in fact, allows the passivation of the surfaces, preserving the material from subsequent corrosion (also at high temperature).

### 2.3.1 ASTM F75 alloy: microstructure

Cobalt and its alloys have two allotropic phases: hexagonal close-packed (hcp,  $\epsilon$ ) and body-centered cubic (bcc,  $\alpha$ ). In pure cobalt, the former phase is stable below 400 °C, while the latter is stable for higher temperature. The free energy variation associated to the transformation is low. As a consequence, the transformation is slow [13].

The alloy composition affects the transition temperature. Typical alpha elements are Al, B, C, Mn, Fe and Ni; these elements enlarge the  $\alpha$  field. On the contrary, the  $\epsilon$  field is extended by elements such as Si, Cr, Mo and W. Only a few phase diagrams exhibit the presence of a biphasic field (as expected by the lever rule). The phase transformation occurs by a martensitic mechanism and is due to the dislocation movement on the octahedral plans of the cubic lattice. The plans sequence changes from *abcabc* to *ababab*. The Stacking Fault Energy (SFE) for both the phases is low: from  $31 \cdot 10^{-7}$  J/cm<sup>2</sup> (at 20 °C) to  $20.5 \cdot 10^{-7}$  J/cm<sup>2</sup> (at 370 °C) for  $\epsilon$  phase, and from

---

<sup>1</sup> the name “Stellite” comes from the Latin word *stella* (star), and is related to the brightness of the alloy.

---

$13.5 \cdot 10^{-7} \text{ J/cm}^2$  (at  $500 \text{ }^\circ\text{C}$ ) to  $18.5 \cdot 10^{-7} \text{ J/cm}^2$  (at  $710 \text{ }^\circ\text{C}$ ) for  $\alpha$  phase.

As an evidence of the long history of the Co alloys, there is the publication date of an important paper written by J.W. Weeton and R.A. Signorelli: 1954. The paper regards the effect of heat treatment upon microstructures, microconstituents and hardness of a wrought cobalt base alloy [14]. Hot working is, indeed, a typical processing route for Co alloys, as well as casting. Alloys for tribological and corrosion-resistant applications usually have a large amount (about 30%) of chromium. The cobalt-chromium system is then powerfully strengthened by the addition of molybdenum. A limited percentage of carbon allows the control of the amount of chromium carbides, resulting in the preservation of corrosion resistance. The result is the chemical composition of Stellite 21, which is the material studied by Weeton and Signorelli. They found out the wrought material to be extremely fine grained, equiaxed, with massive carbides and fine precipitates at the grain boundaries (Fig. 2.3).

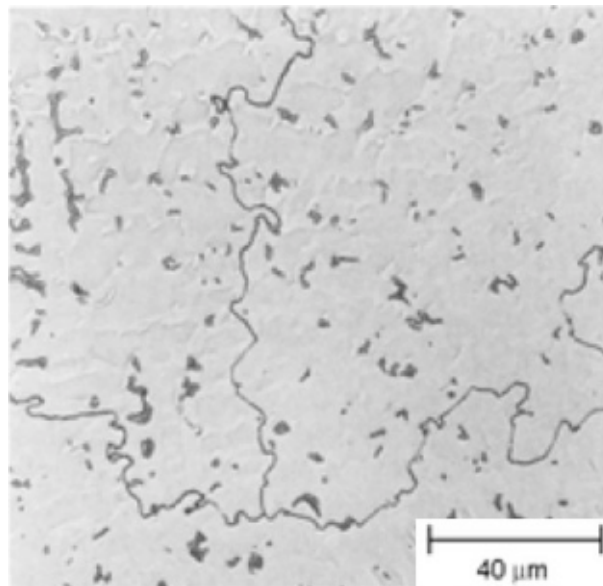


*Figure 2.3. Microstructure of a wrought Stellite 21; fine equiaxed grains with massive carbides and fine precipitates at the grain boundaries.*

The wrought material both contains  $\text{Cr}_{23}\text{C}_6$  carbide and  $\sigma$  phase. A solution treatment (followed by quenching) produced a solid solution showing little residual precipitation

( $M_6C$  and  $Cr_{23}C_6$ ); considerable grain growth occurred. The matrix wholly consisted of fcc phase. Aging at different temperatures resulted in precipitation, very rapid for the highest temperatures, along slip lines and twin boundaries generated by the rapid cooling. Hcp phase formed upon thermal treatment and quenching. Isothermal treatments directly following the solution treatment, carried out in order to study the isothermal transformations, resulted in the formation of a lamellar pearlitic-type structure along the grain boundaries; for long treatment times, the lamellae broke up and agglomerated into small spheroidized particles. For lowest temperatures, a Widmanstätten-type precipitate formed into the grains; a layer of precipitate-free matrix remained along most of the grain boundaries.  $M_6C$  and  $Cr_7C_3$  carbides appeared as well as  $Cr_{23}C_6$  and sigma phase. The  $\sigma$  phase is associated with a large amount of carbides, probably because the depletion of alloying elements due to the precipitation of carbides causes a lattice strain that can promote sigma precipitation near the carbides. While the low-temperature phase transformation from fcc to hcp is martensitic, the formation of the minor phases occurred by a nucleation and growth mechanism (involving diffusion), by direct precipitation from a single phase solution, eutectoid decomposition or transformation from a type of carbide to a second one. The pearlitic formation occurred with the diffusion of carbon from within the grains to the boundaries, where it formed carbide lamellae; as a consequence, a depletion on chromium in the solid-solution lamellae and in adjacent areas happened. The precipitation of  $Cr_{23}C_6$  carbides on the (111) octahedral plane of the austenitic fcc matrix was favored by the similarity between the atomic space of the plane and the adjoining plane of the carbide. This close structural relation makes it possible that initially the carbide forms from the austenite by a spontaneous non-diffusive transformation of the lattice.

### 2.3.2 ASTM F75 alloy: mechanical properties

The main properties of the Co alloys are related to the crystallographic nature of the cobalt, the solid solution strengthening (due to the effect of chromium and molybdenum, for instance) and the formation of metal carbides (responsible for precipitation hardening) [1].

Strictly concerning ASTM F75 (Stellite 21), it is substantially a carbide-hardened alloy.

---

The strength of the alloy, in fact, is in part provided by solution hardening, but mainly by the presence of carbides. These are usually distributed both at the grain boundaries and within the grains; the former obstruct gross sliding and migration of the boundaries, while the latter hinder the movement of dislocations. Their morphology and location influence the strengthening effect. Carbides are mainly formed from chromium, but also from molybdenum. Their observed forms are  $M_{23}C_6$ ,  $M_6C$ ,  $M_7C_3$ ,  $MC$  and, occasionally,  $M_2C_3$  [13]. The distribution of these carbides is initially determined by the temperature reached during processing and by the cooling rate. However, a solution treatment and aging combination can follow, in order to obtain a proper carbide distribution.

Co alloys are furthermore characterized by a low Stacking Fault Energy (SFE). As known, stacking faults are discontinuities in the stacking order of close-packed planes [15]; they can appear in fcc structures (on the octahedral plane), but also in hcp (on the basal plane, which has the same arrangement of atoms of the octahedral in fcc). These discontinuities are bounded by so-called partial dislocations: Shockley type, when the Burgers vector of the dislocation lies in the plane of the fault, or Frank type, when the Burgers vector is orthogonal to the plane. The formation of partial dislocations is associated to a lowering of the strain energy of the lattice, because the square of the Burgers vector (proportional to the energy of a dislocation) is larger, for the total dislocation, than the sum of those for the partials. The dimensions of a stacking fault depend on the balance between the repulsive force that partial dislocations exert each other and the surface energy associated to the plane discontinuity. Concerning the movement of the stacking faults, the main remark to be done regards cross-slip. In fact, since the direction of the Burger vectors of the partial dislocations does not lie in the cross-slip plane, two new dislocations have to be created during cross-slip. One of these is free to move in the cross-slip plane, while the second (called star-rod dislocation) is immobile and remains behind along the intersection between the planes (perpendicularly to them). The star-rod dislocation is removed when the second partial dislocation gets to the intersection between planes. Obviously, additional strain energy is required for the formation of the sessile star-rod dislocation; consequently, cross-slip on an extended dislocation is more difficult than for a total dislocation.

The low Stacking Fault Energy of cobalt-base alloys has some consequences. The main is that the deformation is arranged through the formation of stacking faults and

twinning and the localized slip along pre-existing stacking faults. The interaction between the slipping dislocations and the lattice defects (such stacking faults and twinings) is not easy: there is a difficulty of deformation to happen by dislocation slip. Strain hardening rate is, consequently, high [16].

It is then easy to understand that the low Staking Fault Energy is related to the material ability to deform uniformly until the fracture, without exhibiting plastic instability. In fact, plastic instability (connected to necking), as known, occurs when the condition is verified: the strain hardening rate cannot compensate for the rate of decrease of the tensile specimen cross-section area. An increasing of the strain hardening rate helps in avoiding the condition to be reached.

Moreover, in alloys where the austenitic phase is significantly present, uniform flow is furthermore enhanced. This is ascribable to the strain-induced phase transformation from cubic to hexagonal phase, happening during deformation. The formation of hcp martensite further increases strain hardening rates. This is the second reason why plastic flow keeps on uniform until fracture.

As stated above, Co alloys are well-known because of their wear resistance. Also concerning their use for the production of prosthesis parts, their wear behaviour results to be important, as discussed in the following of the section. Then, some general information about wear is now given, as an introduction to the subject.

Wear occurs when the contact between two bodies is responsible for the surface damage on one or both the bodies. Generally, wear debris are formed [17]. Adhesive wear is the wear mechanism involving two bodies in mutual sliding. Archard theory starts from the hypothesis of the plastic deformation of roughness in contact, and the following formation of plastic junctions. Some junctions can break the harshness, creating wear debris. The wear rate is proportional to the contact area, which in its turn is in inverse relation to the hardness of the material. A particular case of adhesive wear is trioxidative wear, which is a combination of oxidative process and mechanical action of the contact surfaces. Oxidation can be direct, because of the high sliding rate, or involve oxide scales formed by oxidized metal scraps (at low rates). Wear debris are here consisting of oxide particles.

Abrasive wear occurs between two bodies with a significant difference in hardness. Harder material can cause a plastic deformation in the softer one, removing some material (microcutting) or displacing it to the sides of the contact furrow (plowing).

Surface fatigue wear regards periodical solicitations, and is typical of non-conformal

---

contact: when a hertzian pressure springs underneath the surface, a fatigue crack can nucleate and propagate, carrying to the formation of a wear debris.

Sliding wear is determined by adhesive and tribooxidative mechanisms. Fretting is a particular case, in which the relative motion is oscillating and has small amplitude; it involves tribooxidative and surface fatigue mechanisms.

A lubricant is effective in the reduction of friction between two bodies in contact and in mutual sliding. The lubricant interposes between the surfaces reducing the shear stress necessary to the sliding itself.

### **2.3.3 ASTM F75 alloy: application and corresponding required properties**

CoCrMo alloys are characterized by hardness and by corrosion and creep resistance. Consequently, as anticipated in Paragraph 2.3.1, they have been largely used for the production of turbine components as well as for applications involving wear.

Biomedical prostheses made of Co alloy are usually subjected to tribological coupling. Wear debris are very critical for metallosis: debris can cause aseptic fibrosis, local necrosis or loosening of the device, acting as foreign agents responsible for immune response and infection [18,19]. So, a high wear resistance, preventing the release of metallic debris, can be helpful in the reduction of infection risks and prosthesis failure probability.

Anyhow, Co alloys are usually coupled with UHMWPE, both in hip and knee implants. The two bodies put into contact generally pay a marked difference in hardness. So, we have to consider that metal wear is negligible in comparison with the one affecting polyethylene: polymeric debris are released better than metallic. This debris may play an important role in the formation of osteolytic membranes at the interface between the implant and bone, carrying to a consequent bone resorption [16]. This introduces some considerations about the polishability of the alloy: if the metal part results to be well polished, in fact, its wear effect on the polymer is less crucial. As a consequence, the prosthesis will have a longer life. Co-Cr-Mo alloys are well polishable, and then are a good choice for the coupling with UHMWPE. Nevertheless, the presence of carbides causes, during polishing, the formation of a microstructural roughness, in which the distribution of carbides corresponds to a

distribution of asperities. Besides, carbides can separate from the matrix and become the third body in a three-body wear mechanism. As a consequence, a matrix free from carbides (typical of a low-carbon alloy, or a solution treated material) results to be better in the matching with polymer. Moreover, the hcp crystal structure gives lower friction coefficients in comparison with the fcc in the metal-to-metal contact. Therefore, the modification of the matrix phase composition by processing can induce a large improvement of the implant life.

Physiological environment, on its own, partially acts as a lubricant; however, it is also aggressive for the implanted materials, and can alter the tribological coupling. So, degradation of the implant can be the result of the combined action of wear and corrosion [20-22]. In the case of total hip replacement, for instance, aseptic loosening from UHMWPE debris is one of the most critical causes of failure for metal-on-polyethylene implants [23-25]. Loosening is due to sliding wear and fretting. Polymeric wear debris are responsible for the macrophage-induced degradation of bone surrounding the implant (periprosthetic osteolysis) [26]. The consequent loss of anchoring of the prosthesis is dangerous and painful.

In this background, ASTM F75 alloy enters as a strategical material. Evidently, as previously said, in the coupling with UHMWPE its wear loss is negligible. All the more reason, it becomes important that the metal friction effect on polymer be reduced. Concerning this, ASTM F75 alloy can be easily polished, and then it is ideal for the coupling.

## **2.4 17-4 PH Stainless Steel**

In order to obtain a proper combination of corrosion resistance, mechanical properties and workability, Precipitation Hardening (PH) stainless steels represent an excellent alternative choice to austenitic stainless steels. They are able to improve their mechanical strength by aging: very fine second-phase particles precipitate from a supersaturated solid solution. Thermal treatments are carried out as the final step of the process, because the dimensional variations conditioned by them are small.

PH stainless steels, depending on their chemical composition, can be martensitic, semi-austenitic or austenitic after the processing [27].

17-4 PH Stainless Steel (AISI 630) is a martensitic one: after solution treatment and

---

aging, its stable phase is martensite. Its strengthening agent for the precipitation hardening mechanism is copper.

Due to the combination of corrosion resistance and high hardness, the 17-4 PH Stainless Steel is usually employed in the production of surgical instruments (e.g., scalpels and pliers).

### **2.4.1 17-4 PH Stainless Steel: microstructure**

Generally, martensite start temperature ( $M_s$ ) for 17-4 PH Stainless Steel is in a reasonable neighborhood of 100 °C. Because of the chemical composition of the alloy, martensite is stable at room temperature; as a consequence, even if the rate is low, martensitic transformation can occur on cooling [28].

Usually, the steel is solution treated in austenitic field, cooled down to room temperature and afterwards aged. The microstructure of the steel is then basically composed by heavily faulted lath martensite in which copper has precipitated. The dislocation density of such material is high. Twins, resulting from the accommodation of the strain generated by adjacent laths, can be observed [29,30].

Chromium percentage in the composition of the alloy is within the spinodal line. Then, a long-time aging at low temperature (below 450 °C) results in the decomposition of the martensite into Fe-rich  $\alpha$  phase and Cr-rich  $\alpha'$  phase.



Figure 2.4. Microstructure of an AISI 630 grade containing  $\delta$ -ferrite; etched with Fry's reagent.

Depending on the cooling rate and on possible segregations,  $\delta$ -ferrite can be present as an additional stringer-shaped phase (Fig. 2.4). It usually forms on heating (e.g., sintering or debinding). The fraction of probable  $\delta$ -ferrite varies with Ni and Cr equivalents, according to the Schaeffler constitution diagram of stainless steel [31]. Since carbon is an important contributor to Ni equivalent,  $\delta$ -ferrite depends on it: the lower the carbon content, the higher the  $\delta$ -ferrite fraction.

The presence of  $\delta$ -ferrite is typical of Metal Injection Molding (MIM) technologies [32], because of the high temperature reached during processing.

### 2.4.2 17-4 PH Stainless Steel: mechanical properties

The 17-4 PH grade is usually employed for application after solution treatment and aging. Depending on the aging conditions, the tensile properties of the material can change (Tab. 2.1).

Table 2.1. Tensile properties of the alloy after aging treatment at different temperatures on the solution-annealed material [1].

	Yield stress [MPa]	UTS [MPa]	elongation [%]	hardness [HRC]
<b>H900</b>	1170	1310	10	40
<b>H1025</b>	1000	1070	12	35
<b>H1100</b>	795	965	14	31
<b>H1150</b>	725	930	16	28

This change in tensile properties is understood considering that the mechanical properties of the 17-4 PH Stainless Steel are mostly ascribable to the precipitation of copper-rich phases into the martensitic matrix. Hardness, in particular, is of great interest for the biomedical use, as stated above. The aging temperature, affecting the precipitation stage, has a strong effect on the resulting hardness.

Precipitation hardening is a well known and studied mechanism. A dislocation moving on its slip plane, when meets a particle, can cut through the particle, go beyond it by bending and creating a new dislocation ring (Orowan bowing) or go over by moving out from its slip plane [33]. In any case, an amount of energy must be expended.

The increase in yield stress due to the precipitation hardening principally depends on the strength, size and distribution of the precipitates. The degree of misfit or coherency between the particle and the matrix is also very important.

Precipitation hardening is induced by solution treatment followed by aging. During the solution treatment, the alloy is heated to a temperature at which the equilibrium concentration of solute into the matrix is high: a solid solution is formed. In particular, the solubility of copper in the iron austenitic matrix is approximately 9%. After the solution treatment, a very rapid quench from the solution temperature prevents an appreciable diffusion of the solute atoms, and then the material results to be a supersaturated solution [15]. This condition is very unstable.

The precipitation from supersaturated solution occurs by a nucleation and growth process; therefore, it is a diffusional process.

First of all, precipitation needs a finite time, called incubation period, before stable visible nuclei are formed. Then, precipitation goes on (*like the beat*) at different rates, depending on aging temperature: if the temperature is very low, diffusion is poor, while if it is near the solvus line, the solution is only slightly supersaturated and the

driving force for precipitation is small. So, the precipitation rate reaches a maximum at intermediate temperature.

Usually, in binary systems the precipitates pass through several stages before they get to a final structure. These stages have been diffusely studied for the binary Al-Cu system, and four different structures have been recognized for this alloy. They will be briefly described in the following lines. The first stage of aging consists in the clustering of solute atoms in areas called Guinier-Preston (GP) zones. The misfit caused by the solute atom in the matrix lattice is important for the shape of this zones: if the misfit is small, the GP zones shape is spherical (minimizing the surface, and then the surface energy); on the other hand, two-dimensional plates take place (minimizing the volume, and then the strain energy) when the misfit is larger. For Al-Cu system, the misfit is large. Prolonging the aging time, a second, intermediate structure forms. It is named  $\theta''$  and has the characteristics of a three-dimensional ordered phase, consisting of plates with several atomic layers thickness (larger than the GP zones). The following intermediate structure is the  $\theta'$ , which is very similar to the stable phase  $\text{CuAl}_2$ , but is partially coherent with the lattice of the aluminum matrix. This is the more effective precipitate regarding the improvement in hardness, at least till the  $\theta'$  particles are small and distributed. The  $\text{CuAl}_2$  ( $\theta$ ) precipitate, which is the fourth and last structure, is incoherent; when it forms, the hardness definitively decreases.

These remarks about the precipitation hardening mechanism can be applied to a binary system as the Fe-Cu, which is of interest for the AISI 630 alloy. In 17-4 PH Stainless Steel, in fact, the hardening element is copper, whose percentage is about 4%. As a consequence, the mechanical properties of 17-4 PH stainless steel are strictly related to the aging treatment the material undergoes.

As previously said, quenching rates after the solution treatment are usually very rapid. However, for an alloy such as AISI 630, in which martensite is chemically stabilized at room temperature, cooling rates can also be relatively slower.

Metals Handbook suggests [34] a sequence of heat treatments for this alloy. The preliminary step consists in a homogenization at  $1175 \pm 15$  °C for times from 2 h; this is followed by a solution treatment (austenite conditioning) step at  $1040 \pm 15$  °C for times from 30 min. To prevent cracks and ensure uniform properties, parts are mainly cooled in air. Oil quench is an alternative for small parts.

Hardening by aging is carried out in a temperature range spreading from 480 °C (900

---

°F) to 620 °C (1150 °F), for times of 1-4 h. Aging treatment reference abbreviations refer to the Fahrenheit temperature preceded by the cap letter H. The aging treatments suggested by the Metals Handbook are then H900, H925, H1030, H1050, H1075, H1150. Depending on the different temperature, mechanical properties of the steel change. However, the material has the ability to develop very high strength without fall in a dramatic loss of ductility. Already in the solution-treated condition the material has appreciable mechanical properties; nevertheless, the alloy is usually employed in the aged condition.

Mirzadeh and Najafizadeh [35] take into account a “tempering parameter” (Larson-Miller) that simultaneously involves tempering temperature and time. This parameter is

$$P = T(C + \log t) * 10^{-3}$$

where  $T$  is the absolute temperature,  $t$  is the time (in hour) and  $C$  is a material constant (corresponding to values from 10 to 20; usually considered as 20).

Contemporarily, they report hardness as a dimensionless parameter named as “relative percentage of hardening”, represented by

$$H_t = \frac{H - H_{st}}{H_{st}} * 100$$

where  $H$  is the hardness of the aged material, while  $H_{st}$  is the hardness of the alloy in the solution treated condition. The study of data reported in literature allows the deduction of some considerations from the relative percentage of hardening vs. tempering parameter graphs. There are mainly four stages. (i) At low tempering parameters (stage I), time and/or temperature are insufficient for precipitation of copper phases; then, no increase is registered in the relative percentage of hardening. (ii) During stage II, when the tempering parameter assumes values ranging from 10 to 15, hardness increases. However, from 13.25 on the hardening rate slows down, probably because of the softening related to the recovery of martensite. (iii) When the tempering parameter falls between 15 and 18 (stage III), the relative percentage of hardening decreases. This is attributed to the accompanying effect of recovery of martensite, coarsening of precipitates and probably reversion of martensite to

austenite. (iv) Above 18, in the stage IV, the tempering parameter is related to a negative relative percentage of hardening, mainly because the three concomitant phenomena of stage III are exhausted.

The maximum hardness is obtained for tempering parameters around 15; this corresponds to an H900 aging treatment. For parameters from 15 to 19, in the neighborhood of H1025, the material is in an overaging condition, where toughness is higher. Above 19, the tempering parameter matches H1150 aging condition, producing a material that is softer than the solution-treated one and is suitable for cold working.

Generally, temperature has a large influence on aging behaviour: hardness increase is more pronounced at higher temperatures, and at the same time the rate of decrease after the hardness peak is quicker. The effect of aging time is negligible in the nearby of 450 °C, but becomes more significant below and above this temperature.

Concerning the reformation of austenite on aging in stage III, Hsiao et al. [36] made some interesting observation by dilatometric and TEM analyses. They determined the  $A_{C1}$  and  $A_{C3}$  temperature, at 725 °C and 915 °C, respectively, and also the  $M_s$  temperature, around 105 °C. The latter is in contrast with the calculated one, which is 229 °C taking into account carbon, manganese, nickel, chromium and molybdenum, but neglecting copper. The microstructure of the solution treated specimen is composed of lath martensite with a high dislocation density [36,37] and micro-twins; the martensitic matrix is supersaturated with copper, and no precipitation is observed. The relation between micro-twins and laths has been attributed to the cooperative “back-to-back” growth mechanism of adjacent laths, which have opposite shape deformations. The inter-twin space is observed to be generally large and twins are oriented as the adjacent martensite laths. During the aging process, tempering of martensite and precipitation of copper-rich phases occur. However, Hsiao et al. observed that tempering has a little effect on hardness, because of the small carbon amount in the martensite. Moreover, after aging at 480 °C for 1 h (when a peak in the age-hardening is reached), the lath martensite matrix still exhibits a very high dislocation density; some “strain strings” appear, due to the copper precipitates along the dislocations. These precipitates, however, are coherent with the matrix and do not cause large strain; they have an fcc lattice and elliptical shape, the axes of which are 15 nm and 25 nm long. After aging at 620 °C for 4-8 h, Hsiao et al. observed a large amount of precipitates with an average size of 30 nm. These are a copper-rich phase

---

with fcc lattice. The formation of reversed austenite is also noticed; it proceeds along the original martensite laths, following a Nishiyama-Wasserman orientation relationship for the habit plane [37], and its morphology suggests that its formation mechanism is diffusional. Reversed austenite forms along the laths because of the segregation of copper (which is a  $\gamma$ -stabilizer) towards the lath boundaries (where copper-rich phases precipitate) and the consequent depletion of Cu into the laths themselves. This austenite is retained on cooling; copper and nickel must have segregated to these areas and lowered the  $M_s$  temperature below the room temperature. Another interesting observation regards the treatment temperature, which is well below the  $A_{C1}$  temperature. The understanding of this annotation is related to the precipitation of copper phases before the austenite formation. In fact, copper particles have the same structure (fcc) of the austenite, and similar lattice parameter; as a consequence, they are preferential heterogeneous nucleation site for austenite. Moreover, since the solubility of Cu and Ni in the austenite is high, during aging the austenite can be enriched of these elements by diffusion.

Aging is also associated to a recovery of the dislocations, which results in a decrease of the dislocations density and in the formation of regular arrays of dislocations.

Concerning the copper precipitation, in the Fe-Cu binary system it starts with the formation of spherical copper-rich bcc areas. These areas are nearly spherical because of the tendency to minimize the surface energy. Because of the trifling difference between the atomic radii of copper and iron, this surface energy is mainly due to the chemical component (the strain component is negligible). After reaching a critical size, the copper-rich particles transform (probably by a shear process) into an fcc structure, which cannot maintain the coherency with the bcc lattice of the Fe matrix.

Nakagawa and Miyazaki [38] investigated a martensitic PH stainless steel with a chemical composition similar to the one of 17-4 PH. Carbon and nitrogen contents were controlled in order to reduce carbides and nitrides, and Cr-equivalent and Ni-equivalent were balanced with the aim of reduce the presence of  $\delta$ -ferrite and adjust the  $M_s$  temperature. In particular, nickel was added as a  $\gamma$ -stabilizer (instead of C) in order to reduce or eliminate the ferrite content and lower the  $M_s$  temperature. Authors applied a solution treatment to the material, and then quenched it to various temperatures, in order to obtain different amounts of austenite in the material. They observed a highly dislocated lath martensite, with interlath films of retained austenite. The formation of the  $\gamma$  phase follows, furthermore, a Nishiyama-Wasserman

orientation relationship. Some twins formed on  $\{112\}_{\text{bcc}}$  plate, but their density is low. Nakagawa and Miyazaki observed that there were two mechanisms of stabilization of the austenite. The first was attributed to the compression stress caused by the formation of a large amount of martensite on cooling, and gave rise to 10% of  $\gamma$ . The second mechanism was related to the formation of atmospheres with interstitial atoms around lattice defects and to the precipitation hardening of martensite. No Ni enrichment in the austenite took place, and then no chemical stabilization occurred. The effect of austenite on the mechanical properties can be linearly represented. Yield stress and tensile strength decrease, whilst elongation rises with the increase of the amount of retained austenite. However, metastable austenite can transform into martensite during deformation, as discussed in the following.

### **2.4.3 17-4 PH Stainless Steel: application and corresponding required properties**

Precipitation Hardening stainless steels are able to combine high hardness with corrosion resistance. Moreover, they are easily machined. They traditionally offer an alternative choice to austenitic stainless steels in aeronautical and aerospace applications, as well as in naval field (e.g., for the production of hardly loaded axles and hydrofoil legs).

Concerning medical applications, the 17-4 PH Stainless Steel is usually employed in the production of surgical instruments, such as scalpels, because of its high hardness (due to precipitation of copper compounds in the martensitic matrix) and its workability. Since the steel has not to be implanted in the human body, biocompatibility is not a required property. Nevertheless, its corrosion resistance is important.

---

## References

- [1] *ASM Metals Handbook*, 9th ed., American Society for Metals, Metals Park, Ohio 44073, Vol. 2, 1985
- [2] E.W. Collings, "The physical metallurgy of titanium alloys", American Society for Metals, 1984
- [3] N. Stefansson, S.L. Semiatin, D. Eylon, *Metal. Mater. Trans.* 33A (2002) 3527
- [4] S.L. Semiatin, J.F. Thomas Jr., P. Dadras, *Metall. Trans.* 14A (1983) 2363
- [5] E.B. Shell, S.L. Semiatin, *Metal. Mater. Trans.* 30A (1999) 3219
- [6] G. Lütjering, J.C. Williams, "Titanium", Springer, 2003
- [7] S.L. Semiatin, V. Seetharaman, I. Weiss, *JOM* June (1997) 33
- [8] C. Leyens, M. Peters, "Titanium and titanium alloys", Wiley-VHC, 2003
- [9] M. Benedetti, "Initiation and propagation behaviour of fatigue cracks in titanium alloys", Ph.D. thesis, Department of Materials Engineering and Industrial Technologies, University of Trento
- [10] D.C., Mears *Int. Metal Rev.* 119 (1977) 1
- [11] L.Z. Zhuang, E. W. Langer, *J. Mater. Sci.* 24 (1989) 4324
- [12] H.F. López, A.J. Saldivar-Garcia, *Metal. Mater. Trans.* 39A (2008) 9
- [13] W. Betteridge, "Cobalt and its alloys", E. Horwood Series, 1982
- [14] J.W. Weeton and R.A. Signorelli, *Trans. ASM* 47 (1954) 815
- [15] R.E. Reed-Hill, R. Abbaschian, "Physical metallurgy principles", PWS Publishing Company, 1994
- [16] A. Salinas-Rodriguez, J.L. Rodriguez-Galicia, *J. Biomed. Mater. Res.* 31 (1996) 409
- [17] G. Straffelini, "Attrito e usura - metodologie di progettazione e controllo", Tecniche Nuove, 2008
- [18] J. Black, H. Sherk, J. Bonini, W.R. Rostoker, W. Schajowicz, J.O. Galante, *J. Bone Joint Surg. Am.* 72 (1990) 126
- [19] G. Meng Tan, G. Lynne, S. Sarbjit, *J. Arthroplasty* 23(5) (2008) 775
- [20] M. Azzi, M. Paquette, J.A. Szpunar, J.E. Klemberg-Sapieha, L. Martinu, *Wear* 267 (2009) 860
- [21] S. Mischler, A. Spiegel, M. Stemp, D. Landolt, *Wear* 251 (2001) 1295
- [22] P. Jemmely, S. Mischler, D. Landolt, *Tribol. Int.* 32 (1999) 295
- [23] G. Matsoukas, R. Willing, I. Yong Kim, *J. Biomech. Eng. T-ASME* 131 (2009) 1
- [24] M. Jasty, D.D. Goetz, C.R. Bragdon, K.R. Lee, A.E. Hanson, J.R. Elder, W.H.

- Harris, J. *Bone Joint. Surg. Am.* 79 (1997) 349
- [25] W.H. Harris, *Clin. Orthop. Relat. Res.* 467 (2009) 28
- [26] B. Sonny Bal, D. Vandelune, D.M. Gurba, M. Jasty, W.H. Harris, *J. Arthroplasty* 13(5) (1998) 492
- [27] L. Di Caprio, “Gli acciai inossidabili”, Hoepli, 2003
- [28] W.F. Smith, *Structure and Properties of Engineering Alloys*, second ed., McGraw-Hill, 1992
- [29] S.A.A. Akbari Mousavi, A.R. Sufizadeh, *Mater. Design* 30 (2009) 3150
- [30] J. Wing, H. Zou, C. Li, R. Zuo, S. Qiu, B. Shen, *Journal of University of Science and Technology Beijing* 13(3) (2006) 235
- [31] J.R. Davis, in “Stainless steel”, ASM International, Materials Park, Ohio, 1994
- [32] R.M. German, D. Kubish, *Int. J. Powder Metall.* 29 (1993) 47
- [33] R.W.Cahn, P. Haasen, “Physical metallurgy”, Elsevier, 1996
- [34] *ASM Metals Handbook*, 9th ed., American Society for Metals, Metals Park, Ohio 44073, Vol. 4, 1985
- [35] H. Mirzadeh, A. Najafizadeh, *Mater. Chem. Phys.* 116 (2009) 119
- [36] C.N. Hsiao, C.S. Chiou, J.R. Yang, *Mater. Chem. Phys.* 74 (2002) 134
- [37] U.K. Viswanathan, Banerjee S., Krishnan R., *Mater. Sci. Eng.* 104A (1988) 181
- [38] H. Nakagawa, T. Miyazaki, *J. Mater. Sci.* 34 (1999) 3901

## Chapter 3

# Requirements for the application

### 3.1 The biomedical standards

The application of metallic alloys in the biomedical field is regulated by international standards that fix or suggest some specific requirements concerning the microstructure and the mechanical properties of the employed alloy. The biomedical field, in fact, needs particular attentions, since it involves human health. Consequently, from material to material, many different features become critical. Strictly regarding the materials discussed in this thesis work, they are subjected to different requirements. First of all, the chemical composition. Moreover, Ti-6Al-4V and ASTM F75 alloys, which are directly applied to the human body, undergo precise qualifications about tensile properties. On the other hand, 17-4 PH Stainless Steel needs to be hard, since it is not implanted but only used for surgical instruments. Ti-6Al-4V is also limited in the use by some microstructural characteristics. Even if an acceptable level of biological response can be expected from surgical implant metals, they have never been shown to cause absolutely adverse reactions in the human body. Consequently, standards usually refer to indications based on a long-term clinical experience. Moreover, the standards here taken into account refer to materials produced by hot working or casting, since these are the traditionally employed materials. Since no standard exists making reference to EBM or SLM products for biomedical applications, the standards referring to classically produced alloys have to be considered.

In the light of what just written, the principal standard requirements for the three materials are dealt with in the following. Some critical issues related to single materials

and single technologies will be anticipated in this chapter. These issues will be approached from an industrial point of view, highlighting those specific aspects the producers are interested in.

### 3.2 Requirements on chemical composition

The three alloys taken into account by this thesis are required to comply with specific chemical composition, since they have to resist to corrosion in physiological environment in order to avoid metallosis and other related problems, as previously stated. The ISO 5832-3 for Ti grade 5 alloy, the ISO 5832-4 for ASTM F75 alloy and the ASTM A564M-04 for 17-4 PH Stainless Steel are the standard usually taken as a reference for the chemical composition. The fact that one standard is chosen rather than another principally depends on the customers' wishes. The ASTM 1472-02a standard, for instance, can indifferently be required instead of ISO 5832-3 for the Ti alloy. The requirements of the two standards, for chemical composition as well as for tensile properties, correspond. In the next paragraphs, then, only one standard will be considered and discussed for each material. Concerning the chemical compositions, standard requirements are summarized in Table 3.1.

*Table 3.1. Chemical requirements from the reference standards.*

ISO 5832-3 (Ti-6Al-4V)		ISO 5832-4 (ASTM F75)		ASTM A564M (17-4 PH)	
element	[%]	element	[%]	element	[%]
Al	5.50-6.75	Cr	26.5-30.0	Cr	15.0-17.5
V	3.5-4.5	Mo	4.5-7.0	Ni	3.0-5.0
Fe	0.3 max	Ni	1.0 max	Cu	3.0-5.0
O	0.2 max	Fe	1.0 max	C	0.07 max
C	0.08 max	C	0.35 max	Mn	1.0 max
N	0.05 max	Mn	1.0 max	P	0.040 max
H	0.015 max	Si	1.0 max	S	0.030 max
Ti	balance	Co	balance	Si	1.0 max
				Fe	balance

---

In addition, the amount of Nb and Ta (summed) in AISI 630 stainless steel should fall in a range between 0.15% and 0.45%.

The chemical composition of the processed materials matches the standard indications for both Electron Beam Melting and Selective Laser Melting. Then, they will be not commented in the following.

### 3.3 Requirements on mechanical properties

As stated above, both Ti grade 5 and CoCrMo alloys need to match tensile requirements in order to be applicable as prostheses materials. In particular, the ISO 5832-3 standards is to be followed for Ti-6Al-4V, while ISO 5832-4 is the reference standard for the F75 alloy.

#### 3.3.1 ISO 5832-3 standard for Ti-6Al-4V alloy

The ISO 5832-3 standard makes reference to wrought Ti-6Al-4V alloy used in the manufacture of implants for surgery. The indications about tensile properties are related to testing carried out under the prescriptions of the ISO 6892 standard. For a bar material, these indications are those summarized in Table 3.2.

*Table 3.2. ISO 5832-3 standard prescriptions for wrought Ti-6Al-4V alloy used in manufacture of implants for surgery.*

Tensile property	Prescription
Proof stress on non-proportional elongation	> 780 MPa
Tensile Strength	> 860 MPa
Percentage elongation after fracture	> 10 %

For the evaluation of the percentage elongation after fracture, the ISO 6892 standard takes into account a gauge length equal to  $5.65\sqrt{S_0}$ , where  $S_0$  is the original cross-sectional area.

Concerning this thesis work, the noticed problem regarded the material produced by Selective Laser Melting. As discussed in the following, in fact, the ductility of the as-built material did not satisfy the standard prescriptions, requiring an improving in the elongation at fracture.

### 3.3.2 ISO 5832-4 standard for ASTM F75 alloy

The tensile properties of an as-cast CoCrMo alloy used for the production of surgical implants undergo the suggestions of the ISO 5832-4 standard. Even if the material produced by Electron Beam Melting is deeply different from the as-cast alloy, ASTM F75 alloy used for the production of biomedical parts is usually produced by casting. Then, in absence of a specific standard for EBM products, the reference standard is reasonably that for casting alloy. The specifications coming from this standard are reported in Table 3.3.

Table 3.3. *ISO 5832-4 standard prescriptions for as-cast CoCrMo alloy used in manufacture of implants for surgery.*

<b>Tensile property</b>	<b>Prescription</b>
Proof stress on non-proportional elongation	> 450 MPa
Tensile Strength	> 665 MPa
Percentage elongation after fracture	> 8 %

The gauge length taken into account in the evaluation of the elongation at fracture is the same of Paragraph 3.3.1. Reference testing must be carried out under the prescriptions of the ISO 6892 standard.

Also in this case, the problem regards the ductility of the as-built alloy. The material produced by Electron Beam Melting, in fact, is hard and brittle, as will be shown in Chapter 6. Then, something has to be done in order to improve ductility and match the standard requirements.

---

### 3.3.3 ASTM A564-02 standard for 17-4 PH Stainless Steel

The standard directions concerning hardness of hot-rolled and cold-finished age-hardening stainless steel bars are included in the ASTM A564M-04 standard. Following this, the hardness of the solution annealed (at 1040 °C) AISI 630 stainless steel shall conform to 38 HRC. After an H900 aging treatment, hardness shall be higher than 40 HRC. Tensile properties are considered by the producers to be less important than hardness. The Rockwell hardness of the as-built (and stress relieved) 17-4 PH Stainless Steel results to be 27 HRC; moreover, after solution treatment at 1040 °C for 1 h and aging at 480 °C for 1 h, the material still present an unsatisfactory hardness. As a consequence, the knowledge of the 17-4 PH grade produced by SLM had been deepened in order to achieve the desired hardness.

## 3.4 Microstructure

The ISO 5832-3 standard, as well as about tensile properties, provides indications at regard of how the microstructures shall appear. ISO 5832-3 makes reference to the second publication (1979) of the European Titanium Producers' Technical Committee (ETTC). On its turn, the ISO 20160 standard is the specific standard concerning the classification of microstructures for  $\alpha+\beta$  titanium alloy bars, acknowledging the ETTC 2 directions. In plain words, the ISO 20160 standard provides, receiving the ETTC 2 indications, a list of metallographic micrographs for the designation of microstructures of biphasic titanium alloys in the form of bars. This standard works as an aid in the communication. The list is then referred to by the ISO 5832-3 standard: this ratifies which reference micrographs the microstructure shall correspond to. In particular, the ISO 5832-3 standard indicates micrographs from A1 to A9 of the ISO 20160 standard as suggested microstructures. Moreover, microstructures corresponding to the micrographs A20 to A24 of the ISO 20160 standard are classified as unacceptable in the first edition of ETTC 2.

From a practical point of view, the micrographs reported in the ISO 20160 standard represent transverse sections of bar material, after suitable etching (i.e., with Kroll's reagent). This is a useful specification, since bar products can be affected by a microstructural anisotropy due to the processing. In the following, some of the

micrographs reported in the ISO 20160 standard are reproduced, in order to supply a reference for Chapter 5 of the present thesis.

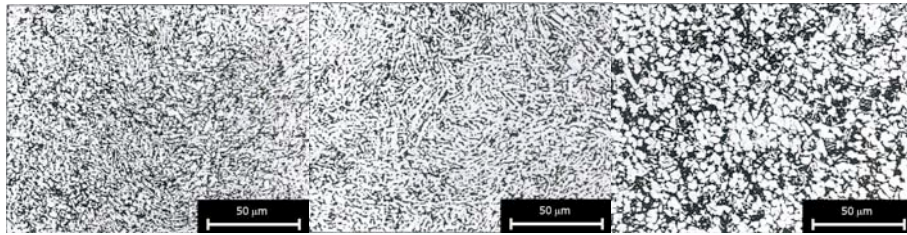


*Figure 3.1. Micrograph A2, A4, A5 reported in the ISO 20160 standard; suggested microstructures.*

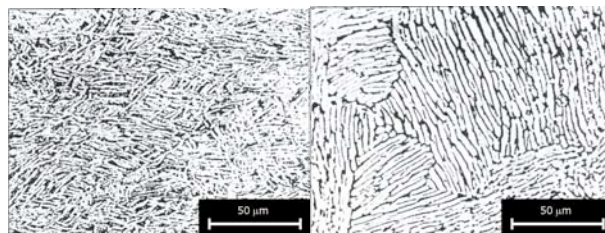


*Figure 3.2. Micrographs A15 and A16 reported in the ISO 20160 standard; not suggested by the standard but not rejected by ETTC 2.*

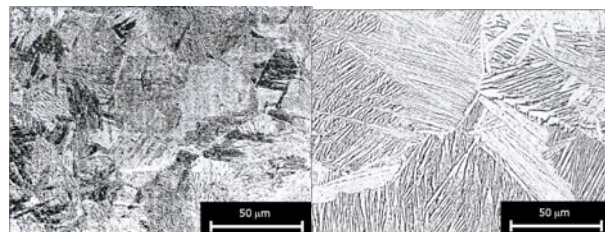


*Figure 3.3. Micrographs A23 and A24 reported in the ISO 20160 standard; classified as unacceptable by ETTC 2.*

Figure 3.1 makes reference to three of the micrographs indicated by the ISO 5832-3 standard as suggested. They are mainly globular. Figure 3.2, on the other hand, shows two coarse lamellar microstructures that are not suggested by the standard, but also not rejected by ETTC 2. Finally, Figure 3.3 reports two basket weave and lamellar microstructures that are explicitly classified as unacceptable by ETTC 2. It can be

---

anticipated that Ti-6Al-4V grades produced by both Electron Beam Melting and Selective Laser Melting are characterized by fine microstructures that can strongly differ from those shown here, or correspond to unacceptable micrographs. In particular, the former is similar to the micrograph on the left of Figure 3.3, while the latter is martensitic. As a consequence, the thermal stability of the two as-built microstructure had to be investigated in order to understand if a correspondence with the standard requirements would be possible.

### **3.5 Density of the alloys produced by Rapid Manufacturing techniques**

When the control and the combination of the process parameters is consolidated, Rapid Manufacturing techniques involving the melting of the processed powders result in fully dense materials, as stated in Chapter 1. In the present thesis work, if not differently specified, the material referred to is always to be considered fully dense.

## Chapter 4

# Materials and experimental procedures

### 4.1 Powders

The powders employed in Rapid Manufacturing processes are usually gas-atomized powders, with spherical morphology.

The chemical compositions collected on the powders used for the present thesis work, provided by the machine producers, are summarized in Tables 4.1-4.4.

*Table 4.1. Measured chemical composition of the Ti-6Al-4V alloy employed in the Electron Beam Melting process.*

Ti-6Al-4V EBM								
element	Al	V	Fe	O	N	H	C	Ti
[%]	6.010	3.900	0.071	0.130	0.002	0.010	0.011	bal.

*Table 4.2. Measured chemical composition of the Ti-6Al-4V alloy employed in the Selective Laser Melting process.*

Ti-6Al-4V SLM								
element	Al	V	Fe	O	N	H	C	Ti
[%]	5.970	4.010	0.056	0.160	0.003	0.010	0.013	bal.

Table 4.3. Measured chemical composition of the ASTM F75 CoCrMo alloy employed in the Electron Beam Melting process.

<b>ASTM F75 EBM</b>							
<b>element</b>	Cr	Mo	C	Fe	Ni	Mn	Si
<b>[%]</b>	28.5	6.0	0.3	0.2	0.25	0.5	0.7
<b>element</b>	N	W	P	S	Al	Ti	Co
<b>[%]</b>	0.15	0.01	0.01	0.005	0.05	0.01	bal.

Table 4.4. Measured chemical composition of the 17-4 PH Stainless Steel employed in the Selective Laser Melting process.

<b>17-4 PH SLM</b>					
<b>element</b>	Cr	Ni	Cu	Si	Mo
<b>[%]</b>	15.33	4.76	3.99	0.62	0.52
<b>element</b>	Nb	Mn	C	P	Fe
<b>[%]</b>	0.216	0.113	0.043	0.022	bal.

The particle sizes of the different powders are reported in Table 4.5.

Table 4.5. particle sizes of the metallic powders used in the EBM and SLM processes.

<b>particle size [<math>\mu\text{m}</math>]</b>	
<b>Ti-6Al-4V EBM</b>	45-100
<b>Ti-6Al-4V SLM</b>	< 50
<b>ASTM F75 EBM</b>	30-100
<b>17-4 PH SLM</b>	< 50

The chemical composition of the as-built parts has been investigated by Leco, with a particular attention to the interstitial elements. The oxygen and nitrogen contents have been analyzed by gas fusion in a Leco TC400 analyzer, while carbon and hydrogen contents have been analyzed by combustion and by IR spectroscopy in a Leco CS125 and Leco TCH600 analyzer, respectively.

## 4.2 Process parameters

As discussed in Chapter 1, the suitable control of the process parameters is fundamental for the obtaining of a fully dense material. Changing from material to material, these parameters have to be properly combined.

Concerning the production of Ti-6Al-4V by Electron Beam Melting, it has been carried out in vacuum (in the chamber, from  $5 \times 10^{-3}$  mbar at the start to  $2 \times 10^{-5}$  mbar at the end of the process) in an Arcam EBM S12. The parts have been built up in layers of 100  $\mu\text{m}$  thickness; the beam diameter was 2 mm and its power was 3 kW.

The Ti-6Al-4V SLM parts have been produced in an EOS EOSINT M 270 machine. A power of 170 W and a scan speed of 1125 mm/s have been used. Parts were built under a flux of Ar protective atmosphere (40 l/min), with a beam diameter of 500  $\mu\text{m}$  for a melt pool diameter of 150  $\mu\text{m}$ .

For the production of the ASTM F75 alloy by Electron Beam Melting, the settled beam power was 3 kW, for a beam diameter of 2 mm. The process has been performed in vacuum (between  $10^{-3}$  and  $10^{-5}$  mbar, varying as for Ti-6Al-4V). Layer thickness was 70  $\mu\text{m}$ .

Finally, regarding the 17-4 PH grade produced by Selective Laser Melting, it has been built using a nominal beam power of 195 W and a beam diameter of 500  $\mu\text{m}$ . The melt pool diameter was 150  $\mu\text{m}$ . Parts have been produced under a flux of nitrogen protective atmosphere (40 l/min).

When the geometry of the parts is long and narrow, the parts can be built essentially arranging the main axis along the working plate (horizontal orientation) or perpendicularly to it (vertical orientation). Evidently, the stress state and the interlayer defect probability are influenced by this choice. In other words, if the process parameters are not well arranged (i.e., production defects between layers are present), the number of layers can be critical for the presence of defects. Statistically, in fact, larger the number of layers, larger the probability to have incidence of defects. On the other hand, the effect of the thermal stress is less sensitive if the samples are free to deform, i.e. if the samples are vertically layered and only a small area is welded to the working plate. Vertical orientation, however, can result in larger deformations of the part after building. Finally, it is obvious to say that the building direction is also related to the production times.

In the specific of the materials studied during this thesis work, the layering orientation

---

has been vertical for the materials produced by Electron Beam Melting and horizontal for the materials produced by Selective Laser Melting. In SLM, in fact, thermal stresses are higher, as well as (consequently) thermal strains. This causes larger deformations of the parts. If the parts are built up as horizontally welded to the working plate, the deformation is controlled, even if the final removal of the parts from the plate could result difficult (i.e., it could require a stress relief treatment before the removal itself).

### **4.3 Microhardness and hardness**

The microhardness tests have been performed under a Paar MHT-4 Vickers micro-indenter. The samples have been prepared through the classical metallurgical preparation (i.e., polishing and eventually etching). A 0.050 kg load has been applied for a time of 10 s. A minimum of 7 and a maximum of 20 indentations (depending on data scattering) have been executed for every tested sample.

The hardness tests have been carried out under an EmcoTest M4U 025 Rockwell indenter. The samples have been prepared by surface polishing. During Rockwell indentation, a pre-load of 10 kg is applied for 2.5 s; then, a load of 150 kg is applied for 2.5 s. A minimum of 3 and a maximum of 10 indentations (depending on data scattering) have been executed for every tested sample.

Mean values and standard deviations have been calculated for every data batch.

### **4.4 Light Optical Microscopy (LOM)**

A Zeiss Light Optical Microscope has been used for the optical characterization of the material microstructures. Digital images have been acquired by a Leica DC300 system connected to the microscope's optical system.

The samples have been prepared through lapping and polishing with abrasive papers and diamond cloths. The samples have then been etched. The procedures for every material are summarized in Table 4.6.

Table 4.6. Summary of the polishing stages and procedures applied to the studied materials.

	<b>Ti-6Al4V</b>	<b>ASTM F75</b>	<b>17-4 PH</b>
<b>Papers</b>	120	120	120
	500	500	500
	800	800	800
	1200	1200	1200
	4000	4000	4000
<b>Cloths</b>	3 $\mu\text{m}$ dedicated	6 $\mu\text{m}$ 3 $\mu\text{m}$ 1 $\mu\text{m}$	6 $\mu\text{m}$ 3 $\mu\text{m}$ 1 $\mu\text{m}$
	<b>Etchant</b>	Kroll's reagent	electrolytic modified Fry's reagent

The diamond cloth used for the polishing of Ti alloys is a dedicated 3  $\mu\text{m}$  cloth coupled with a Struers OP-S suspension added with hydrogen peroxide and hydrogen nitride.

An electrolytic etching has been carried out on the Co alloy, applying a potential difference of 4 V for a time of 4-20 s. The electrolytic etching has been performed in a water solution of nitric acid (4,5vol%) and hydrogen peroxide (1,5vol%).

## 4.5 Scanning Electron Microscopy (SEM) and Transmission Electron Microscopy (TEM)

A Philips XL30 Scanning Electron Microscope (SEM), operating in high vacuum atmosphere, has been suited for the observation of microstructural details (e.g., carbides in CoCrMo alloy) and of fracture surfaces. Secondary Electrons (SE) and Back-Scattered Electrons (BSE) have been used. Samples for the microstructural analysis were incorporated in polymeric resin, polished, etched and metallized. Samples for the fracture surface were cut from the broken fragments of the tested tensile specimens.

A Philips CM12 Transmission Electron Microscope (TEM) has been employed in the analysis of microstructural features. The TEM operated at 120 kV. TEM foils (discs 3 mm in diameter) have been mechanically ground to a thickness of about 80  $\mu\text{m}$  and then twin jet electropolished in a solution of perchloric ethanol at -25 °C and

---

electrochemically etched in a Fischione apparatus.

## 4.6 Differential Scanning Calorimetry (DSC)

The Differential Scanning Calorimetry (DSC) analyses have been carried out in a Netzsch 409-PC apparatus. Alumina crucibles have been employed. If not differently specified, a heating rate of 20 °C/min and a cooling rate of 50 °C/min have been applied, and a constant argon flux (100 ml/min) has been insufflated. A subtraction curve has been acquired on the empty crucible for each measurement.

## 4.7 Dilatometry

The dilatometric analyses have been performed in a Bähr DIL 805 dilatometer. Specimens were 10 mm long, with a squared section (5x5 mm<sup>2</sup>). Specimens were heated by induction and cooled by insufflating gas through proper holes arranged on the inductor itself. If not differently specified, the cooling gas was nitrogen. The sample temperature was controlled by mounting an S thermocouple on the sample itself. Thanks to the temperature control and the cooling system, the instrument allows the application of very high cooling rates (i.e., 100 °C/s and higher); so, it is suitable for reproducing large undercoolings and also for “freezing” the microstructures characterizing a specific temperature.

The measurement atmosphere was vacuum (10<sup>-5</sup> mbar) for all the materials. In fact, in the case of a N<sub>2</sub> backfilling, nitrogen could interact with them, affecting the measurement results. In the case of the ASTM F75 alloy, at high temperature N<sub>2</sub> could act as a substitutional element for carbon, altering the phase composition and promoting the formation and stabilization of the fcc phase [1]. As well, nitrogen can promote the precipitation of M<sub>6</sub>C carbides rather than M<sub>23</sub>C<sub>6</sub> [2]. Actually, also vacuum could be critical for carbon depletion on the surface of the CoCrMo; however, the comparison between the ASTM F75 alloy treated in vacuum and the same alloy treated in a backfilling of argon removed possible doubts, since their carbon content after a heat treatment up to 1150 °C is the same.

## 4.8 Heat treatments

Eventual heat treatments have been executed, after the processes, on the as-built materials. Sometimes they are necessary in order to relieve the residual stresses. Besides, they can be required by the customers, since they are the usual procedure after traditional processing (e.g., hiping after casting). In the present thesis work, heat treatments have also been carried out with the aim of making the microstructure of the as-built material to change.

Hipping at  $915\pm 10$  °C for  $120\pm 15$  min, under an isostatic pressure of  $1000\pm 50$  bar, has been carried out on Ti-6Al-4V alloy produced by Electron Beam Melting.

Hipping has also been carried out for 240 min at a temperature of 1200 °C, under a pressure of 1000 bar, on ASTM F75 alloy produced by Electron Beam Melting.

Several heat treatments have been carried out in a TAV Minijet HP vacuum furnace on Ti-6Al-4V alloy produced by SLM, ASTM F75 alloy produced by EBM and 17-4 PH Stainless Steel produced by SLM. They have been performed in vacuum (around  $10^{-3}$  mbar) or in a partial pressure (backfilling) of argon (100-200 mbar). The backfilling has in particular been used for the heat treatments on the 17-4 PH grade. A heating rate of 15 °C/min or 20 °C/min has been applied, while the cooling has been obtained by the introduction of high pressure gas in the chamber. This pressure varied from 2 bar to 8 bar. In correspondence with the pressure and the part geometry, the cooling rate varied between 5 °C/s and 20 °C/s. Details on the single heat treatments will be given in the specific sections.

## 4.9 X-Ray Diffraction (XRD) and neutron diffraction spectroscopy (SMARTS)

X-Ray Diffraction (XRD) analysis was done using a Cu- $k\alpha$  source ( $\lambda=1.5418$  Å), and an Image Plate (IP) over the  $2\theta$  range from 30° to 120°, in reflection geometry. The experimental patterns were elaborated with the Rietveld method using the MAUD (Materials Analysis Using Diffraction) software [3,4].

Quantitative phase analysis (QPA) and line profile analysis (LPA) were performed to account the volume fractions of each constituent, the crystallites size and microstrain,

---

the dislocation density and the stacking fault or twin probability.

Planar defects (i.e., intrinsic and extrinsic stacking faults and twins) were calculated using the Warren approach [5] incorporated into a Fourier-series-based Rietveld algorithm.

In-situ neutron diffraction analysis has been carried out at the Spectrometer for Materials Research at Temperature and Stress (SMARTS) in the Lujan Neutron Scattering Center in Los Alamos, NM. In-situ analyses are possible because neutrons are highly penetrating, and then a sample environment can be utilized [6]. Moreover, due to their high penetration, neutrons allow the obtaining of a measurement representative of the bulk rather than the surface behaviour. Neutron diffraction gives independent information for each present phase and allows the determining of anisotropic responses to applied loads along various crystallographic planes [7,8]. The geometric setup of SMARTS allows for simultaneous measurements in longitudinal and transverse directions. Two detector banks, in fact, simultaneously measure the diffraction patterns at scattering angles of  $\pm 90^\circ$  (Fig. 4.1). In-situ measurements on 17-4 PH Stainless Steel produced by SLM have been carried out both during loading and on heating. Diffraction patterns have been acquired on loading at 0%, 0.4%, 1% and 2% of elongation, and then every 2% of elongation up to 26%. In a different measure, diffraction patterns have been acquired on cooling at 750 °C, 700 °C, 600 °C, 500 °C, 400 °C, 300 °C, 200 °C, 150 °C, 125 °C, 100 °C, 90 °C, 80 °C, 70 °C, 60 °C, 50 °C, 40 °C and 30 °C.

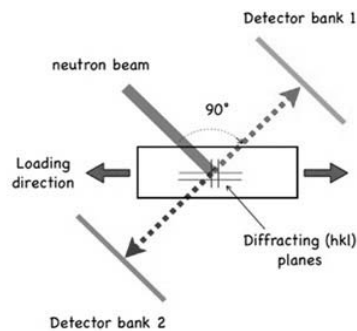
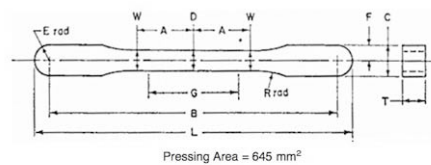


Figure 4.1. Geometric setup of SMARTS: two detector banks simultaneously measure the diffraction patterns at scattering angles of  $\pm 90^\circ$ .

## 4.10 Tensile testing

Tensile tests have been carried out using an Instron 8516 servo-hydraulic machine on samples machined from bars built up perpendicularly (in SLM) or parallelly (in EBM) to their main axis. Specimens had rectangular cross section, with an overall length of 89.64 mm and a reduced section length of 31.76 mm, according to the ASTM E8M standard. A 0.2 mm/min cross-head speed has been applied. An axial extensometer has been applied for the elongation measurement. The gauge length was 12.5 mm. A minimum of 5 specimens has been employed for each tested batch.

As stated in Chapter 3, the reference for the tensile properties of the biomedical alloys employed in surgical implants is the ISO 6892 standard. However, this gives generic suggestions about the geometry of the samples and the conditions (e.g., cross-head speed). Since the ISO 6892 standard totally complies with ASTM E8M standard, which is more indicative, the sample geometry was chosen from those there reported. In particular, the geometry indicated for Powder Metallurgy products was used (Fig. 4.2).



NOTE 1—Dimensions specified, except *G* and *T*, are those of the die.

Dimensions, mm	
<i>G</i> —Gage length	25.40 ± 0.8
<i>D</i> —Width at center	5.72 ± 0.03
<i>W</i> —Width at end of reduced section	5.97 ± 0.03
<i>T</i> —Compact to this thickness	3.56 to 6.35
<i>R</i> —Radius of fillet	25.4
<i>A</i> —Half-length of reduced section	15.88
<i>B</i> —Grip length	80.95 ± 0.03
<i>L</i> —Overall length	89.64 ± 0.03
<i>C</i> —Width of grip section	8.71 ± 0.03
<i>F</i> —Half-width of grip section	4.34 ± 0.03
<i>E</i> —End radius	4.34 ± 0.03

Figure 4.2. Geometry of the tensile specimens (from ASTM E8M standard: standard flat unmachined tension test specimen for Powder Metallurgy products).

The tensile properties of the alloys have been inferred by their stress-strain curves following the prescriptions of the ASTM E8M standard. Elastic Modulus has been evaluated as the slope of the line that fits the elastic step of the stress-strain curve. Yield stress has been calculated as the intersection between the stress-strain curve and

---

a line, parallel to the elastic step, horizontally shifted by a 0.2% of strain (offset value). Upper yield point and lower yield point have been determined as the first zero slope and the onset of uniform strain hardening, respectively. Ultimate Tensile Strength has been obtained as the higher stress value in the engineering stress-strain curve. Finally, elongation to failure has been evaluated as the maximum percentage strain in the engineering stress-strain curve.

## 4.11 Fatigue testing

Fatigue tests have been carried out in 4 points bending mode, at a frequency of 30 Hz and a load ratio (R) of -1. The geometry suggested by the ISO 3928 standard has been adopted for the samples (Fig. 4.3).

In order to evaluate the fatigue limit at 50% of failure probability, a statistical staircase method has been adopted. The method follows the indication of MPIF 56 standard; it consists in a staircase approach, which allows the statistical determination of the mean endurance limit.

First of all, a run-out number of cycles is fixed. In the present thesis work, this number is  $2 \times 10^6$  cycles. The method suggests to start from a predicted limit, which is about 0.3-0.5 times the known tensile strength. If the first specimen, tested at the predicted limit, fails in less than the run-out number of cycles, the stress for the subsequent specimen is decreased by a certain step; conversely, if the specimen survives the stress, the next specimen (which is not the same that survived) is tested at a stress higher by one step.

In the present thesis work, the size of one step has been chosen to be 15 MPa; lowering the stress, the number of steps of reduction, depending on the failure number of cycles, has been: 4 (60 MPa) for 0 to 100000 cycles, 3 (45 MPa) for 100000 to 200000 cycles, 2 (30 MPa) for 200000 to 300000 cycles, 1 (15 MPa) for over 300000 cycles.

The resolution of a quite complex statistical table with the collected data allows the obtaining of the mean endurance limit (50% survival) and the 10% and 90% survival stresses.

The staircase method has been applied to 15 samples for each batch.

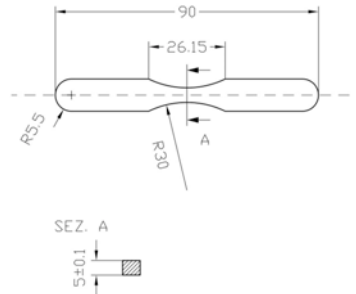


Figure 4.3. Geometry of the fatigue specimens (from ISO 3928 standard).

## 4.12 Density

The density of the produced materials has been determined by means of the Archimede's principle. Since the relative density of the as-built materials approaches the 100%, it can be calculated on the basis of two weighing: the former (dry) in air, the latter (wet) in water. The measurements have been performed using a Gibertini E42 balance.

---

## References

- [1] Z.F. Zhou, Y.D. Fan, Study of Co-Cr films deposited by magnetron sputtering under different nitrogen partial pressures
- [2] J. Escobedo, J. Mendez, D. Cortès, J. Gòmez, M. Mendez, H. Mancha, *Mater. Design* 17(2) (1996) 79
- [3] L. Lutterotti, S. Matthies, H.R. Wenk, A.S. Shultz, J.W. Richardson, *J. of Appl. Phys.* 81 (1997) 594
- [4] I. Lonardelli, H.R. Wenk, L. Lutterotti, M. Goodwin, *J. of Synch. Rad.* 12 (2005) 354
- [5] B.E. Warren, *Prog. Met. Phys.* 8 (1959) 147
- [6] P.K. Liaw, H. Choo, R.A. Buchanan, C.R. Hubbard, X.L. Wang, *Mat. Sci. Eng.* 437A (2006) 126
- [7] P.K. Liaw, H. Choo, R.A. Buchanan, C.R. Hubbard, X.L. Wang, *Mat. Sci. Eng.* 437A (2006) 126
- [8] D. Dragoi, E. Üstündag, B. Clausen, M.A.M. Bourke, *Scripta Materialia* 45 (2001) 245

## Chapter 5

# Ti-6Al-4V in Rapid Manufacturing

### 5.1 Microstructures

Traditionally, Ti-6Al-4V biomedical parts are processed by hot working and machining of wrought semi-products. Among the near-net-shape technologies, investment casting and, to a less extent, metal mold casting are used; in this case, the as-cast microstructure can only be modified by heat treatment. An alternative near-net-shape route is Powder Metallurgy: near-fully dense (with density between 99% and 100% of the theoretical one) parts are produced by Metal Injection Moulding of powders. Annealing or HIP can follow the processes, in order to reduce the porosity and/or stabilize the martensite. As a consequence of this custom, resulting microstructures for Ti-6Al-4V are coarse and, depending on the treatment temperature and conditions, lamellar or globular. The microstructure is determined by both strain rate and temperature, which influence dynamic and static recrystallization, and by the subsequent cooling, changing from lamellar to acicular on increasing the cooling rate. A primary globular  $\alpha$  phase (Fig. 5.1) can as well come from hot working, possibly followed by annealing [1].

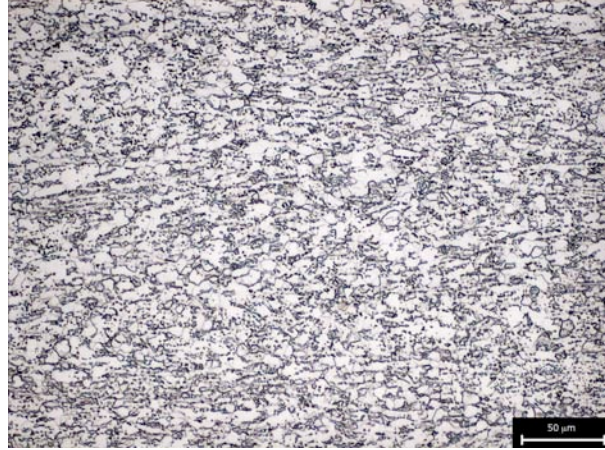


*Figure 5.1. Example of  $\alpha$ -globular microstructure, obtained by cooling from  $\alpha+\beta$  field in presence of deformation; equiaxed  $\alpha$  grains are distributed in a biphasic matrix.*

The microstructure reported in Figure 5.1 makes reference to a wrought and annealed bar. It contains the 8% of  $\beta$  phase (as confirmed by XRD analysis), mainly retained (on cooling) between  $\alpha$  globular grains.

In the case of the formation of globular  $\alpha$ , deformation has a noticeable effect on microstructure, as well as temperature. The explanation of the role of deformation is developed in terms of driving forces. We have to consider that, during hot working of Ti grade 5 alloy and subsequent annealing, either dynamic or static phenomena take place. The morphological changes of the material, in both cases, are initially associated with the formation of sub-structures within the pre-existing  $\alpha$  platelets. The first step toward the break up of the starting microstructure is the formation of low- and high-angle boundaries across the pre-existing  $\alpha$  platelets [2]. This can be due to the recovery of the dislocations (faster than recrystallization). Under deformation, the recovery can be dynamic: dislocations are generated, but simultaneously annihilated [3]. Another source of sub-boundaries is the localization of shearing and the rotation of the  $\alpha$  platelets during deformation. In a second time, after the formation of the low- and high-angle boundaries, the penetration of  $\beta$  phase along the sub-boundaries can make the separation of the lamellae fragments complete. If the platelet thickness is large, the separation by  $\beta$  phase penetration is obviously more complicated. However, when penetration is limited, breaking up of the lamellae can occur by the

formation of high-angle  $\alpha/\alpha$  boundaries, as a result of the elimination of the low-angle boundaries, during annealing [2].

Concerning static globularization of Ti-6Al-4V alloy, it occurs mainly in two stages [4]: (i) the initial short-time segmentation of the  $\alpha$  lamellae by boundary splitting and edge spheroidization and (ii) the microstructural coarsening by termination migration and Ostwald ripening. Boundary splitting happens by the just described mechanisms; edge spheroidization is related to the reduction of the  $\alpha/\beta$  interface energy. Termination migration is related to the mass transfer from the curved edges of the lamellae to the flat edges. Ostwald ripening provides for large platelets to grow (thermodynamically driven) to detriment of small ones: smaller grains dissolve because of their higher dissolution potential (i.e., increased chemical potential), while coarser grains grow by material reprecipitation (reducing the interface area of the system). The time during which both the stages take place varies depending on the treatment temperature; however, the first stage gives a modest contribution to globularization (particularly in a lack of stored deformation): static globularization is mainly due to termination migration [5]. As stated above, the formation of low- and high-angle boundaries is related to recovery mechanism. Since the recovery is due to cross slip, the globularization kinetic is controlled by this mechanism [3].

In the different, specific case of MIM, microstructure is globular-lamellar, since the cooling rate from the sintering temperature is basically slow. After EBM or SLM, evidence is different. According to the considerations about the characteristics of the RM technologies, it is not so surprising to notice fine microstructures in the processed material. There is, however, a difference between the material produced by Selective Laser Melting and the material produced by Electron Beam Melting. We have to consider, in fact, that the extent of the undercooling is not the same: the pre-heating that takes place during the EBM process (see Paragraph 1.9) makes the thermal gradient less severe. The difference is well reflected in the resulting microstructures.



*Figure 5.2. Microstructure of Ti-6Al-4V alloy produced by Electron Beam Melting; (b) acquired at a higher magnification.*

Concerning EBM, an acicular, very fine microstructure is observable. The microstructure principally consists of  $\alpha$ -phase fine lamellae, organized in a basket-weave morphology. This microstructure is the result of the rapid solidification and the subsequent annealing due to the temperature of the working zone. It is reasonable to hypothesize that, at first, a martensitic hcp phase forms, since the large undercooling promotes the formation of a metastable phase through a non-diffusive mechanism. Then, the permanency at a temperature above 600 °C makes the stabilization of the microstructure possible. As an evidence of this interpretation, there is the sporadic

presence, in the microstructure, of areas showing pre-existing martensitic packages, but coarse needles (Fig. 5.3).

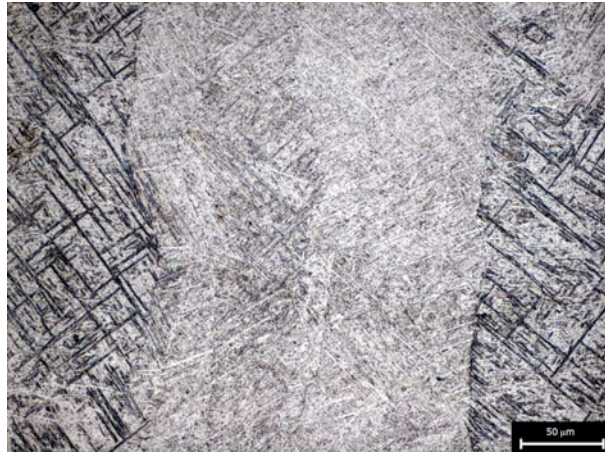


*Figure 5.3. Areas showing pre-existing martensitic packages (but also coarse needles) in Ti-6Al-4V produced by Electron Beam Melting.*

A Quantitative Phase Analysis of an XRD pattern acquired on the material (Fig. 5.4) allows the individuation of a 7% of bcc  $\beta$  phase in an hcp matrix. The percentage accords with what can be expected by the alloy. As stated above, considering that the parts are built up, because of the pre-heating, at an average temperature between 600 °C and 700 °C, it may be concluded that the formerly produced martensite (the solidification rate of the melting pool is very high) is then transformed in an  $\alpha+\beta$  mixture by the soaking at the process temperature [6].

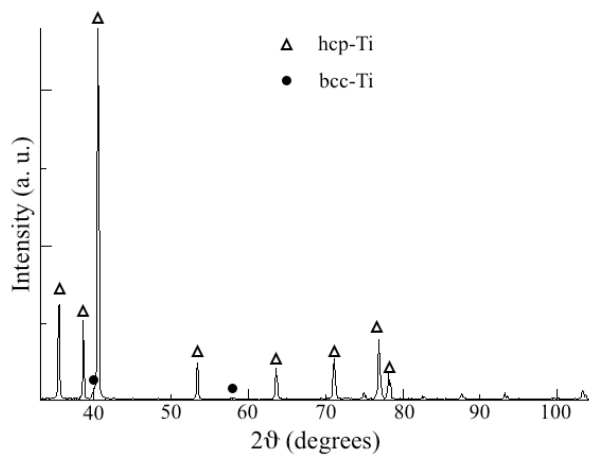


Figure 5.4. XRD pattern acquired on Ti-6Al-4V produced by Electron Beam Melting.

As discussed in Chapter 3, the microstructure of the material produced by Electron Beam Melting does not satisfy the standard prescriptions. In particular, the microstructure of Ti-6Al-4V produced by EBM complies with micrograph A23 of the ISO 20160 standard, which is classified as unacceptable.

The as-built material coming from Selective Laser Melting process has a finer microstructure, in which a martensitic hcp phase follows the orientations expected for the crystallographic relations between  $\alpha$  and the prior  $\beta$  phase (cf. Paragraph 2.1.1). Packages of needles are recognizable in the microstructure (Fig. 5.5).



Figure 5.5. Microstructure of Ti-6Al-4V alloy produced by Selective Laser Melting; (b) acquired at a higher magnification.

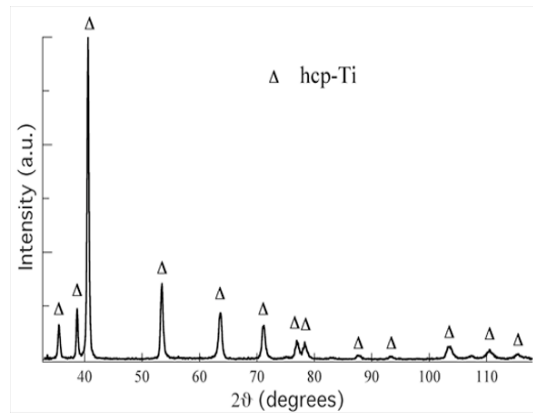


Figure 5.6. XRD pattern acquired on Ti-6Al-4V produced by Selective Laser Melting.

---

The XRD pattern, in this case, reflects only the peaks related to the hcp phase (Fig. 5.6): no  $\beta$  phase is present. It is indeed quite complicated to individuate and distinguish between  $\alpha$  and  $\alpha'$ : they both have a hexagonal lattice, and similar cell parameters [7-9]. However, it is reasonable to expect that hexagonal phase in the material will be martensite, since the large undercooling can promote a martensitic transformation (and  $\beta$  formation is inhibited). Differently from EBM, where the formerly produced martensite is transformed into  $\alpha+\beta$  mixture because of the stabilization induced by the process temperature, here the metastable martensite remains the only phase present at room temperature.

## 5.2 Mechanical properties of the as-built material

The peculiar microstructures intrinsic of the Rapid Manufacturing processes strongly affect the mechanical properties of the material.

From the point of view of the tensile properties, Ti-6Al-4V is usually characterized by a good strength (referred to its density). Yield stress ( $\sigma_y$ ) falls between 800 MPa and 925 MPa, while Ultimate Tensile Strength (UTS) is arranged between 900 MPa and 1025 MPa. The difference between UTS and  $\sigma_y$  is slight because the strain hardening rate of titanium and its alloys is small: the plastic flow is basically horizontal. This also signifies that, after yielding, a small increase in stress results in a large increase in strain. Concerning Elastic Modulus (E), 115-120 GPa are typical values. Elongation ( $\epsilon$ ) is generally comprised between 12% and 28%, depending on the microstructure and the embrittling oxygen content.

Regarding fatigue endurance, the limit at  $10^7$  cycles for the wrought alloy is included between 400 MPa and 700 MPa. As discussed in Paragraph 2.1.2, fatigue resistance strongly depends on the microstructure, varying from globular to lamellar.

### 5.2.1 Tensile properties

Requirements for the application of Ti-6Al-4V alloy in the biomedical field, referring to ISO 5832-3 standard, impose limits for yield stress (780 MPa), Ultimate Tensile

Strength (860 MPa) and elongation (10%). These values, making reference to the wrought material, are easily reachable by a solid material. Nevertheless, defects in the bulk could affect the soundness of the parts.

Two different kinds of defects involve Ti-6Al-4V produced by RM technologies. The first, regarding Electron Beam Melting, consists in the localized evaporation of the melted pool because of the temporary stop of the beam on a single spot. Obviously, such a problem is the consequence of a software mistake, depending on the software itself rather than on the control system. The result is the formation of a round hollow; these cavities are well recognizable on the fracture surface of the broken tensile samples (Fig. 5.7).

As anticipated, the problem is restricted to Electron Beam Melting, because of a technological/practical reason related to the controlling software. At this time, however, this limit has been overcome thanks to a better software control (i.e., through a new software) of the process.



been changed from 60% to 100%. The sequence of the microstructures and soundness obtained by this way is reported in Figures 5.8-5.9.



Figure 5.8. Microstructure and soundness obtained on Ti-6Al-4V applying 225 mm/s scanning speed and 60% power.



Figure 5.9. Microstructure and soundness obtained on Ti-6Al-4V applying 225 mm/s scanning speed and (b) 70%, (c) 80%, (d) 90%, and (e) 100% power.

Then, fixed the beam power at 60%, the scanning speed has been varied from 225 mm/s to 125 mm/s. The obtained results are reported in Figure 5.10, with a reference on Fig. 5.8.



Figure 5.10. Microstructure and soundness obtained on Ti-6Al-4V applying 60% power and (b) 200 mm/s, (c) 175 mm/s, (d) 150 mm/s scanning speed, and (e) 125 mm/s scanning speed.

Evidently, an increase in the specific energy involved in the process, coming from a higher power or a slower scanning speed, results in the substantial improvement of the material soundness.

Nevertheless, another mechanism is responsible for the second kind of defects (i.e. related to insufficient energy): incomplete homologous wetting. In this case, sharpened cracks are visible on the etched metallographic sections (Fig. 5.11); these are visible also on the fracture surfaces of broken tensile specimens (Fig. 5.12). If a balling mechanism has taken place, spherical particles can be detected inside the crack (Fig. 5.13). In particular, Figures 5.12-5.13 report the fracture surface of tensile samples produced by Selective Laser Melting in a preliminary production stage, when the process parameters still were not appropriately chosen.



*Figure 5.11. Sharpened cracks visible on the etched metallographic sections of Ti-6Al-4V produced by Selective Laser Melting.*

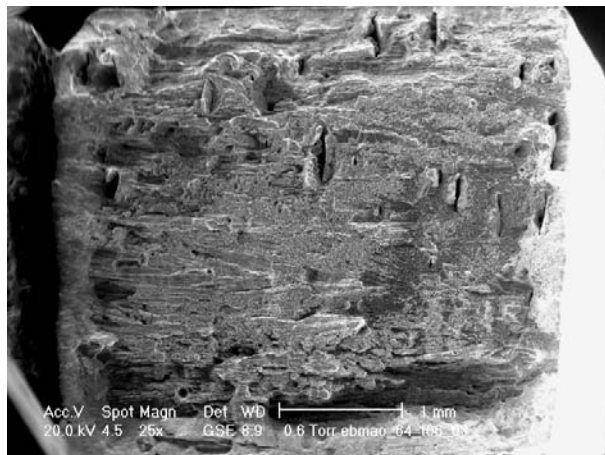


*Figure 5.12. Sharpened cracks visible on the fracture surface of a broken tensile specimen of Ti-6Al-4V produced by Selective Laser Melting.*

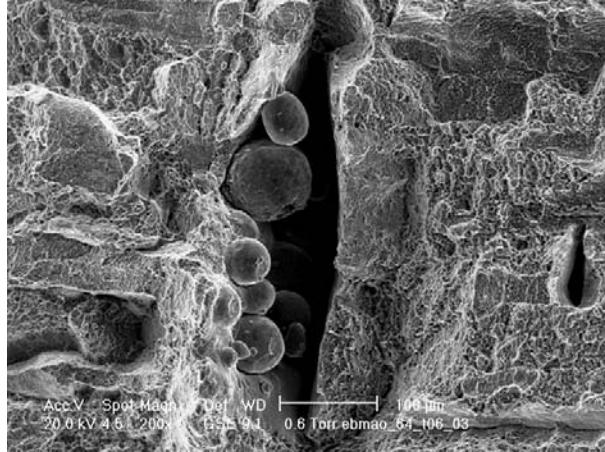


Figure 5.13. Fracture surface of a broken tensile specimen of Ti-6Al-4V produced by Selective Laser Melting; particular: balling mechanism has taken place, spherical particles can be detected inside the crack.

Concerning the cracks, a discussion has been conducted on their genesis. From a chemical point of view, the presence of interstitial elements (and in particular oxygen and carbon) can be critical for the ductility of the alloy. In fact, these elements are  $\alpha$ -stabilizers (and  $\alpha$  phase is less ductile than  $\beta$ ). Moreover, oxygen distorts the hcp lattice, limiting the mobility of dislocations and embrittling the material [10]. Nevertheless, the chemical compositions of the parts produced by EBM and SLM match the standard requirements (ISO 5832-3), as shown in Table 5.1. These values are precautionary in terms of mechanical properties, and then a strong effect of the interstitial element on the ductility of the alloys produced by Electron Beam Melting and Selective Laser Melting can be excluded.

Table 5.1. Oxygen and carbon contents in Ti-6Al-4V produced by Electron Beam Melting (EBM) and Selective Laser Melting (SLM); standard requirements reported.

	EBM	SLM	ISO 5832-3
%O	0,1313±0,0129	0.1900±0.0200	< 0.2000
%C	0,0589±0,0062	0.0280±0.0031	< 0.0800

In a first moment, the hypothesis about the formation of the cracks was founded on the residual stresses. The presence of cracks in the bulk, in fact, would be suitable with the store of plastic deformation in the material: after removal from the working plate, when the thermal stresses are relaxed (inducing plastic deformation), cracks could form. However, in such a situation we should expect the cracks to grow over several layers perpendicularly to the layers plane. Cracks are, on the contrary, aligned along the layers direction. Moreover, cracks appear to be arranged in planes, corresponding to the interfaces between layers. Finally, as previously advanced and shown in Figure 5.13, spheroidal particles can be detected inside some cracks. So, the formation of cracks during processing is ascribed to issues regarding the process itself.

The presence of defects is then clearly related to unsatisfactory process control. From this point of view, in prospect the studied RM technologies are promising and reliable. No other defects, in fact, such as segregations, may be found; then, the proper control of the process parameters results in a fully dense, homogenous material.

When the material is sound, in both EBM and SLM productions it presents appreciable mechanical properties. In this connection, an example of the tensile response of the alloy produced by Electron Beam Melting is shown in Figure 5.14.

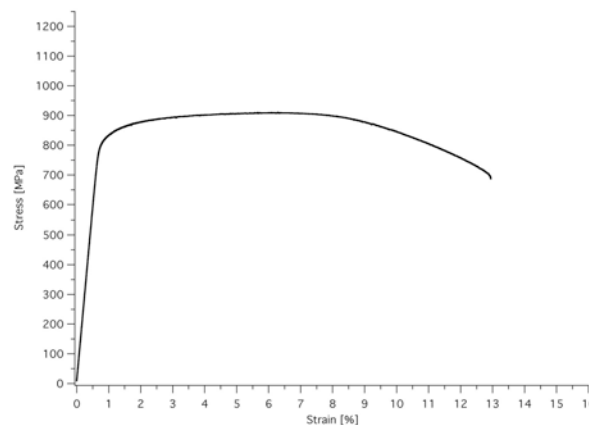


Figure 5.14. Stress-strain curve of Ti-6Al-4V alloy produced by Electron Beam Melting.

After yielding, the engineering curve exhibits an almost horizontal plastic step, with a nearly constant flow stress, up to necking.

Concerning the material coming from SLM technology, it has a quite different

behaviour on tensile testing (Fig. 5.15).

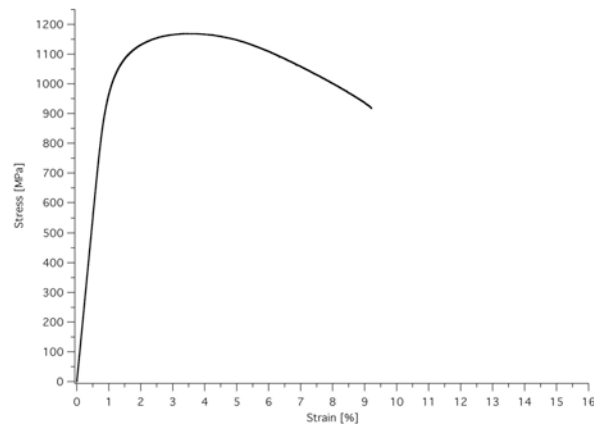


Figure 5.15. Stress-strain curve of Ti-6Al-4V alloy produced by Selective Laser Melting.

In this case, plastic instability starts rapidly after yielding, carrying to an engineering curve similar to those characteristic of ultrafine grained materials [11]. The combined effect of martensite and residual stress is responsible for ductility lower than expected for the alloy. Martensite, in fact, is more brittle than  $\alpha$  and  $\beta$  phases [12,13]. On the other hand, the residual stress can anticipate the limit for plastic fracture.

Collected over a number of specimens, the tensile properties of the two materials are summarized in Table 5.2. In the same table the tensile properties of the wrought and annealed alloy corresponding to the microstructure of Figure 5.1 are also reported.

Table 5.2. Tensile properties of Ti-6Al-4V alloy produced by Electron Beam Melting (EBM) and Selective Laser Melting (SLM); wrought and annealed material and standard requirements reported.

	EBM	SLM	wrought and annealed	ISO 5832-3
<b>Elastic Modulus [GPa]</b>	118±5	112±2	104±2	-
<b>Yield stress [MPa]</b>	830±7	1005±7	790±17	> 780
<b>Ultimate Tensile Strength [MPa]</b>	914±10	1166±3	872±7	> 860
<b>Elongation [%]</b>	13.1±0.4	8.9±0.2	18.1±0.8	> 10

The alloy produced by Selective Laser Melting reaches higher strength values, but contemporarily it is less ductile. Its ductility, moreover, is below the limit imposed by the reference standard. To tell the truth, both the materials produced by Rapid Manufacturing are less ductile than the wrought and annealed alloy, but also stronger.

## 5.2.2 Fatigue behaviour of the as-built materials

As anticipated, the fatigue endurance of Ti-6Al-4V alloy usually depends, once more, on the microstructure of the alloy itself.

Metals Handbook [1] furnishes reference values for the Wöhler diagrams of the alloy produced by different processes (Fig. 5.16).

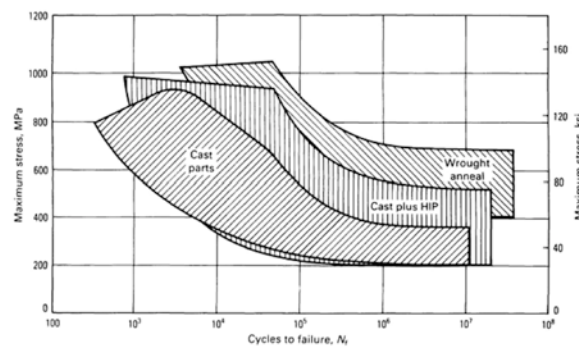


Figure 5.16. Reference values for the Wöhler diagrams of Ti-6Al-4V alloy produced by different common processes.

The better fatigue limit is guaranteed by the wrought and annealed material, which has a resistance higher than 400 MPa at 10 million cycles to failure. The logical reference for the alloy produced by EBM and SLM is just the wrought and annealed material. The staircase method described in Chapter 4, applied to the wrought and annealed alloy already subjected to tensile testing (see Paragraph 5.2.1, Tab. 5.2), returns a fatigue limit value, at 50% of resistance probability, corresponding to  $445 \pm 7$  MPa (Tab. 5.3). This limit is little scattered (as testified by the statistically calculated limits at 10% and 90% of resistance probability). When produced by Electron Beam Melting, the material reaches  $391 \pm 21$  MPa, while after Selective Laser Melting the material has

a 50% limit at  $381\pm 27$  MPa. Looking at the references, fatigue resistance of the as-built alloys is lower than that of the wrought and comparable with that of the as-cast materials.

*Table 5.3. Fatigue limits at 10%, 50% and 90% of resistance probability for Ti-6Al-4V alloy produced by EBM, SLM and hot working.*

	Limit at 10% of resistance probability	Limit at 50% of resistance probability	Limit at 90% of resistance probability
<b>Wrought and annealed</b>	445	$445\pm 7$	445
<b>Electron Beam Melting</b>	421	$391\pm 21$	361
<b>Selective Laser Melting</b>	421	$381\pm 27$	341

A forecast of the fatigue limit is usually given taking as a prediction the value of the yield stress multiplied by 0.3-0.5; both for EBM and SLM, the fatigue limit at 50% of resistance probability falls in the range between  $0.3\sigma_y$  and  $0.5\sigma_y$ . The range is respected even if the Ultimate Tensile Strength, rather than the yield stress, is taken into account (as suggested for certain materials, such as steels). However, the limit for the wrought and annealed alloy is higher, even if yield stress is contained. This can be attributed to the microstructure of the materials.

### 5.3 Thermal stability of the microstructures

Matching the standard prescriptions is the target of the producers of biomedical prostheses: parts can obviously be used for implants only if they satisfy the requirements. As a consequence, a study of the feasibility of this matching is necessary for manufacturing activities.

Problems regarding Ti-6Al-4V alloy produced by Electron Beam Melting or Selective Laser Melting are at first microstructural; concerning SLM material, it also has a problem related to ductility.

As anticipated in Chapter 3, the ISO 20160 standard makes reference to bar material

processed in the longitudinal direction. Implicitly, this is a wrought stuff. Consequently, contemplated microstructure go from globular  $\alpha$  to lamellar  $\alpha$  in large prior  $\beta$  grains. Only a few acicular microstructures are taken into account (and they are considered as unacceptable), because no acicular microstructure forms in common wrought products. Then, it is important to evaluate the possibility that the microstructure of the as-built material might change in the desired direction. The only way by which a microstructural evolution can be aided without affecting shape and finishing of the part is thermal treating. In the near-net shape RM technologies, then, the only practice chance to modify the microstructure is to apply a proper thermal treatment to the material. Starting from these considerations, a study of the thermal stability of the as-built microstructures has been carried out.

### **5.3.1 Microstructural thermal stability of Ti-6Al-4V produced by Selective Laser Melting**

As discussed in Paragraph 5.1, the microstructure of titanium grade 5 produced by Selective Laser Melting is out of equilibrium. Martensite, in fact, is a metastable phase: even if the necessary driving force is stored, it can transform in a stable  $\alpha+\beta$  microstructure only under activation.

In order to individuate transformation temperatures and phenomena occurring on heating, the alloy has been subjected to a Differential Scanning Calorimetry (DSC) and to a dilatometric analysis up above 1000 °C (i.e. in the  $\beta$  field). The DSC behaviour allows the individuation of two main peaks: the former between 500 °C and 800 °C, the latter approximately between 850 °C and 1000 °C (Fig. 5.17).

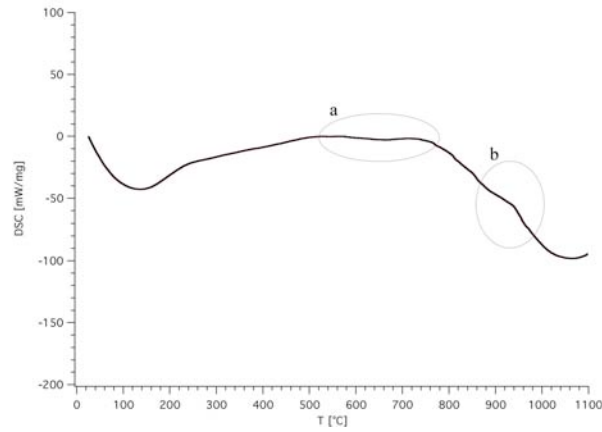


Figure 5.17. Differential Scanning Calorimetry (DSC) signal on heating acquired on Ti-6Al4V produced by Electron Beam Melting.

The signal collected during the same heating carried out in dilatometer exhibits two peaks in correspondence of the same ranges. In particular, the dilatometric differential rate shows an evident peak corresponding to the  $\alpha+\beta$  field (Fig. 5.18, b).

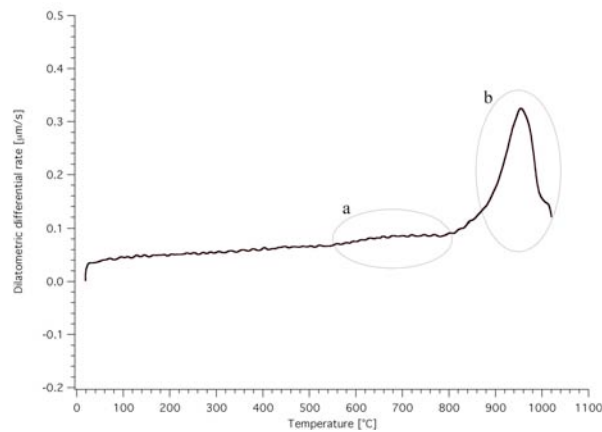


Figure 5.18. Dilatometric differential rate signal on heating acquired on Ti-6Al4V produced by Electron Beam Melting.

It is really expectable to individuate the peak associated to the phase transformation on heating in the nearby of 1000 °C. The transformation is slightly endothermic (Fig.

5.17, b). During it, the rate of variation of the dilatometric signal (Fig. 5.18, b) undergoes an increase, reaching its maximum in correspondence of 950 °C. Evidently, it can be noticed that, during the transformation from  $\alpha$  (hcp) to  $\beta$  (bcc) phase, the contribution of the transformation determines an accelerating in the dimensional variation; when the material is wholly composed by bcc phase, the dilatometric differential rate returns constant.

Concerning the first peak (Fig. 5.17, a), widely spread between 500 °C and 800 °C, it can be associated to both the precipitation of some  $\beta$  phase and the formation of a small amount of orthogonal  $\alpha''$  martensite. This is confirmed by an XRD analysis on a sample heated up to 800 °C (in dilatometer) and then quenched (Fig. 5.19).

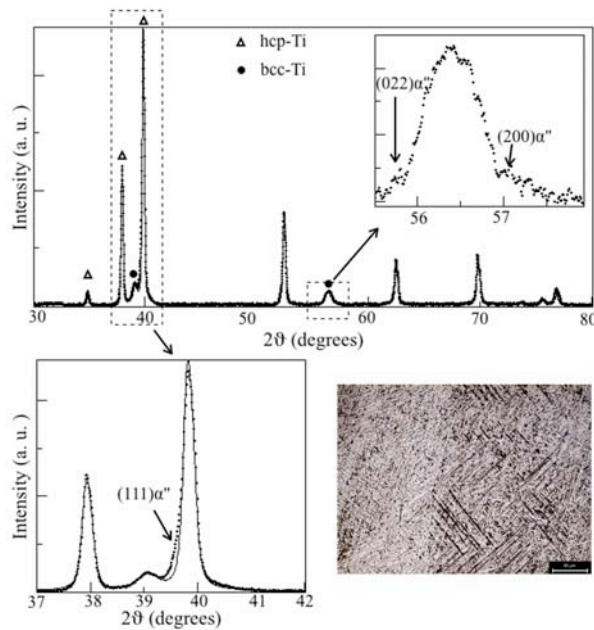


Figure 5.19. XRD pattern of Ti-6Al-4V produced by Selective Laser Melting, heated up to 800 °C and then quenched.

Regarding  $\alpha''$ , small shoulders are visible on the pattern before the third peak of hcp phase and around the second peak of bcc phase. Orthorhombic crystal structure is the result of the distortion of the hexagonal  $\alpha'$  martensite, occurring in alloys containing high solute amounts. The orthorhombic martensite is reported [12] to decompose by

---

spinodal decomposition upon annealing in the biphasic field. Decomposition results in the modulation of solute rich and solute poor  $\alpha'$  regions before the final precipitation of  $\beta$  phase. Furthermore, the precipitation of orthorhombic martensite upon aging of a supersaturated  $\alpha'$  phase has been suggested by Malinov et al. [9]. Related to these observations is the noticed effect of heat treating carried out at 550 °C. Such a temperature was chosen following the suggestions of the Metals Handbook: common aging after water quenching on Ti-6Al-4V alloys, in fact, is usually carried out at a temperature in a range between 480 °C and 595 °C [1]. The aging is performed with the aim of making the martensitic matrix formed during rapid cooling to transform into a mixture of  $\alpha$  and  $\beta$  phases. Since after SLM the alloy could be in the conditions of a solution treated and quenched material, an aging in this range might be efficient in order to stabilize the martensitic microstructure. Three different times have been chosen for treatment at 550 °C: 4 h, 12 h and 24 h. The obtained microstructures are reported in figure.



*Figure 5.20. Ti-6Al-4V produced by Selective Laser Melting and heat treated at 550 °C for 4 h (upper pictures), 12 h (middle pictures) and 24 h (lower pictures).*

After treatment at 550 °C, therefore, whatever the time may be, no change in the microstructural aspect of the material happens. According to this, the microhardness of the heat treated materials presents values similar to the as-built material's microhardness. In other words, even if the aging time changes, the microstructure remains martensitic (i.e., neither transformation into biphasic matrix nor coarsening of the fine lamellae occur).

Table 5.4. Microhardness obtained on Ti-6Al-4V produced by SLM and heat treated at 550 °C for 4 h, 12 h and 24 h.

	4 h	12 h	24 h
mHV [HV <sub>0.05</sub> ]	455±10	456±7	462±8

Moreover, also after heat treatment up to 800 °C the microstructure remains substantially the same (Fig. 5.19). The real microstructural change happens when the heat treatment is carried out at a temperature above the  $\alpha/\alpha+\beta$  transus. A treatment of 30 min at 950 °C, in fact, results in a significant evolution of the microstructure. After the treatment in the biphasic field, the morphology of the microstructure becomes basket-weave type: woven lamellae of  $\alpha$  phase constitute the overwhelming majority of the microstructure, but also an amount (~6%) of bcc phase is present, as confirmed by the XRD analysis (Fig. 5.21).

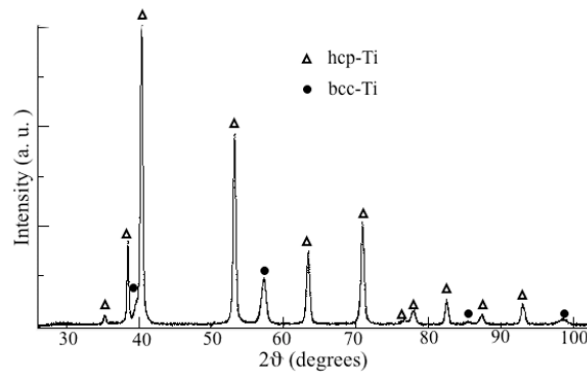
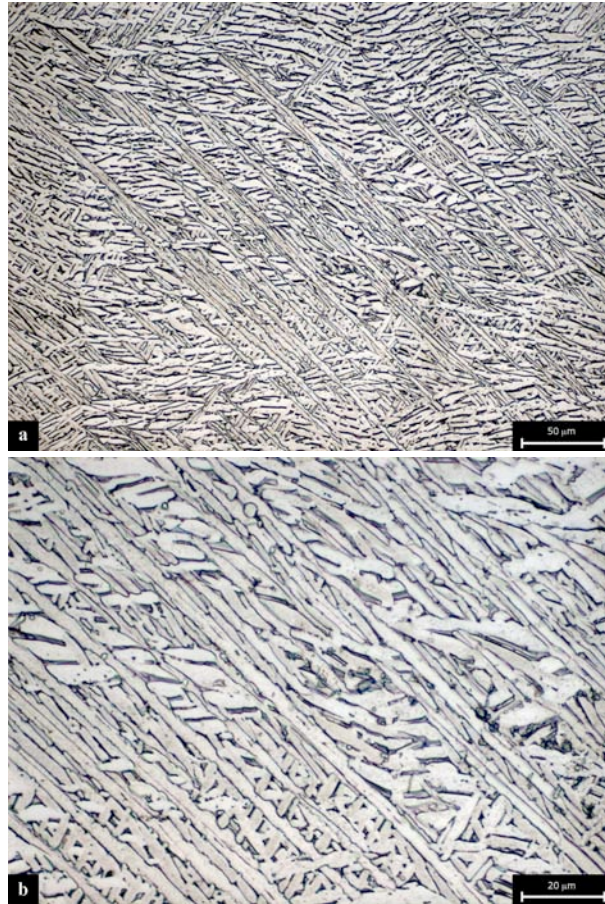


Figure 5.21. XRD pattern pattern acquired on Ti-6Al-4V produced by Selective Laser Melting and heat treated at 950 °C for 30 min.



*Figure 5.22. Microstructure of Ti-6Al-4V alloy produced by Selective Laser Melting and heat treated at 950 °C for 30 min; (b) acquired at a higher magnification.*

So the microstructure becomes biphasic, with columnar  $\alpha$ -phase crystals formed at the boundaries of the original martensitic plates and an  $\alpha+\beta$  mixture within. The microstructure is still quite different from the globular microstructure of a wrought alloy, since  $\alpha$  phase nucleates and grows in the interplate regions, developing a texture. In other words, there is a clear memory effect in the martensite-to-alpha transformation. In wrought alloy, instead,  $\alpha$  phase nucleates in the highly strained regions, which are homogeneously distributed in the cross section, and grows symmetrically; this leads to the globular microstructure.

In any case, the development of the biphasic microstructure improves the ductility of the alloy (Fig. 5.23). After the treatment, in fact, elongation exceeds the standard requirements (Tab. 5.5).

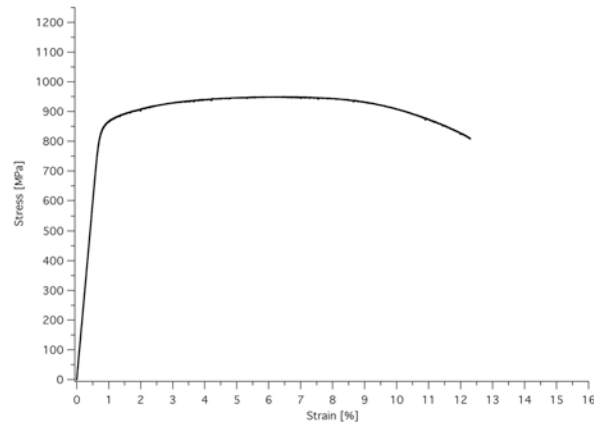


Figure 5.23. Stress-strain curve of Ti-6Al-4V alloy produced by Selective Laser Melting and heat treated at 950 °C for 30 min.

However, if the stabilization of the martensite has a beneficial effect on the ductility of the material, on the other hand it causes a slight reduction in yield stress and Ultimate Tensile Strength. Another difference is observable: after the heat treatment, plastic instability occurrence is delayed.

The tensile properties of the modified material are summarized in Table 5.5; the properties of the as-built material are reported as a comparison.

Table 5.5. Tensile properties of Ti-6Al-4V alloy produced by Selective Laser Melting and heat treated at 950 °C for 30 min, compared with those of the as-built alloy and standard requirements.

	h.t. SLM	SLM	ISO 5832-3
<b>Elastic Modulus [GPa]</b>	119±4	113±2	-
<b>Yield stress [MPa]</b>	858±1	1009±10	> 780
<b>Ultimate Tensile Strength [MPa]</b>	950±1	1175±15	> 860
<b>Elongation [%]</b>	12.2±0.2	8.6±0.4	> 10

Another important difference between the as-built and the heat treated materials regards the fatigue limit at 50% of resistance probability. The limit calculated for the heat treated material, in fact, is  $420 \pm 7$  MPa: it is shifted towards the fatigue limit registered for the wrought and annealed material. Considering the discussion reported in Paragraph 2.1.2, the result signifies that the coarsening of the microstructure has a major contribution to retarding the crack propagation, while its effect on crack nucleation is less important.

The obtained material represents a good equilibrium point. Its microstructure, however, still does not satisfy the requirements of the ISO 20160 standard.

Considering the discussion about globular microstructures faced in Paragraph 5.1, and in particular the comments concerning the driving force and the activation of the microstructural evolution, it is to note that a spur for changing is here present (contrarily to what happens for the EBM material, as will be demonstrated in Paragraph 5.3.2). In the alloy produced by Selective Laser Melting, the driving force is furnished by the microstrain accumulated during the process and by the metastability of the  $\alpha'$  phase; the heat treatment in the biphasic field activates the mechanisms for the evolution towards stable microstructure.

### **5.3.2 Microstructural thermal stability of Ti-6Al-4V produced by Electron Beam Melting**

As previously shown, the microstructure of Ti-6Al-4V alloy produced by EBM is acicular. Very fine  $\alpha$  needles are oriented along one of the twelve possible orientations (see Paragraph 2.1.1). This microstructure is the combined result of large undercooling and pre-heating characteristics of the process. As previously stated, because of the pre-heating, the material obtained by EBM undergoes a less severe thermal gradient (differently from what happens for SLM). As a consequence, the amount of residual stress is lower. Moreover, the thermal residual stress can be partially recovered by the permanence at quite high temperatures. Furthermore, the pre-heating is responsible for the formation of  $\beta$  phase.

Despite the good mechanical properties that is related to, the biphasic microstructure distinctive of the material produced by Electron Beam Melting is not foreseen by ISO 20160 standard. Then, a possibility of globularization must be investigated. As

---

discussed in Paragraphs 2.1.1 and 5.1, globularization is strongly affected by strain [14]. So, the role of the strain in the globularization of Ti-6Al-4V alloy produced by EBM and SLM has to be taken into account.

From a preliminary point of view, as for the SLM material, DSC and dilatometric analyses have been carried out (Figs 5.24-5.25). They are not surprising, having a behaviour similar to the one followed by the SLM material.

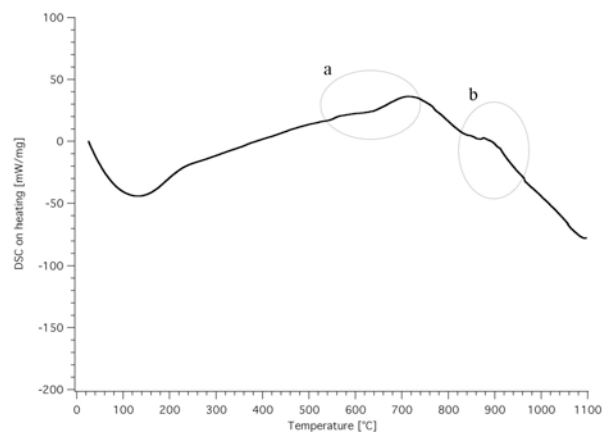


*Figure 5.24. Differential Scanning Calorimetry (DSC) signal on heating acquired on Ti-6Al-4V produced by Selective Laser Melting.*

Even in the curves referring to the alloy produced by EBM two peaks can be detected. They are approximately located in the ranges already pointed out for the SLM material.

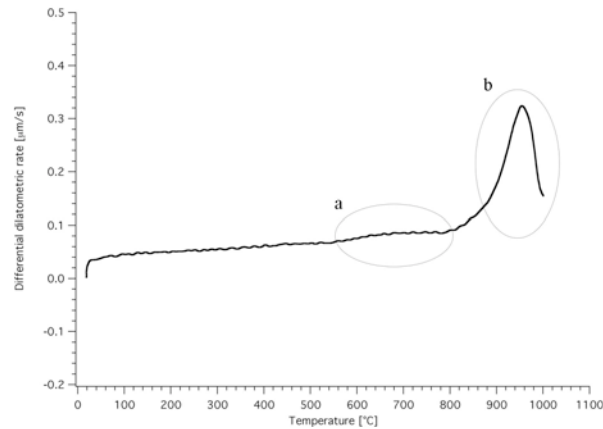
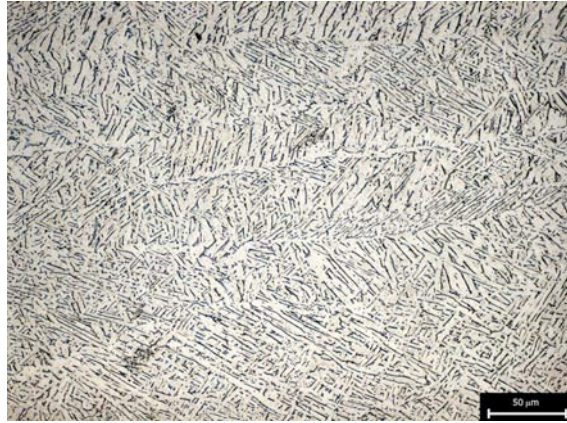


Figure 5.25. Differential dilatometric rate signal on heating acquired on Ti-6Al-4V produced by Selective Laser Melting.

After Electron Beam Melting an amount of bcc phase is formerly present in the as-built material. Consequently, the first peak can be related to the formation of a few more  $\beta$  phase and some orthorhombic martensite, as for SLM material.

Taking into account the similarity between the two materials, the common sense suggests to work above the  $\alpha/\alpha+\beta$  transus in order to obtain a sensitive modification of the microstructure.

For the biomedical applications, usually, a post-process HIPping is introduced in order to reduce the residual porosity of the part to be implanted. This becomes particularly significant for Ti-6Al-4V alloy produced by EBM, since this is already diffusely used for such applications. Moreover, HIPping can also have an industrial justification, helping in the reduction of the porosity described in Paragraph 5.2.1, when present. Consequently, a HIPping treatment in the biphasic field has been carried out.



*Figure 5.26. Microstructure of Ti-6Al-4V alloy produced by Electron Beam Melting and hipped in the biphasic field.*

The obtained result is reported in Figure 5.26: the acicular microstructure underwent a slight coarsening, but not a clean modification occurred.

The coarsening of the acicular  $\alpha$  lamellae is associated with a slight increase in elongation (Fig. 5.27) and a slight decrease in yield stress and Ultimate Tensile Strength, as inferable from Table 5.6. The difference in tensile properties is not pronounced in comparison with the as-built material. Nevertheless, the  $\sigma_y$  and the UTS of the hipped material lower towards the limits imposed by the ISO 5832-3 standard.

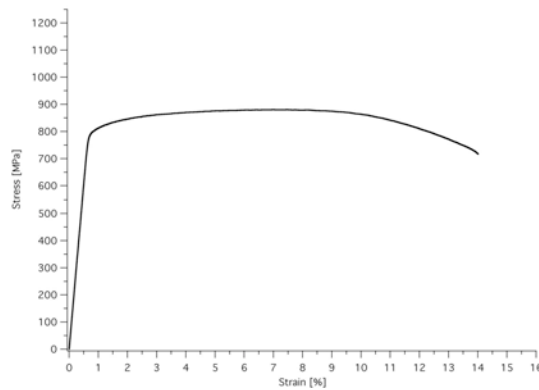


*Figure 5.27. Stress-strain curve of Ti-6Al-4V alloy produced by Electron Beam Melting and hipped in the biphasic field.*

Table 5.6. Tensile properties of Ti-6Al-4V alloy produced by Electron Beam Melting and hipped in the biphasic field, compared with those of the as-built alloy and standard requirements.

	hipped EBM	EBM	ISO 5832-3
<b>Elastic Modulus [GPa]</b>	117±4	118±5	-
<b>Yield stress [MPa]</b>	795±10	830±7	> 780
<b>Ultimate Tensile Strength [MPa]</b>	870±10	914±10	> 860
<b>Elongation [%]</b>	13.7±1.0	13.1±0.4	> 10

A difference regards the fatigue resistance. The fatigue limit at 50% of resistance probability of the hipped alloy, in fact, is  $441\pm 42$  MPa. Notwithstanding the scattering, the value is comparable with the limit for the wrought and annealed material (cfr. Table 5.3). Evidently, the coarser microstructure has a better resistance to the crack propagation, as for the material produced by SLM (see Paragraph 5.3.1).

The hipped microstructure finds a reference in ISO 20160 standard (A15 microstructure is simply coarser), but it is not one of the recommended. The slight microstructural modification by HIP can be attributed merely to the process temperature, which is in the  $\alpha+\beta$  field. In fact, since deformation introduced by HIP is isostatic and very poor because of the very high density of the as-built material, there is no chance to significantly change the microstructure by this approach. We have here to recall what Semiatin et al. [5] evidenced: a heat treatment in the biphasic field produces some globulization provided that the material has been pre-strained or is dynamically strained, and even in this case the kinetics is quite slow.

Then, verified and studied the behaviour of the as-built material after a treatment in the biphasic field, it becomes interesting to deepen the aspects related to the effect of the strain on the microstructural transformation. This has been investigated on three broken tensile samples. The samples have been chosen from a batch previously fractured in a tensile test. The three samples broke at about the same elongation; by this way, their deformations in the fracture zone should be quite similar. They have been cut in 20 mm long specimens, and each of their external surfaces has been photographed in a stereoscope in order to measure their thickness and calculate, qualitatively, their area reduction at any distance from the fracture surface. The samples have then been heat treated in a DSC furnace, fluxing a mixture of Ar and

---

2% of H<sub>2</sub>, for 1 h at three different temperatures: 900 °C, 980 °C (just below the  $\alpha+\beta/\beta$  transus) and 1020 °C (just above the  $\alpha+\beta/\beta$  transus). The samples have subsequently been etched with Kroll's reagent and observed under an optical microscope.

Close to the fracture surface, the transformed microstructures result to be globular for all the treatment temperatures, as reported in Figure 5.28. Furthermore, the obtained microstructure is very fine after heat treatment at 900 °C, while it is coarser for the specimens heated at higher temperatures.

It is difficult to evaluate the strain amount in the neighborhood of the fracture surface, since the edge is uneven and irregular. Nevertheless, a qualitative starting strain has been calculated, from the acquired images, at about 2.0 mm, 4.0 mm and 6.0 mm from the fracture surface. The calculated strain has afterwards been associated with the transformed microstructure observed after heat treatment. The results of such a qualitative study are summarize in the following figures, where transformed microstructures and relative calculated starting strain are reported for 2 mm (Fig. 5.29), 4 mm (Fig. 5.30) and 6 mm (Fig. 5.31) distances from the fracture surface.

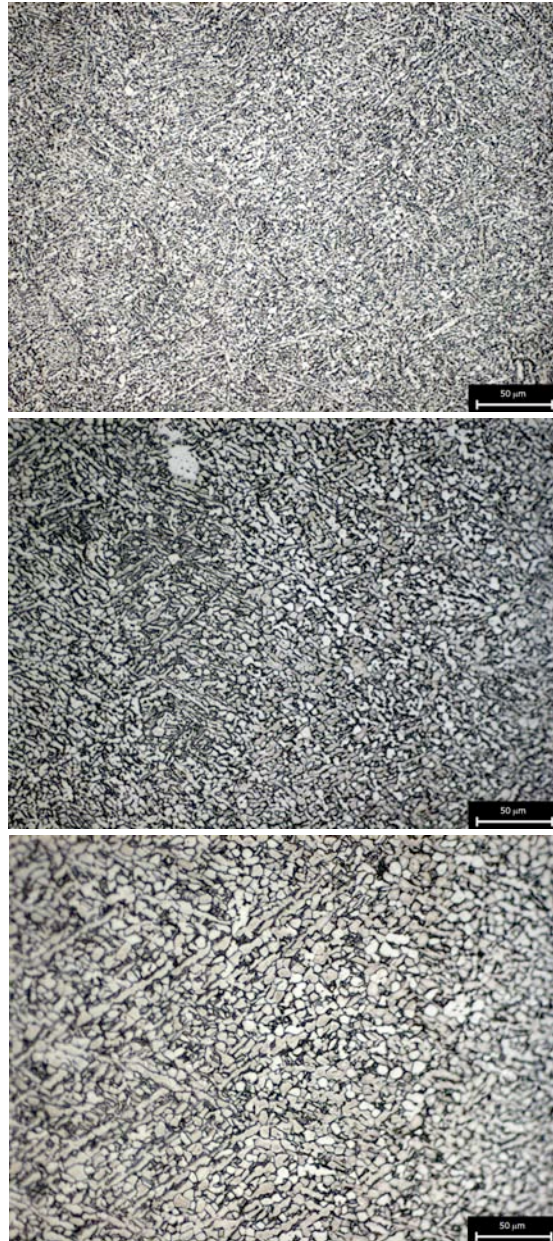


*Figure 5.28. Transformed microstructure of Ti-6Al-4V broken tensile specimens after heat treatment at 900 °C (upper), 980 °C (middle) and 1020 °C (lower); micrographs acquired close to the fracture surface.*

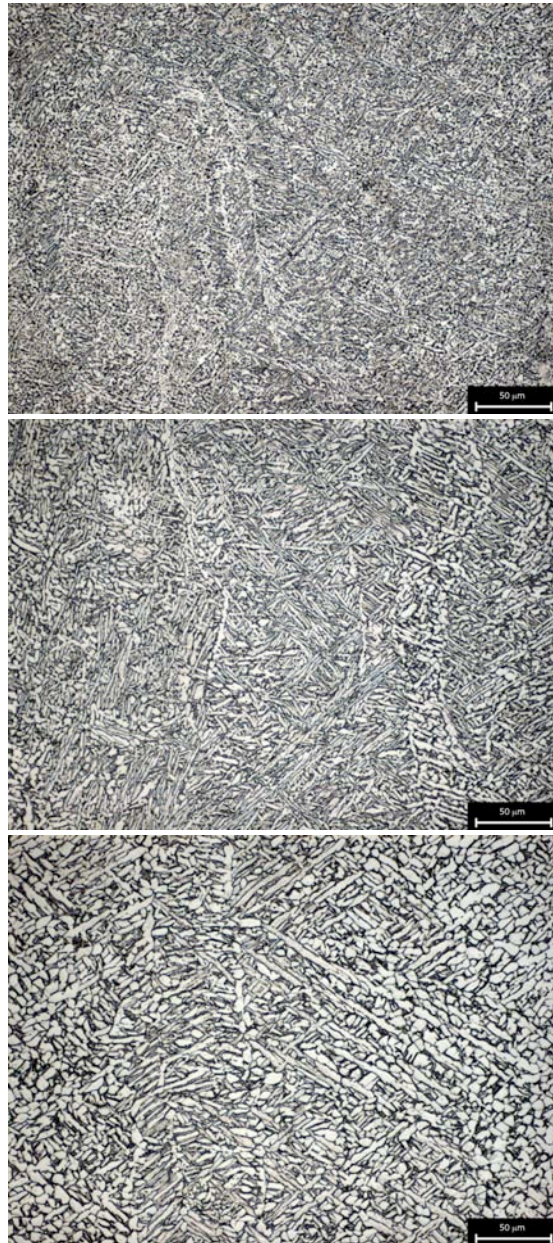


*Figure 5.29. Transformed microstructure of Ti-6Al-4V broken tensile specimens after heat treatment at 900 °C (upper), 980 °C (middle) and 1020 °C (lower); micrographs acquired at a distance of 2 mm from the fracture surface (area reduction: 0.27-0.37).*

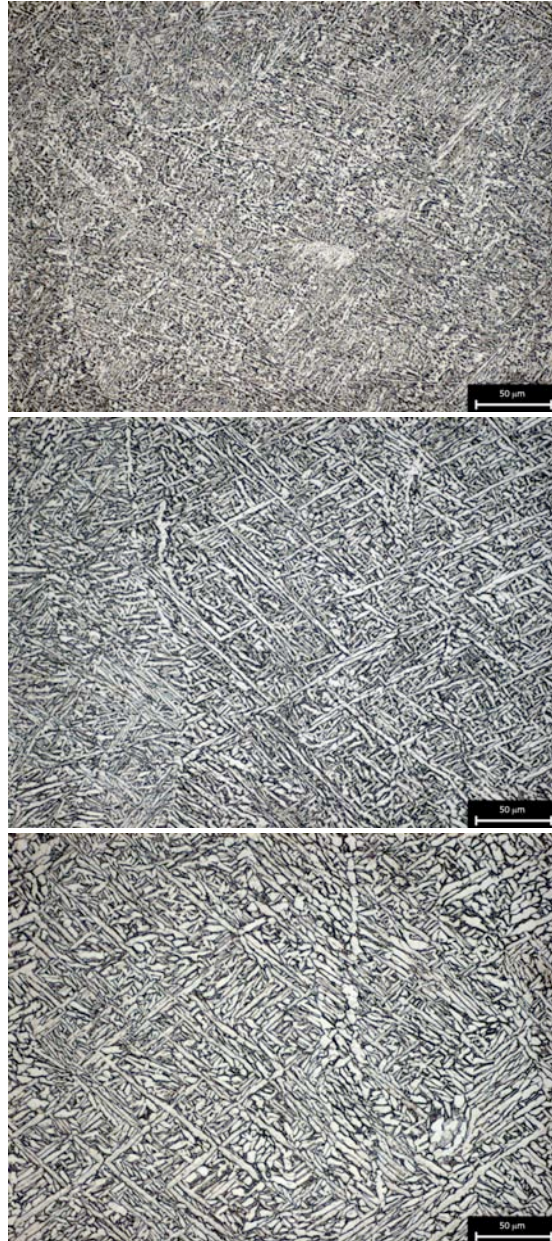


*Figure 5.30. Transformed microstructure of Ti-6Al-4V broken tensile specimens after heat treatment at 900 °C (upper), 980 °C (middle) and 1020 °C (lower); micrographs acquired at a distance of 4 mm from the fracture surface (area reduction: 0.16-0.26).*

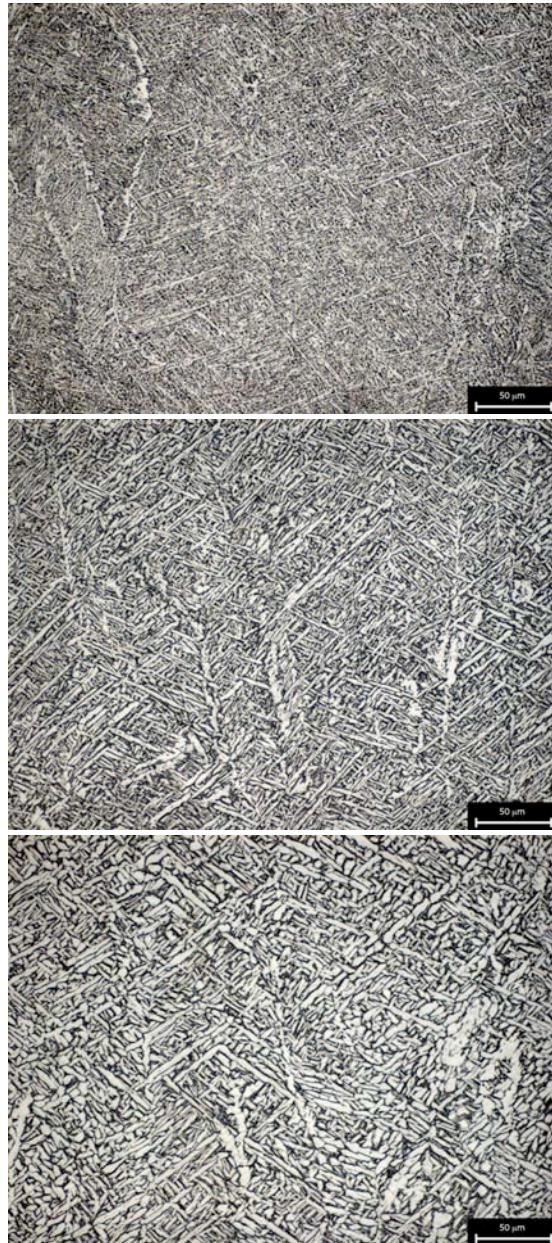


*Figure 5.31. Transformed microstructure of Ti-6Al-4V broken tensile specimens after heat treatment at 900 °C (upper), 980 °C (middle) and 1020 °C (lower); micrographs acquired at a distance of 6 mm from the fracture surface (area reduction: 0.12-0.19).*

As observable in the foregoing figures, for lower temperatures the microstructure cannot become globular in lack of substantial strain. Moreover, at about 2 mm from the fracture surface, where the area reduction is nearly 0.3, a transition zone (from globular to lamellar microstructure) is visible.

When heat treated at 1020 °C, however, the strained material transforms into a globular or quite-globular microstructure even if the strain is not severe (Figs. 5.31, lower). Furthermore, at 6 mm from the fracture surface the microstructure of this sample is comparable with picture A4 of the ISO 20160 standard (Fig. 5.32), which is one of those accepted from the ISO 5832-3 standard and reports a microstructure with long (lamellar)  $\alpha$  grains.

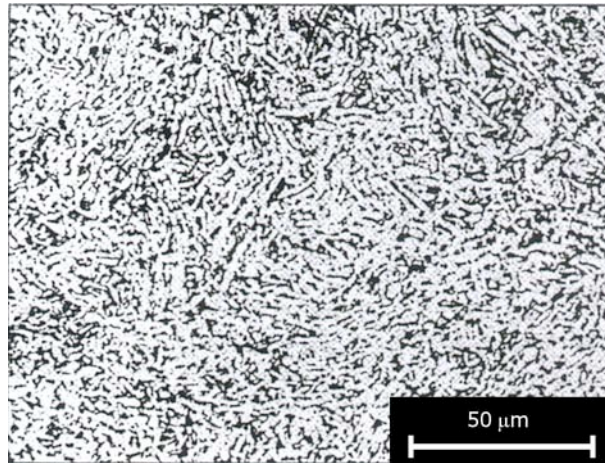


*Figure 5.32. A4 reference micrograph from ISO 20160 standard; globular/lamellar  $\alpha$  in  $\beta$  transformed matrix.*

The study carried out on the broken tensile samples confirms that a certain amount of strain is able to introduce an  $\alpha$ -globular microstructure in the samples. However, the strain must be a shear strain; as shown, in fact, a post-process hipping, which can introduce isostatic strains, results in a coarsening without globularization (Fig. 5.26). Nevertheless, such a strain cannot be introduced in the route of a near-net shape technology such as Electron Beam Melting.

---

## 5.4 Final remarks

Ti-6Al-4V alloy produced by Selective Laser Melting and Electron Beam Melting presents interesting, intrinsic features. In particular, very fine microstructures are associated with appreciable mechanical properties.

Nevertheless, two kinds of problems arise when the materials have to be applied in the biomedical field. Primarily, a ductility lack affected the material produced by SLM. The issue is unavoidably related to the microstructure of the as-built material. This consideration introduces the second kind of problem: the microstructural acceptability. Standards for biomedical applications, in fact, make substantially reference to globular microstructures, typical of wrought and annealed material.

Ductility can be improved via a heat treatment in the biphasic field. The treatment makes the microstructure change, obtaining the precipitation of  $\beta$  phase from the starting martensite. The transformation of the martensite causes a slight reduction of the strength, but on the other hand allows a significant improvement in elongation.

The microstructure of the material is decisive also for the fatigue endurance. In comparison with the wrought and annealed alloy, which commonly has an  $\alpha$ -globular microstructure, Ti-6Al-4V produced by EBM and SLM have a lower fatigue limit, due to the fine microstructure. In fact, the acicular microstructure is better for the resistance to crack nucleation, but is worse for the propagation of the nucleated cracks.

Strictly concerning the microstructures, both the as-built materials do not match the ISO standard requirements because of their morphology. The morphology can be modified by heat treating the alloy; nevertheless, the formation and/or coarsening of a biphasic microstructure cannot hit the target of  $\alpha$  globular microstructure. As a consequence, the point is that there are two peculiar microstructure, which can warrant good mechanical properties, but have to be received by the international standard community.

## References

- [1] *ASM Metals Handbook*, 9th ed., American Society for Metals, Metals Park, Ohio 44073, Vol. 3, 1985
- [2] I. Weiss, F.H. Froes, D. Eylon, G.E. Welsch, *Met. Mater. Trans.* 17A(11) (1986) 1935
- [3] T. Seshacharyulu, S.C. Medeiros, W.G. Frazier, Y.V.R.K. Prasad, *Mat. Sci. Eng.* 325A (2002) 112
- [4] N. Stefansson and S.L. Semiatin, *Metall. Mater. Trans.* 34A (2003) 691
- [5] S.L. Semiatin, N. Stefansson, R.D. Doherty, *Metall. Mater. Trans.* 36A (2005) 1372
- [6] F.X. Gil Mur, D. Rodríguez and J.A. Planell, *J. Alloy Compd.* 234 (1996) 287
- [7] K. Kubiak, J. Sieniawski, *J. Mater. Process. Tech.* 78 (1998) 117
- [8] M.T. Jovanović, S. Tadić, S. Zec, Z. Mišković, I. Bobić, *Mater. Design* 27 (2006) 192
- [9] S. Malinov, W. Sha, Z. Guo, C.C. Tang, A.E. Long, *Mater. Charact.* 48 (2002) 279
- [10] C. Leyens, M. Peters, "Titanium and titanium alloys", Wiley-VHC, 2003
- [11] S. Libardi, "Study of the production by Spark Plasma Sintering of nanostructured Fe-Mo alloys", Ph.D. thesis, Department of Materials Engineering and Industrial Technologies, University of Trento
- [12] G. Lütjering, J.C. Williams, "Titanium", Springer, 2003
- [13] D.G. Lee, Y.H. Lee, C.S. Lee, S. Lee, "Effects of Volume Fraction of Tempered Martensite on Dynamic Deformation Properties of a Ti-6Al-4V Alloy Having a Bimodal Microstructure"
- [14] S.L. Semiatin, V. Seetharaman, A.K. Ghosh, *Phil. Trans. R. Soc. Lond.* 357A (1999) 1487

## Chapter 6

# ASTM F75 alloy produced by Electron Beam Melting

### 6.1 Microstructures

ASTM F75 (CoCrMo) alloy has a microstructure that strongly depends on its phase composition.

First of all, two allotropic phases can be detected: the face centred cubic  $\alpha$  phase, stable at higher temperatures, and the hexagonal close-packed  $\epsilon$  phase, stable at lower temperatures. Because of the sluggish nature of the phase transformation, the cubic phase can be stabilized at room temperature, making the matrix composition to be biphasic.

Characteristic of commercial Co alloys is also the presence of carbides that precipitate on solidification. These, depending on the carbon amount and the processing the material has undergone, vary for quantity, size and distribution. Preferred sites for carbide precipitation are the grain boundaries and the defects, such as twinings and stacking faults. In fact, the Stacking Fault Energy of both the allotropic phases is low: large planar defects between partial dislocation can easily form.

Traditionally, ASTM F75 alloy is processed by casting or by hot working. Processing is usually followed by thermal treating. In particular, the wrought alloy is annealed, while the as-cast material is homogenized, solution treated and aged. After solution treatment and quenching, an fcc carbon-rich matrix is formed. This solid solution is then aged in order to obtain an opportune carbide distribution. The typical microstructure of CoCrMo in the as-cast condition is shown in Figure 6.1: carbides are distributed mainly within the grains (between the dendrites), but also at the grain boundaries. The distribution of the carbides is initially determined by the solidification

features (primarily the pouring temperature of the melt and the cooling rate).



*Figure 6.1. Microstructure of CoCrMo in the as-cast condition; carbides distributed between the dendrites and at the grain boundaries [1].*

Further carbide precipitation, both within the grains and at the grain boundaries, can occur on heating. The microstructure of a cast Stellite 21 alloy after 24 h at 870 °C is shown in Figure 6.2.

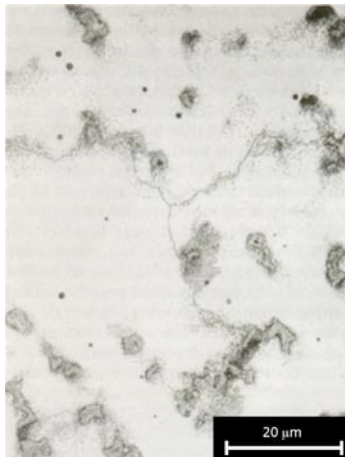


*Figure 6.2. Microstructure of CoCrMo heat treated at 870 °C for 24 h after casting; further carbides precipitated [1].*

---

ASTM F75 is usually processed by casting. Other Co alloys, such as S 816 and HA 25, are usually wrought. After hot working, they are solution treated at a temperature around 1200 °C in order to improve their creep resistance. Since rapid overaging could occur, they generally do not undergo aging. Moreover, full solution of all the carbides is frequently not possible, since melting of the alloy would occur before complete solution of the more stable carbides takes place [1]. Typically, then, they are used in the solution-treated condition: carbides are observable, mainly at the grain boundaries.

Some observations on as-rolled ASTM F75 alloy were made by Weeton and Signorelli [2], as stated in Chapter 2. They noted equiaxed grains containing massive carbides; fine precipitates were also noticed at the grain boundaries. After 72 h at 1230 °C, on the other hand, the solution treated material showed little residual precipitation. Then, an isothermal transformation can take place at 1065 °C, resulting in the formation of a pearlitic lamellar structure along the grain boundaries (Fig. 6.3).

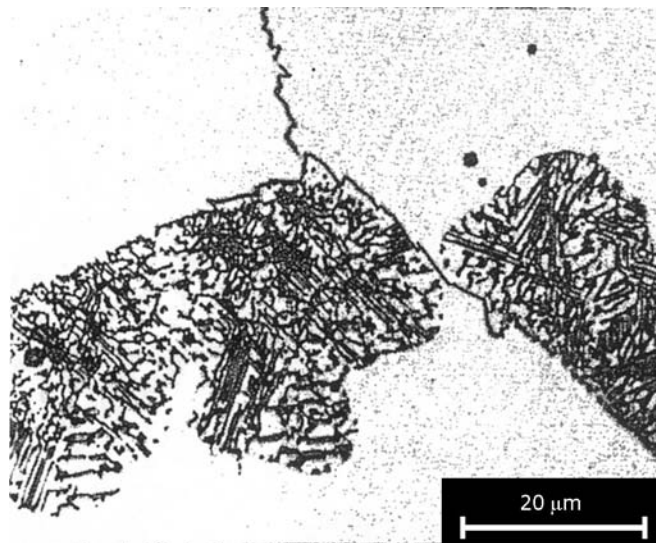


*Figure 6.3. Pearlitic lamellar structure along the grain boundaries of CoCrMo alloy cast solution annealed and isothermally treated at 1065 °C.*

Due to the large undercooling characterizing Electron Beam Melting, the microstructure of the CoCrMo alloy results to be really peculiar (Fig. 6.4).

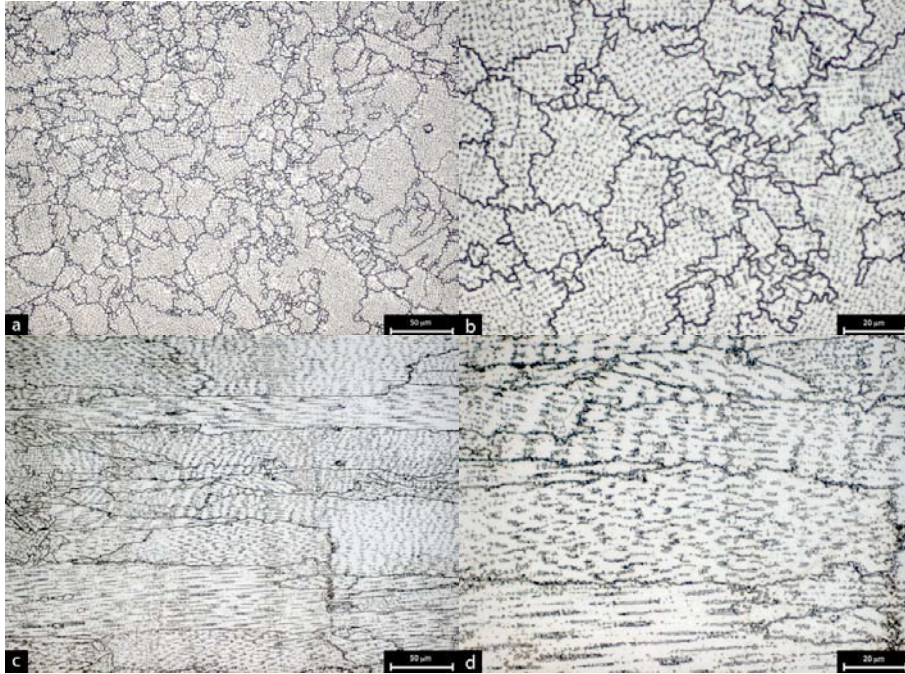


*Figure 6.4. Microstructure of ASTM F75 alloy produced by Electron Beam Melting; (a) and (b) acquired on section transverse to the building direction, (c) and (d) acquired on section parallel to the building direction.*

The microstructure of the as-built alloy is strongly anisotropic. After electrolytic etching, substantially equiaxed grains are observable on a section perpendicular to the building direction. On a section parallel to the building direction, on the contrary, elongated grains are visible. This observation suggests that a columnar grain growth occurred. In particular, it can be hypothesized that an epitaxial mechanism, as described in Paragraph 1.5, took place.

Moreover, the material has a fine, massive distribution of carbides; they appear both at the grain boundaries and within the grains. An SEM observation of the metallographic section after electrolytic etching clarified any doubt about the presence and distribution of carbides.

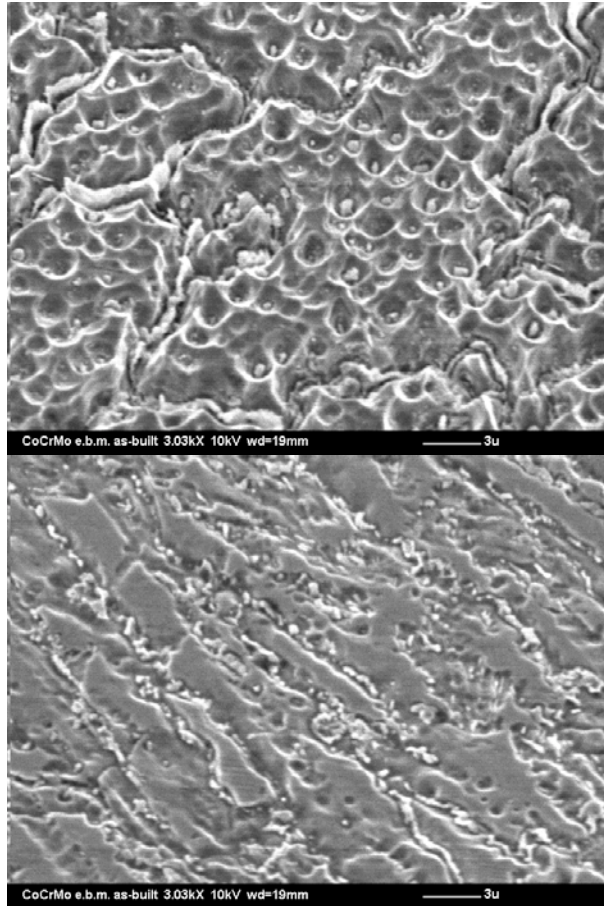


*Figure 6.5. SEM images of ASTM F75 alloy produced by EBM; evidence of carbides.*

Large layers of carbides are in fact observable at the grain boundaries. Carbides are also visible in the intragranular matrix dimples created by etching. XRD analysis confirmed what observed during the microstructural study. Peaks from  $M_{23}C_6$  and  $M_6C$  carbides are in fact observed (Fig. 6.6).

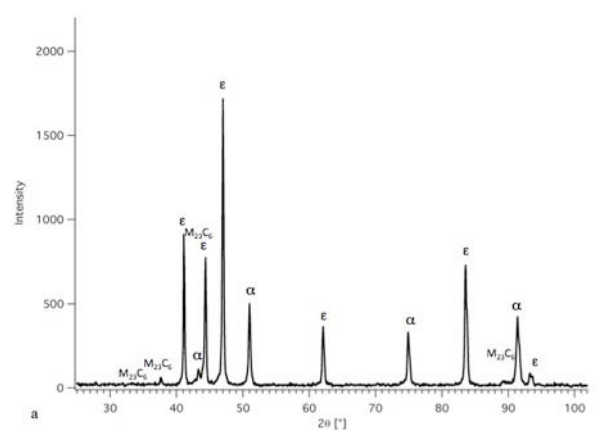


Figure 6.6. XRD pattern acquired on ASTM F75 alloy produced by Electron Beam Melting.

Because of the texture (the vector normal to the basal plane (100) is parallel to the growth direction), a reliable Quantitative Phase Analysis is quite difficult to obtain. However, the as-built material has a biphasic matrix, with prevailing hcp martensite ( $\epsilon$ ).

CoCrMo alloy parts for biomedical applications are traditionally produced by casting. Usually, then, the production is followed by hipping, introduced in order to reduce the porosity. For this alloy, hipping is carried out for 240 min at a temperature of 1200 °C, under a pressure of 1000 bar.

After the post-process hipping, the microstructure strongly changed. The hipped material has equiaxed grains with fewer carbides both at the grain boundaries and within the grains, and pearlitic constituents (Fig. 6.7). The dimension of the equiaxed grains is quite scattered, and large grains are visible, randomly distributed.

From the point of view of the X-Ray Diffraction analysis, the hipped alloy appears to be mainly constituted by fcc phase ( $\alpha$ ). This is not surprising, since usually the solution treated material has an almost completely fcc matrix [2], and hipping was carried out at the same temperature of a solution annealing. Moreover, a small amount of  $M_{23}C_6$  and  $M_6C$  carbides is even detected (Fig. 6.8).

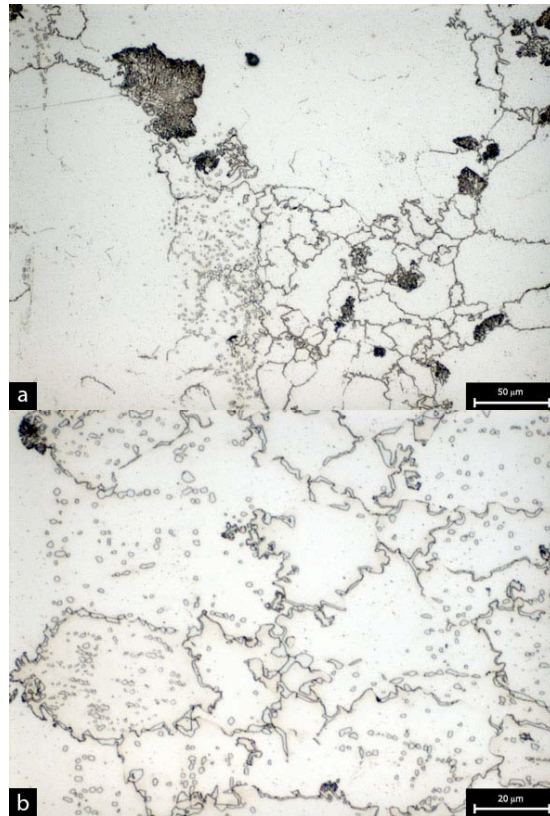


Figure 6.7. Microstructure of ASTM F75 alloy produced by Electron Beam Melting and hipped; (b) at a higher magnification.

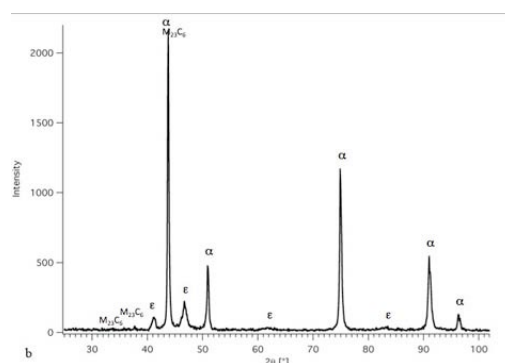


Figure 6.8. XRD pattern acquired on ASTM F75 alloy produced by Electron Beam Melting and hipped.

## 6.2 Mechanical properties of the as-built and hipped materials

As previously introduced, the presence of fcc phase rather than hcp, as well as the amount and distribution of carbides, strongly influence the mechanical properties of the alloy.

It is well-known that fcc structures are associated to 12 principal slip systems (i.e., the octahedral planes) [3]. The large number of equivalent slip systems causes the crystal to slip on more than one octahedral plane contemporarily. As a consequence, the stress required to produce additional deformation rapidly increases, and then a strain hardening takes place. So, metals characterized by an fcc lattice can yield with a relative ease, but after yielding they strain harden. On the other hand, the basal plane of the hcp structure and the octahedral plane of the fcc have the same atomic arrangement. Combined with three slip direction, it warrants 3 principal slip systems. Hcp structure is consequently associated to higher strength and less marked strain hardening behaviour.

Carbides act as precipitation hardening agents. They improve the strength of the material but, at the same time, they embrittle it, acting as sites for the nucleation of cracks, even more since carbides are present at the grain boundaries. Carbides are principally formed from the chromium and the molybdenum. Their morphology and location are important for the strengthening effect. When precipitated at the grain boundaries, in fact, they can prevent sliding and migration of the boundary; if their amount at the grain boundaries is large enough, they can form an interconnected layer that support some of the imposed stress. Within the grains, carbides represent obstacles to the dislocations movement (i.e., crystallographic slip).

Usually, the distribution of carbides is determined by the solidification conditions, which are casting conditions. An additional heat treatment can then cause a further precipitation. Moreover, a solution treatment (at 1175÷1230 °C) followed by rapid cooling can improve the mechanical properties of the alloy. Full solution of the carbides, anyhow, is difficult to obtain, since melting would occur before the more stable carbides are dissolved. As a consequence, the solution treated material still shows carbides, mostly at the grain boundaries. After aging, a fine carbides distribution can be observed also within the grains [1].

---

Depending on the just remarked features, the mechanical properties of the alloy can deeply change, as discussed in the following.

### 6.2.1 Tensile properties

As previously noted in Paragraph 6.1, the distribution of carbides in the as-built material coming from the Electron Beam Melting process is both intergranular and interdendritic. Such a distribution is related to peculiar properties. The material, which has full density, is hard and brittle (Fig. 6.9).

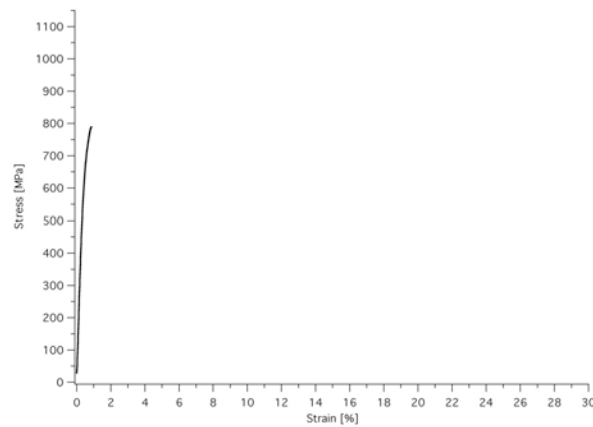


Figure 6.9. Stress-strain curve of ASTM F75 alloy produced by Electron Beam Melting.

The fracture occurred just above the yield point. The UTS of the material, as a matter of fact, is comparable with its yield stress. In comparison with the as-cast material and the standard requirements, the alloy produced by Electron Beam Melting has a higher strength. Nevertheless, no plastic flow is observable.

An SEM analysis of the fracture surfaces of the tensile specimens (Fig. 6.10) furnished information about the fracture mechanism the as-built alloy underwent. A very small ductility (reflected in the substantial absence of dimples) is observable; cracks along the grain boundaries are visible.

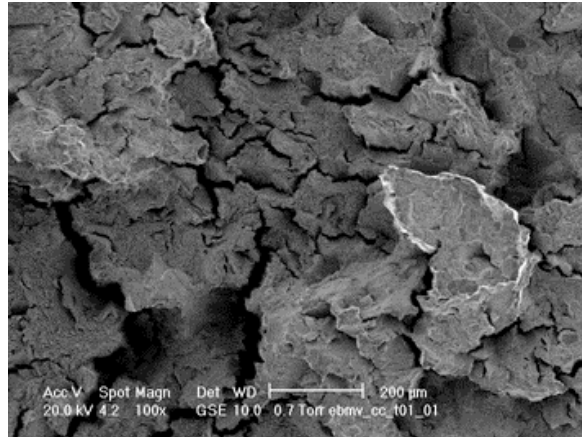


Figure 6.10. Detail of the fracture surface of as-built ASTM F75 alloy; very small ductility (reflected in the substantial absence of dimples) and cracks along the grain boundaries are observable.

As previously said, a hipping treatment can follow the process. It is usually put into practice with the aim of reducing the residual porosity. The material produced by EBM has not residual porosity; however, the treatment at 1200 °C for 4 h could supply enough energy to promote an evolution of the microstructure, dissolving the excess of intragranular carbides. The tensile stress-strain curve associated to the microstructure previously shown in Figure 6.7 is reported in the following graph.

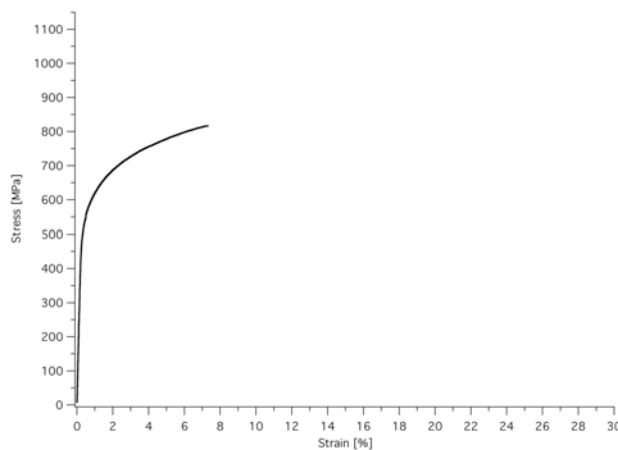


Figure 6.11. Stress-strain curve of ASTM F75 alloy produced by Electron Beam Melting and hipped.

*Table 6.1. Tensile properties of ASTM F75 alloy produced by Electron Beam Melting (EBM); standard requirements reported.*

	as-built	hipped	ISO 5832-4
<b>Elastic Modulus [GPa]</b>	165±6	190±7	-
<b>Yield stress [MPa]</b>	719±17	545±5	> 450
<b>Ultimate Tensile Strength [MPa]</b>	796±12	812±17	> 665
<b>Elongation [%]</b>	1.0±0.2	7.0±1.1	> 8

It is evident from Table 6.1 that, against a reduction of yield stress, both Ultimate Tensile Strength and elongation to fracture underwent an improvement. However, the improvement is not enough to match the standard requirements, which impose an elongation to fracture higher than 8%.

Having a look at the fracture surface of the hipped tensile specimens (Fig. 6.12), an intergranular fracture morphology can be observed. Some ductility is now detectable because of the presence of small dimples on the grain boundaries made clear by the fracture.



*Figure 6.12. Detail of the fracture surface of ASTM F75 alloy produced by EBM and hipped; small dimples on the grain boundaries detectable.*

Nevertheless, even if the deformation mechanism has changed, ductility is still poor.

The as-built material has also an appreciable difference in Elastic Modulus in comparison with the hipped material. Concerning this, the Elastic Modulus of single crystals of pure cobalt with hexagonal lattice can noticeably vary (40-50 GPa) depending on the orientation the crystals have compared with the solicitation direction. In a polycrystalline material, Elastic Modulus assumes an intermediate value; however, in presence of a pronounced texture, the material can exhibit an anisotropic behaviour.

In the material produced by Electron Beam Melting, a strong texture is present. In particular, anisotropic elongated grains are oriented in the same direction of the tensile solicitation. The microstructure after hipping, on the other hand, has dimensionally-scattered equiaxed grains. The difference in Elastic Modulus between the two materials can then be explained in terms of orientations: the as-built material suffers the oriented shape of its grains.

### 6.2.2 Fatigue properties

As well as for Ti-6Al-4V, an investigation of the fatigue limit at 50% of fracture probability has been carried out for ASTM F75 alloy, both in as-built and hipped conditions.

The obtained results match the previous observations about tensile properties. In fact, starting from the general consideration that the fatigue limit usually falls in the range between  $0.3 \sigma_y$  and  $0.5 \sigma_y$ , it could be expected that it would be 210-360 MPa for the as-built material and 160-270 MPa for the hipped material. As observable in Table 6.2, the limit at 50% of resistance probability is positioned in the theoretical range for both the material.

Table 6.2. Fatigue limits at 10%, 50% and 90% of resistance probability for ASTM F75 alloy produced by EBM, in both as-built and hipped conditions.

	Limit at 10% of resistance probability	Limit at 50% of resistance probability	Limit at 90% of resistance probability
<b>As-built material</b>	344	308±25	271
<b>Hipped material</b>	270	241±14	213

Because of the high strain hardenability of the alloy, the Ultimate Tensile Strengths of the two materials are comparable. In fact, even if the yield stresses are dissimilar, the improvement in ductility associated with the hipping makes the UTS of the hipped alloy to reach the UTS of the as-built material. Nevertheless, the yield stress rather than ductility and UTS seems to be the dominant indicator of the fatigue behaviour of the material.

The fatigue endurance is rather related to the different amounts of distinct phases: hcp, fcc and carbides [4]. In particular, the presence of cubic phase can affect fatigue resistance. In fact, thanks to the low Stacking Fault Energy of the alloy, a strain-induced martensitic transformation from fcc to hcp phase can occur, also under cyclic stress. The transformation introduces additional faceted fracture planes (the basal  $\{0001\}_{\text{hcp}}$ ) [5]. On the other hand, carbides can also play a negative role on the fatigue behaviour of the material. They can affect the fatigue resistance, especially when present at grain boundaries [6]. So, the evidence of large pearlitic constituent at grain boundaries in the hipped material can be related to poor fatigue endurance. Moreover, Zhuang and Langer [7] reported that the fatigue fractures of cast CoCrMo alloys show a substantial amount of stage I fatigue which takes the form of a cleavage-like fracture surface, with a crystallographically oriented structure. Furthermore, they evidenced that those crystallographic fractures occurred along  $\{111\}_{\text{fcc}}$  planes. Authors ascribed the occurring of the slip most often on  $\{111\}$  octahedral planes to the presence of dissociated dislocations, stacking faults and twins, and to the intersections of these defects. Then, the low Stacking Fault Energy of the material can strongly affect its fatigue endurance. However, significant fatigue resistances are reported for CoCrMo alloys [6]. So, a proper control of the material microstructure allows good fatigue properties to be obtained.

## **6.3 Modification on heating of the as-built microstructure and related mechanical properties**

As other cobalt alloys, ASTM F75 is sensitive to heat treating. After a solution treatment, in fact, a homogeneous solid solution of carbon in an fcc matrix can be obtained. As a consequence, the material loses strength, but improves in ductility. The proper combination of the solution treatment with an aging, moreover, can make the alloy strengthened by precipitation hardening, paying, however, a reduction in ductility.

Furthermore, whether or not intergranular and intragranular carbides are present, this influences the tribological behaviour of the alloy, and its ability to be polished (important for biomedical applications).

In order to control the microstructure of the material and obtain the desired mechanical properties, a study of the material behaviour on heating is necessary.

### **6.3.1 Phase transformations on heating and solution treatment on the as-built material**

As stated above, a common way to improve the ductility of an ASTM F75 alloy is applying a solution treatment. Commonly, the treatment is carried out at a temperature above 1200 °C for times varying from one to several hours. The temperature interval for solution treating can vary depending on the chemical composition of the alloy. As a first consequence, the solution treatment allows the partial dissolution of the carbides (i.e., the intragranular carbides) to take place. Furthermore, it can stabilize the cubic phase. From the point of view of the mechanical properties, this generally results in an improvement in ductility coupled with a reduction in yield stress.

Several authors [8,9] take into account a homogenization treatment preceding the solution annealing and the aging of the alloy. The treatment is usually carried out around 1100 °C and, as well as for homogenizing, it works for stress relieving and for carbide precipitation. The homogenization treatment is also associated to grain growth [10]. However, such a treatment is traditionally applied to the as-cast alloy. In the

material produced by Electron Beam Melting, neither segregation nor residual stress is critical, and a widespread carbide precipitation takes place already during the process. So, homogenization is not considered necessary for the EBM as-built material, if not with the aim of changing the microstructure.

A dilatometric study of the material behaviour on heating was carried out in order to individuate the temperatures associated to phase transformations. The alloy was heated up above 1300 °C, and the dilatometric differential rate was studied.

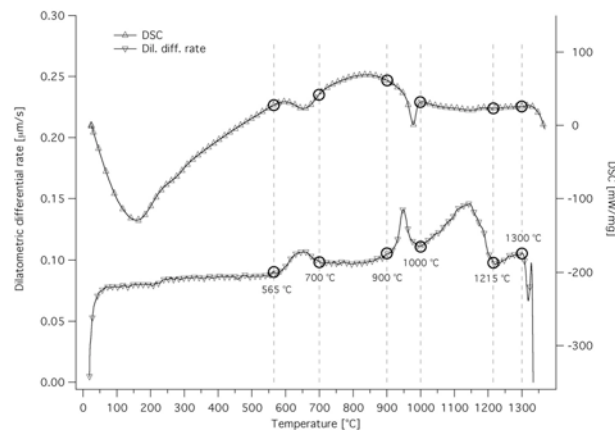


Figure 6.13. Dilatometric differential rate and Differential Scanning Calorimetry (DSC) signals acquired on ASTM F75 alloy produced by EBM.

Associated to the dilatometric study, a DSC scanning was carried out in the same temperature range. As shown in Figure 6.13, the individuated temperature intervals are the same for both the analyses. In particular, three peaks were individuated, each corresponding to a phenomenon occurring on heating.

In order to determine the correlation between the observed peaks and the transformations taking place into the material, a preliminary systematic study has been carried out. The study consisted in carrying out, in the dilatometer, heating at the individuated temperatures (i.e., the temperatures limiting the peaks) and then quenching at high cooling rate in order to investigate the microstructural composition at different temperatures. The quenched samples were investigated through XRD analysis and microstructural observation after electrolytic etching. As previously stated, a Quantitative Phase Analysis on the alloy processed by EBM is difficult,

because a strong texture conditions the analysis. Since this study had the aim of understand which phenomenon occurs in a single temperature range, the author resolved to analyze the same section (i.e., the section perpendicular to the layering direction) and compare qualitatively the results.

Heating at 565 °C, 900 °C, 1000 °C and 1215 °C was immediately followed by quenching at 100 °C/s.

The microstructures obtained after heating and quenching are reported in Figs. 6.14 and 6.15, while the phase compositions are summarized in Table 6.3.



Figure 6.14. Microstructures of ASTM F75 alloy produced by EBM and heat treated at (a) 565 °C, (b) 900 °C, (c) 1000 °C and (d) 1215 °C.

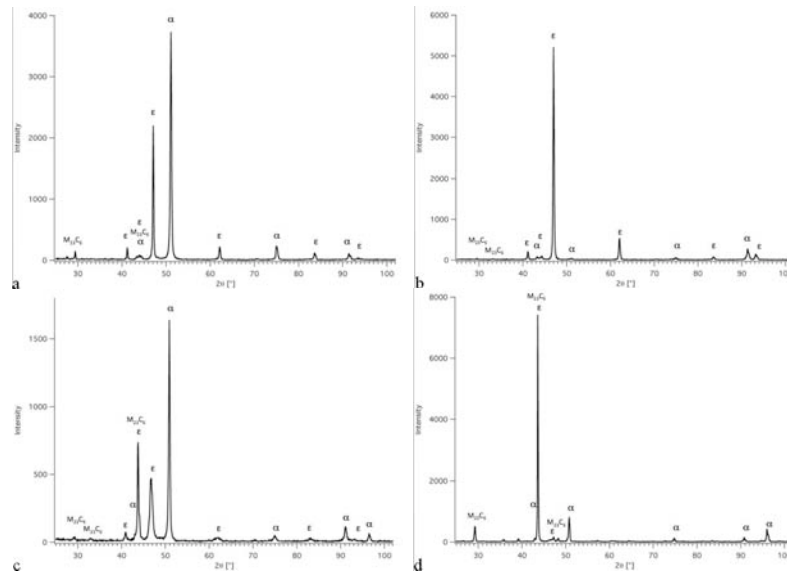
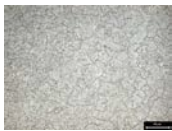
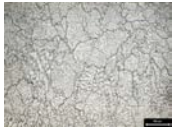


Figure 6.15. XRD patterns acquired on ASTM F75 alloy produced by EBM and heat treated at (a) 565 °C, (b) 900 °C, (c) 1000 °C and (d) 1215 °C.

Table 6.3. Correspondence between temperature ranges and phase compositions.

Temp. range	Phenomenon	Phase composition	Microstructure	
565-900 °C	$\alpha$ to $\epsilon$ transformation	- hcp ( $\epsilon$ ) phase - disappearance of fcc ( $\alpha$ ) phase	- anisotropic dendritic - intergranular + interdendritic carbides	
900-1000 °C	$\epsilon$ to $\alpha$ transformation	- reappearance of fcc ( $\alpha$ ) phase - strong reduction of hcp ( $\epsilon$ ) phase	- anisotropic dendritic - intergranular + interdendritic carbides	
1000-1215 °C	solution annealing	- increase in hcp ( $\epsilon$ ) phase	- equiaxed - solutioning of interdendritic carbides	

As shown in Figure 6.14, during heat treating between 565 °C and 1000 °C the microstructure does not significantly change: intergranular and interdendritic carbides

are still present after quenching from 1000 °C (Fig. 6.14c). The XRD analysis, anyhow, evidenced the substantial disappearance of the cubic phase between 565 °C and 900 °C; therefore, the first peak in the dilatometric signal (Fig. 6.13) is associated to the  $\alpha$  to  $\epsilon$  transformation. The second peak (between 900 °C and 1000 °C) is on the contrary related to the  $\epsilon$  to  $\alpha$  transformation, because the XRD analysis showed the reappearance of the fcc phase (Fig. 6.15) against no visible modification of the microstructure. Between 1000 °C and 1215 °C, the microstructure undergoes a deep transformation: the interdendritic carbides are solubilized, as well as most of the intergranular carbides. The etched section, in confirmation of this, shows a matrix free of carbides, in which no significant grain growth has occurred. The XRD analysis, however, pointed out the presence of  $M_{23}C_6$  carbides remaining at the grain boundaries. An increase in the hexagonal phase is also noticed. Actually, the reversion of the cubic to the hexagonal structure was reported for pure cobalt at temperatures in the region of the magnetic transformation (1100-1150 °C) and was attributed to the presence of interstitial impurities [1].

The first consequence of this study is the individuation of the proper solution treating temperature. In fact, if the peak associated to the decomposition of the carbides runs out below 1215 °C, the solution treatment can be effectually carried out just above this temperature.

Then, a temperature of 1220 °C was chosen. Since the microstructure undergoes a transformation even in absence of an isothermal step, as pointed out by the treatment in the dilatometer, a short time (15 min) was chosen for the solution treatment.

After a solution treatment in furnace at 1220 °C for 15 min, the tensile properties of the material changed. Against a considerable improvement in ductility, the yield stress underwent an evident reduction, as shown in Figure 6.16 and Table 6.4.

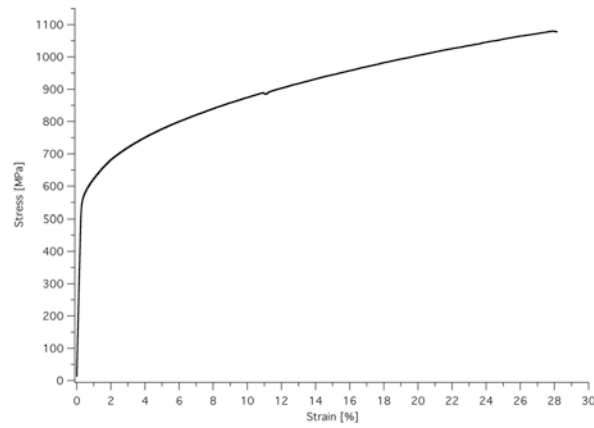


Figure 6.16. Stress-strain curve of ASTM F75 alloy produced by Electron Beam Melting and solution annealed.

Table 6.4. Tensile properties of ASTM F75 alloy produced by Electron Beam Melting (EBM) and solution annealed; as-built material's properties and standard requirements reported.

	<b>solution treated</b>	<b>as-built</b>	<b>ISO 5832-4</b>
<b>Elastic Modulus [GPa]</b>	206±1	165±6	-
<b>Yield stress [MPa]</b>	579±6	719±17	> 450
<b>Ultimate Tensile Strength [MPa]</b>	1073±25	796±12	> 665
<b>Elongation [%]</b>	27.3±1.6	1.0±0.2	> 8

From the point of view of the fracture surface, the solution treated alloy exhibits an intergranular fracture morphology: grain boundaries are observable on the fracture surface (Fig. 6.17, upper). Moreover, semi-cleavages are visible on the fracture surface (Fig. 6.17, lower).

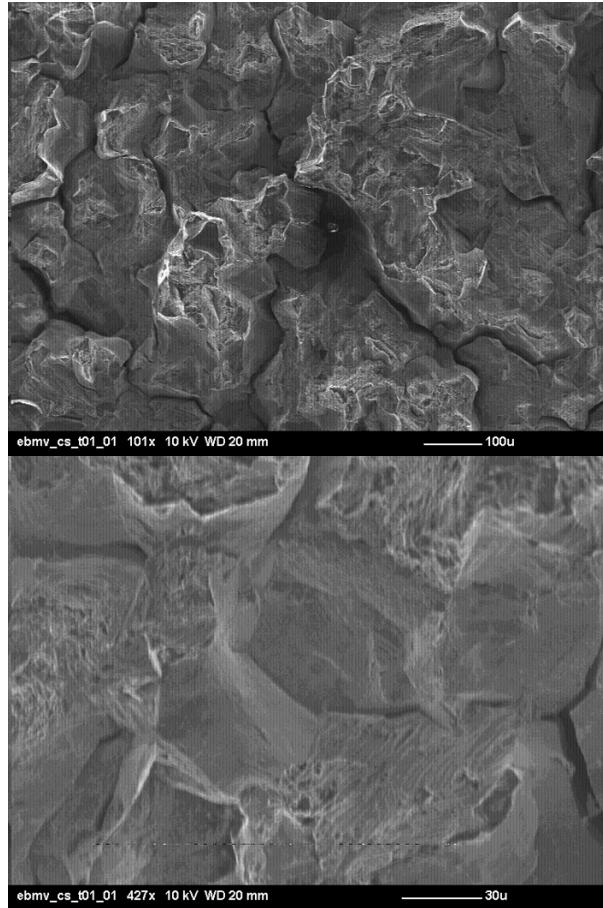


Figure 6.17. Fracture surface of ASTM F75 alloy produced by EBM and solution annealed; intergranular fracture morphology.

The yield stress of the solution treated material is noticeably lower than the yield stress of the as-built material, and comparable with the  $\sigma_y$  of the hipped material. Nevertheless, its Ultimate Tensile Strength is higher than those of both as-built and hipped material. This is related to the strain hardening rate of the material. In fact, the high strain hardening rate characterizing the ASTM F75 alloy makes high UTS corresponding to high elongation.

Solution annealed CoCrMo alloy is characterized by a low Stacking Fault Energy and is mainly constituted by fcc phase with low stacking fault density. A small amount of

heavily faulted hcp ( $\epsilon$ ) phase is also present. The low SFE makes the plastic deformation to occur by gliding of partial dislocations, twinning and strain-induced martensitic transformation. The slip mechanism in the fcc phase is inhibited by the stacking faults and by the formation of hcp bands; stacking faults are also responsible for the increase in strength of the hcp phase. So, the strain hardenability of the alloy is high. Due to these concurring features, moreover, the curvature of the plastic field in a logarithmic stress-strain diagram has an upward trend (Fig. 6.18).

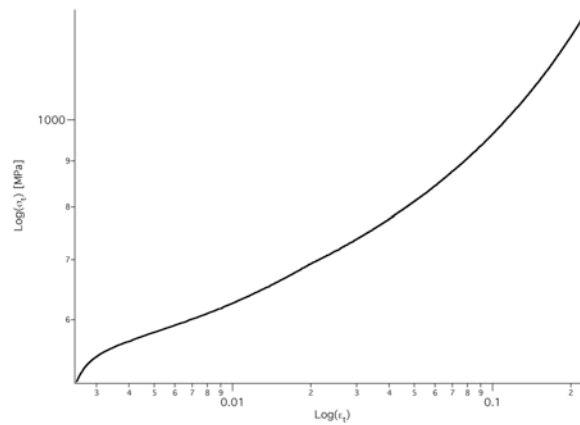


Figure 6.18. Logarithmic stress-strain diagram of the plastic flow of ASTM F75 alloy produced by EBM and solution annealed.

Ludwigson and Berger [11] suggested a model for the plastic behaviour of metastable austenitic stainless steels.

They started from considerations upon the empirical equation

$$\sigma_t = K [\ln(1 + \epsilon)]^n$$

where  $\sigma_t$  is the true stress,  $\epsilon$  is the strain,  $K$  is a constant termed the strength factor and  $n$  is a constant termed the strain-hardening factor. The equation is satisfied for many materials from the onset of the plastic flow to the onset of necking; however, exceptions were noted, suggesting a strain-induced decomposition of austenite to martensite to be responsible for the observed exceptional behaviour [12]. When a strain-induced transformation is present, it takes part in the hardening behaviour of

the material, as well as strength of both austenite (before transformation) and martensite (after transformation).

The contribution that austenite strain hardening makes to the flow curve may be described by

$$\sigma_A = K[\ln(1 + \epsilon)]^n [VFA]$$

where  $[VFA]$  is the volume fraction of austenite present in the steel at the punctual level of strain.  $K$  becomes the austenite strength factor, while  $n$  becomes the austenite strain-hardening index.

The volume fraction of martensite ( $[VFM]$ ) is a continuous function of strain. The nature of martensite formation is autocatalytic, since the formation itself produces dilational and coherency strains in the structure. Furthermore, the transformation reduces the volume fraction of available austenite. Then, Ludwigson and Berger suggested for the volume fraction of martensite the equation

$$[VFM] = A\epsilon^B [VFA]$$

where  $B$  is an exponent to account for autocatalysis and  $A$  is a proportionality constant.

As a consequence, considering that their sum is unity, the volume fractions of the two phases can be described as

$$\begin{aligned} [VFM] &= \left(1 + \frac{\epsilon^{-B}}{A}\right)^{-1} \\ [VFA] &= 1 - \left(1 + \frac{\epsilon^{-B}}{A}\right)^{-1} \end{aligned}$$

and then the austenite contribution to the flow step becomes

$$\sigma_A = K[\ln(1 + \epsilon)]^n \left[1 - \left(1 + \frac{\epsilon^{-B}}{A}\right)^{-1}\right] = K\epsilon_t^n \left[1 - \left(1 + \frac{\epsilon^{-B}}{A}\right)^{-1}\right]$$

It is worthy to note that in this last equation  $A$  represents the ease with which strain-induced transformation can occur and  $B$  represents the effect of martensite

---

formation in stimulating a further formation.

On the other hand, the contribution of the martensitic phase on the flow behaviour can be described by the following equation,

$$\sigma_M = C(1 + \frac{e^{-B}}{A})^{-Q}$$

where  $C$  is the flow stress of the material extrapolated to a fully martensitic structure and  $Q$  is a measure of how effectively increasing amounts of martensite are translated into an increased stress contribution (martensitic strengthening index).

The equation describing the flow stress is then, after Ludwigson and Berger, the sum of the two contributions:

$$\sigma_t = \sigma_A + \sigma_M = K\epsilon_t^n [1 - (1 + \frac{\epsilon^{-B}}{A})^{-1}] + C(1 + \frac{\epsilon^{-B}}{A})^{-Q}$$

Afterwards, Ludwigson [13] suggested a further model specific for the flow curves of fcc alloys:

$$\sigma_t = K_1\epsilon_t^{n_1} + \exp(K_2 + n_2\epsilon_t)$$

where  $K_1$ ,  $K_2$ ,  $n_1$  and  $n_2$  are constants and the exponential term expresses the difference between the classical equation for the flow step and the proposed model. The logarithm of this equation is a linear function of true strain.

However, this model is quite complicated to be applied. Alternative, simplified models had then been developed, in order to account for an easier application.

Tian and Zhang [14] developed a mathematical description for flow curves of some stable austenitic steels, i.e. steels in which austenite does not transform into martensite during deformation. In other words, no transformation strengthening occurs. Using the Gauss-Newton method, Tian and Zhang obtained a general equation for the description of the flow curves:

$$\sigma_t = K\epsilon_t^{n_1 + n_2 \ln \epsilon_t}$$

in which  $K$  is the strength factor and  $n_1$  and  $n_2$  are constants related to the strain hardening rate.

Anyhow, the necessity to model the behaviour of a material undergoing a strain-induced martensitic transformation is actual for many alloys. Concerning this, Kim and Lim [15] suggested a model able to give account of the contribution of the martensitic transformation during deformation in a simpler way in comparison with the Ludwigson and Berger approach. They supposed a quadratic relationship between  $\ln \sigma_t$  and  $\ln \epsilon_t$ . Then, they assumed a linear relationship between strain hardening exponent and true stress:

$$n = \frac{d \ln \sigma_t}{d \ln \epsilon_t} = M \epsilon_t + N$$

where  $M$  and  $N$  are temperature dependent constants. The equation can be rewritten as

$$d \ln \sigma_t \frac{\epsilon_t}{d \epsilon_t} = M \epsilon_t + N$$

and then, upon integrating,

$$\sigma_t = K \epsilon_t^N \exp(M \epsilon_t)$$

where  $K$  is a material constant. This is the Kim's and Lim's flow equation, in which the constant  $M$  is related to the degree of the strain-induced transformation. Kim and Lim also furnished an indication about a necking criterion for the cases in which the strain-induced martensite forms. Considering that necking starts at the maximum engineering stress, they suggested the amount of true uniform elongation to be

$$\epsilon_u = \frac{N}{1 - M}$$

The models described above had been developed from the study of different steels. Nevertheless, they can be successfully applied to even other materials in which a strain-induced phase transformation may occur.

The flow step characteristic of the ASTM F75 alloy produced by Electron Beam Melting and solution annealed is observable in Figure 6.19, where the log-log curve and its fitting are represented.

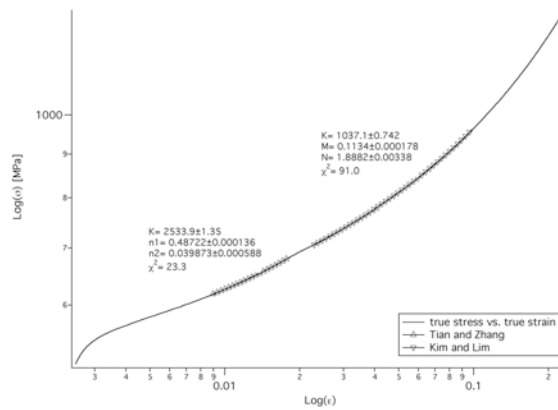


Figure 6.19. Logarithmic stress-strain diagram of the plastic flow of ASTM F75 alloy produced by EBM and solution annealed: fitting.

From about 1% to about 2% of elongation, the flow curve can be fitted by the Tian and Zhang model; this signifies that in the first part of the plastic step no strain-induced martensitic transformation occurs. Up above 2% of elongation, the transformation starts. In fact, the plastic behaviour of the material in this range is well fitted by the Kim and Lim model. The Kim and Lim fitting is good only up to 10% of elongation. Above this value, the faulting of the phases, and in particular the faulting of the martensite, dominates on the strain hardening concurring factors.

As stated above, after Kim and Lim the strain hardening rate can be plotted as a function of the true strain. The application of this idea at the EBM material results in the graph of Figure 6.20.

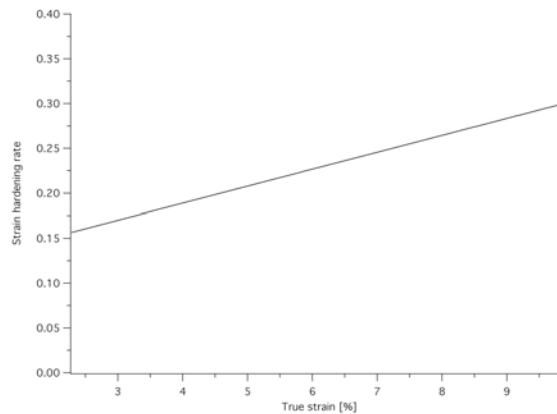


Figure 6.20. Strain hardening rate as a function of the true strain after Kim and Lim.

Furthermore, the true uniform elongation can be calculated from the equation involving  $\epsilon_u$ ,  $M$  and  $N$ ; it results to be about 213% (which is not reasonably acceptable). The very high value of  $N$ , in fact, makes the ratio between  $N$  itself and  $(1 - M)$  very large. Effectively, because of the low SFE, no striking of plastic instability can be observed in CoCrMo alloys.

### 6.3.2 Partial solution treatment on the as-built material

Looking at the question from the point of view of the standard requirements, the elongation to fracture of the solution treated material matches the ISO 5832-4 standard specifications. This can be considered satisfactory. Nevertheless, abstracting from the standard prescriptions, the tensile properties of the solution annealed alloy are suited for mechanical components rather than biomedical parts. Against a remarkable resistance to overloading (due to its very high strain hardenability), in fact, the solution treated material has small yield stress in comparison with the as-built material. Furthermore, considering the observations reported in Paragraph 6.2.2, this is detrimental also for the fatigue resistance; effectively, the fatigue limit at 50% of failure probability calculated on the solution annealed alloy resulted to be  $249 \pm 16$  MPa. The yield stress, then, is important as well as the ductility for the obtaining of a proper material for the biomedical application. Starting from these considerations, a good compromise between the two properties must be looked for.

---

Dobbs and Robertson [6] studied different heat treatments of cast CoCrMo alloy for orthopaedic implant use. They thought about the possibility of an improvement in ductility obtained by heat treating the as-cast material. So, they carried out solution treatments at 1240 °C and aging at 720 °C for different times. Longer the solution treatment time, higher the elongation, but lower the strength of the alloy. Aging, on the contrary, operates in the opposite direction, improving strength and hardness to elongation's detriment. Dobbs and Robertson noted that the best results in terms of corrosion fatigue were guaranteed by a partial solution treatment. The partial treatment did not alter the carbide size and morphology, but both the precipitates at the grain boundaries and the cored microstructure. The explanation Dobbs and Robertson gave of the change in tensile properties was related to the microstructural modifications during heat treating. In the as-cast state, in fact, the main part of the strengthening is due to the carbides, whilst solid solution mechanism is of less importance. Moreover, the carbides at the grain boundaries and the coring were responsible for the brittleness of the as-cast material. Concerning this, the carbide dissolution and the coring elimination caused by the solution treatment make the alloy less strong but more ductile. The partial solution treatment warrants a good compromise between the two extreme conditions.

Well-known Dobbs' and Robertson's considerations represent a starting point for the study carried out on CoCrMo alloy produced by Electron Beam Melting. From the dilatometric study commented above, it can be inferred that the solutioning takes place between 1000 °C and 1215 °C. Consequently, the widening of the response of the material to the solution treatment has to be conducted inside this temperature range. A second dilatometric study had then been carried out. This study consisted in the heating up to different temperatures (in the solutioning range) and in the quenching from those temperatures. Between heating and cooling, the material underwent an isothermal step for the solution time of 15 min. The aim of the quenching was the 'freezing' of the microstructural features characterizing the single treatment temperature. Then, it was chosen a cooling rate that was high enough to avoid microstructural changes. At the same time, it suitably approached the technological cooling rates applicable in the high vacuum furnace employed for the industrial heat treatments. This cooling rate was 15 °C/s.

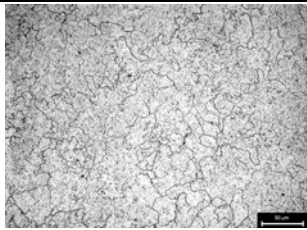
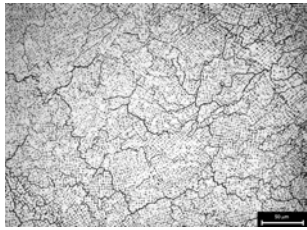
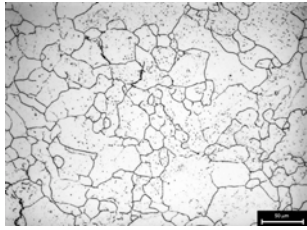
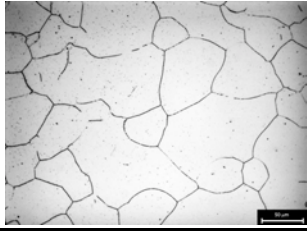
The microstructural evolution of the material within the solutioning stage is summarized in Figure 6.21.



Figure 6.21. Microstructures of ASTM F75 alloy produced by Electron Beam Melting and heat treated at (a) 1050°C, 1100 °C (b), (c) 1150 °C and (d) 1180 °C for 15 min (in dilatometer).

Up to 1100 °C, no change in the microstructure is evidenced in comparison with the as-built material. The observable solutioning of the intragranular carbides in the EBM material happens between 1100 °C and 1150 °C. Moreover, the material solution treated at 1180 °C underwent a dramatic grain growth, even if not the whole of the grain boundaries had been pointed out by the etching (the curvature of the evidenced grain boundaries is meaningful in this way). Following the ASTM E112-96 standard suggestions, the average grain size had been calculated on several micrographs for each sample. The resulting average sizes are summarized in Table 6.5. Furthermore, above 1100 °C the solution treatment is responsible for making the anisotropic microstructure to become equiaxed. From the point of view of the phase composition, above 1100 °C the material lattice is mainly austenitic (Tab. 6.5).

Table 6.5. Microhardness, average grain size, fcc percentage and microstructures of ASTM F75 alloy produced by Electron Beam Melting and heat treated in dilatometer at different temperatures.

Treatment temperature [°C]	$\mu\text{HV}$ [ $\text{HV}_{0.05}$ ]	Average grain size [ $\mu\text{m}$ ]	fcc %	Microstructure
1050	447±14	10.7	83.2±1.7	
1100	426±12	15.0	89.9±1.8	
1150	404±20	63.5	93.8±1.9	
1180	396±14	71.2	95.2±1.9	

Concerning these microstructural observations, it is likewise interesting to analyze the trend of the microhardness versus the treatment temperature (Fig. 6.22).

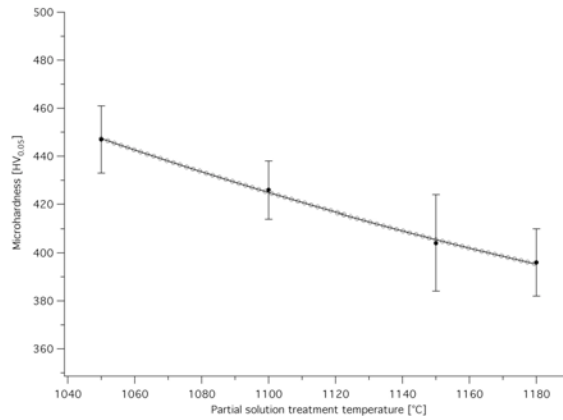


Figure 6.22. Microhardness vs. treatment temperature for ASTM F75 alloy produced by EBM.

Because of the combined effect of carbide solutioning, phase composition and grain growth, the microhardness has a decreasing trend with treatment temperature. However, the decrease in microhardness is not critical.

Since the main evolution of the material happens between 1100 °C and 1150 °C, it is interesting to focus the study on this temperature range. A partial solution treatment had then been carried out at 1125 °C. The obtained microstructure is reported in Figure 6.23.

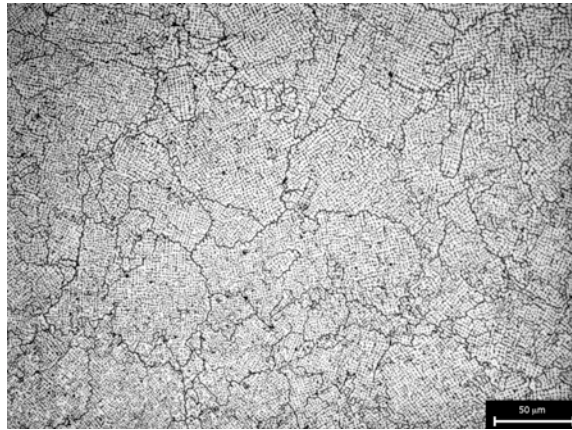
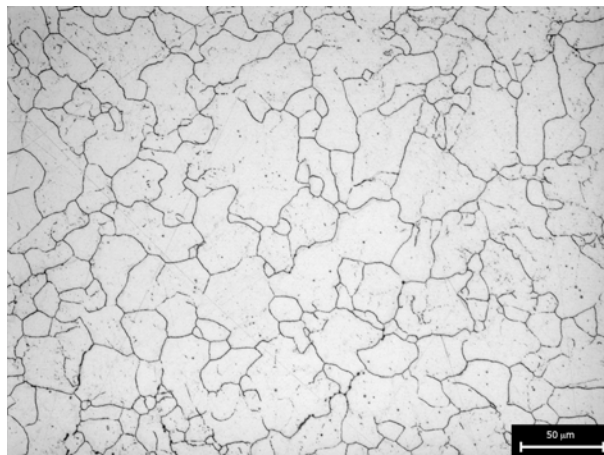


Figure 6.23. Microstructure of ASTM F75 alloy produced by EBM and heat treated for 15 min at 1125 °C (in dilatometer).

As well visible in figure, the microstructure does not seem to be strongly affected by

---

the partial solution treatment at 1125 °C. The measured microhardness of the treated alloy, furthermore, is  $422 \pm 20$  HV<sub>0.05</sub>. With the aim of obtaining a partial dissolution of the intragranular carbides, the material was heat treated at 1137 °C for 15 min, with the same heating and cooling conditions applied in the previous treatments. After this last partial solution treatment, the microstructure underwent a modification, as observable in Figure 6.24.



*Figure 6.24. Microstructure of ASTM F75 alloy produced by EBM and heat treated for 15 min at 1137 °C (in dilatometer).*

Severe grain growth did not affect the material, while the partial solutioning of the interdendritic carbides occurred. For this treated material, the microhardness results to be  $404 \pm 14$  HV<sub>0.05</sub>. Putting the microhardness obtained on the alloy solution treated at 1125 °C and 1137 °C in the graph reported in Figure 6.22, the fitting trend changes (Fig. 6.25). In fact, the trend becomes slightly sigmoidal.

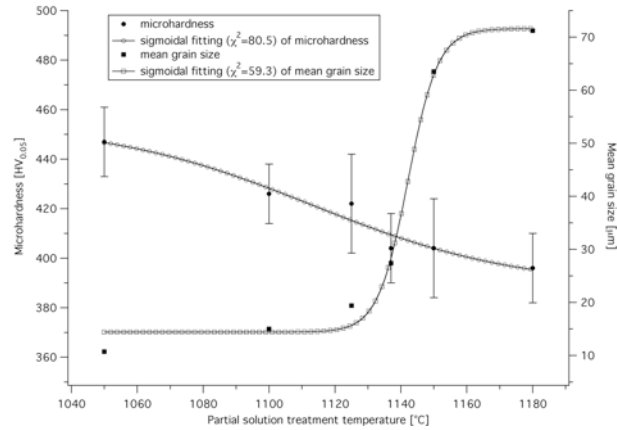


Figure 6.25. Microhardness and average grain size versus treatment temperature for ASTM F75 alloy produced by EBM.

The same but opposite behaviour, even though more pronounced, is registered for the calculated average grain size (Fig. 6.25). On the other hand, the evolution of the austenitic phase presence after the different partial solution treatments follows a different trend, as shown in Figure 6.26: it continuously increases with increasing temperature.

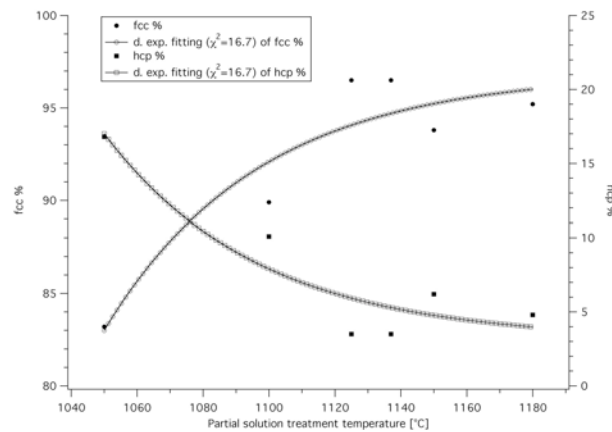
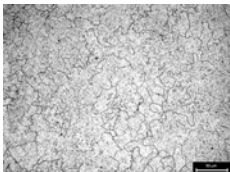
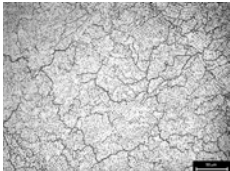
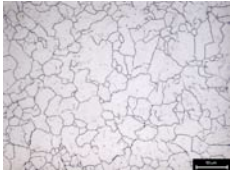
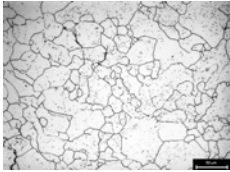
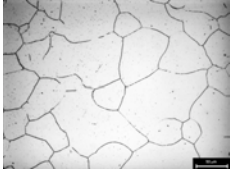


Figure 6.26. Phase composition of alloy versus solution temperature.

Table 6.6. Microhardness, average grain size, fcc percentage and microstructures of ASTM F75 alloy produced by Electron Beam Melting and heat treated in dilatometer at different temperatures.

Treatment temperature [°C]	$\mu\text{HV}$ [ $\text{HV}_{0.05}$ ]	Average grain size [ $\mu\text{m}$ ]	fcc %	Microstructure
1050	447±14	10.7	83.2±1.7	
1100	426±12	15.0	89.9±1.8	
1125	422±20	19.4	96.5±1.9	
1137	404±14	27.4	96.5±1.9	
1150	404±20	63.5	93.8±1.9	
1180	396±14	71.2	95.2±1.9	

At the end of this characterization stage, the temperature of 1137 °C was chosen for

the partial solution treatment. The narrow temperature interval in which the dissolution of the intragranular carbides takes place makes the industrial application of heat treating difficult. Starting from this consideration, the treatments carried out in the dilatometer were repeated in the high vacuum furnace. In particular, the treatments at 1125 °C and 1150 °C for 15 min were repropounded, applying a constant heating rate of 20 °C/min and a calculated cooling rate of 19.7 °C/s (resulting from the forced cooling due to insufflating argon gas at 8 bar). Nevertheless, the alloy resulted different than the expected: no significant solutioning of the intragranular carbides occurred even at 1150 °C (Fig. 6.27).

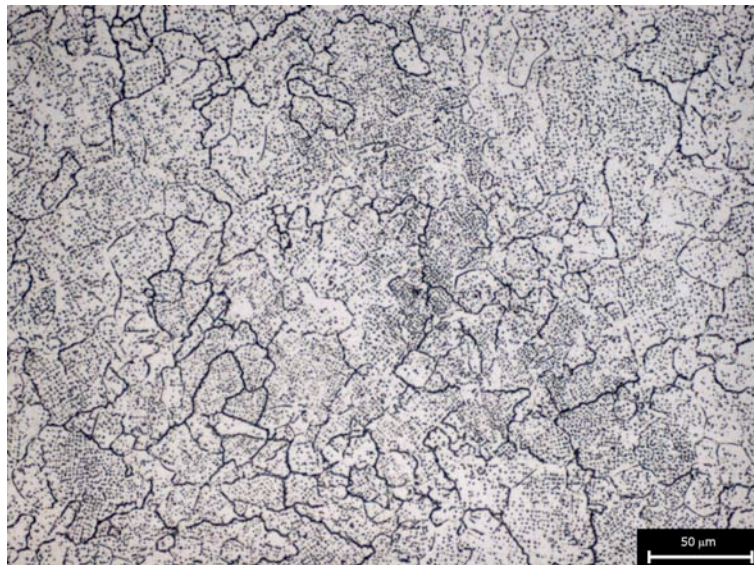


Figure 6.27. Microstructure of ASTM F75 alloy produced by EBM and heat treated for 15 min at 1150 °C (in furnace).

The observed difference put the question of the different temperature perception between dilatometer and furnace. A first hypothesis about this difference regards the possible decarburization of the alloy during the heat treatment in dilatometer, since a partial vacuum atmosphere was there recreated. The Leco analysis on the two samples processed at 1150 °C, however, substantially furnished the same carbon amount. Then, other hypotheses can be put forward. One can be related to the different geometry of the samples. The dilatometric sample, in fact, is significantly smaller than

---

the specimens heat treated in the vacuum furnace. Since the thermal conductivity of the CoCrMo alloys is limited, the temperature distribution along the part can be not homogeneous. However, the temperature in the dilatometer as well as in the furnace was measured through a thermocouple, and this should reduce the risk of misreading. The most probable cause of the difference in temperatures is then ascribable to the controllers of the different systems.

A deepening of the problem required the carrying out of heat treatments so that a trend like those of Figs. 6.25 and 6.26 is obtained also for furnace treatments. Then, solution treatments at furnace temperatures between 1150 °C and 1210 °C, in the same conditions of the previous, were effected, in order to individuate the temperature interval in which the solutioning of the interdendritic carbides takes place. The point is that a difference of 30-40 °C is registered between the treatment temperatures inside the two equipment. Finally, the individuated temperature at which a partial solution occurs is 1170 °C. The microstructure after such a treatment is shown in Figure 6.28.

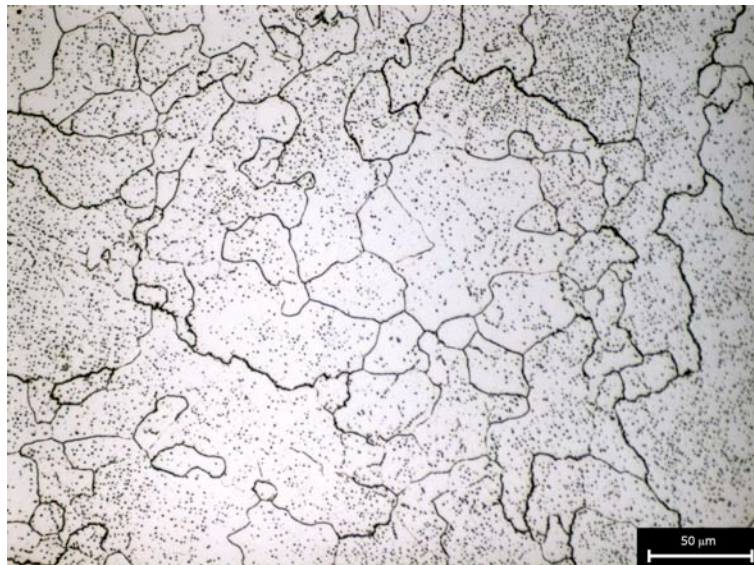


*Figure 6.28. Microstructure of ASTM F75 alloy produced by EBM and heat treated for 15 min at 1170 °C (in furnace).*

As visible in the picture, intragranular carbides are still present after solution treatment

at 1170 °C in furnace, but their amount is reduced. Moreover, the microhardness on the treated alloy is  $404 \pm 11$  HV<sub>0.05</sub>. The matrix is constituted by the 90% of cubic phase and the 10% of hexagonal phase.

Subjected to tensile testing, the material offers the behaviour represented in Figure 6.29 and summarized in Table 6.7.

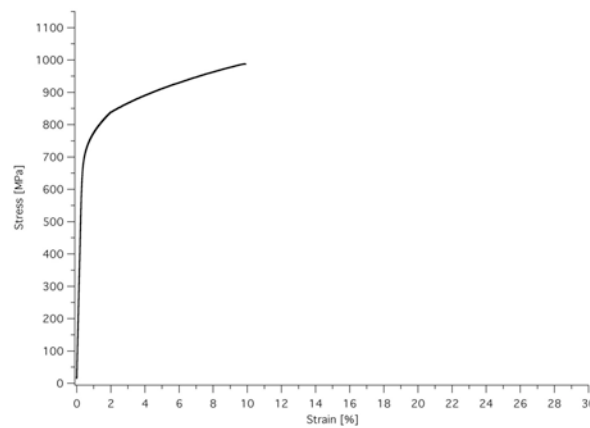


Figure 6.29. Stress-strain curve of ASTM F75 alloy produced by Electron Beam Melting and partially solution annealed at 1170 °C.

Table 6.7. Tensile properties of ASTM F75 alloy produced by Electron Beam Melting (EBM) and partially solution annealed; as-built material's properties, solution annealed material's properties and standard requirements reported.

	partially solution treated	solution treated	as-built	ISO 5832-4
<b>Elastic Modulus [GPa]</b>	209±9	206±1	165±6	-
<b>Yield stress [MPa]</b>	722±1	579±6	719±17	> 450
<b>Ultimate Tensile Strength [MPa]</b>	989±11	1073±25	796±12	> 665
<b>Elongation [%]</b>	9.8±0.8	27.3±1.6	1.0±0.2	> 8

In comparison with the as-built alloy, the partially solution treated material has about the same yield stress. This is noticeable higher than the yield stress of the solution annealed material. Nevertheless, due to the already mentioned strain hardening rate, the Ultimate Tensile Strength of the partially solution treated alloy is considerably

---

higher than the UTS of the as-built alloy. The elongation matches the ISO standard requirements and represents a good compromise between the hardness and brittleness of the as-built material and the softness and ductility of the solution annealed alloy. As previously discussed, the Elastic Modulus can vary depending on the crystallographic orientation (i.e., texture). So, the difference in Elastic Modulus between the two materials can be associated to the different crystallographic features: while texture characterizes the microstructure of the as-built material, the partially solution treated material has equiaxed grains.

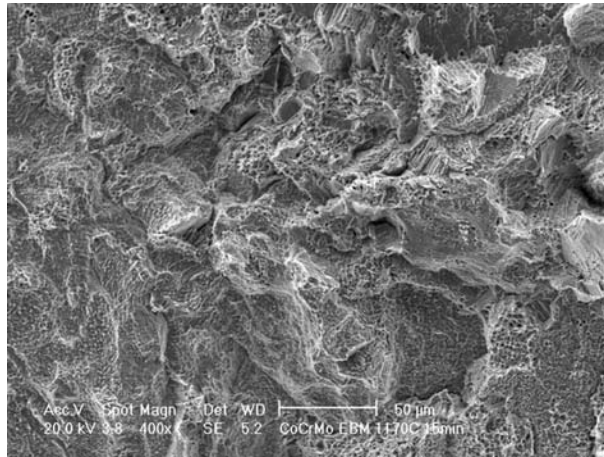


*Figure 6.30. Detail of the fracture surface of ASTM F75 alloy partially solution annealed at 1170 °C; ductile morphology.*

A ductile morphology is observable (Fig. 6.30) on the fracture surface of the broken tensile specimens. Semi-cleavages are also detected. Obviously, this morphology is different from that of the as-built material, but also from the surface of the solution annealed material. The fracture mode rather seems to be a mix of intergranular and transgranular mechanisms, well relatable to the carbide distribution.

## 6.4 Final remarks

CoCrMo ASTM F75 alloy produced by Electron Beam Melting, as well as Ti-6Al-4V

processed by Rapid Manufacturing technologies, has a very peculiar microstructure, due to the characteristics intrinsic of the process itself, such as undercooling.

The as-built material is limited in application because of its poor ductility, imputable to the plenty of intergranular and intragranular (interdendritic) carbides. The microstructure of the as-built material, moreover, is strongly oriented in the building direction, since epitaxial growth takes place during the layer-by-layer process. A typical HIPping treatment improves ductility, but not enough for matching the ISO standard requirements. HIPping is also detrimental for the fatigue endurance, as it causes the formation of embrittling pearlitic constituent at the grain boundaries.

The study of the thermal stability of the EBM alloy is then necessary in order to understand how the mechanical properties can be improved through a microstructural change. Dilatometric tests allow the transformation ranges to be individuated, and in particular the solution interval to be located. The solution annealing of the as-built material strongly improves the ductility of the alloy, but on the other hand it causes an effective reduction in the yield stress. This results to be detrimental for the fatigue resistance. Then, a partial solution treatment had been arranged, in order to obtain both high yield stress and good ductility.

---

## References

- [1] W. Betteridge, "Cobalt and its alloys", E. Horwood Series, 1982
- [2] J.W. Weeton and R.A. Signorelli, *Trans. ASM* 47 (1954) 815
- [3] R.E. Reed-Hill, R. Abbaschian, "Physical metallurgy principles", PWS Publishing Company, 1994
- [4] B. D. Ratner, A.S. Hoffman, F.J. Schoen, J.E. Lemons, "Biomaterials science: an introduction to materials in medicine", San Diego Academic Press, 1996
- [5] L.Z. Zhuang, E.W. Langer, *ESOMAT* (1989) 343
- [6] H.S. Dobbs, J.L.M. Robertson, *J. Mater. Sci.* 18 (1983) 391
- [7] L.Z. Zhuang, E.W. Langer, *Metall. Trans.* 20A (1989) 99
- [8] C. Montero-Ocampo, R. Juarez, A. Salinas Rodriguez, *Metall. Mater. Trans.* 33(7) (2002) 2229
- [9] P. Huang, R. Liu, X. Wu, M.X. Yao, *J. Eng. Mater. Tech.* 129 (2007) 523
- [10] C. Montero-Ocampo, M. Talavera, H. Lopez, *Metall. Mater. Trans.* 30A (1999) 611
- [11] D.C. Ludwigson, J.A. Berger, *J. Iron Steel Inst. London* 207 (1969) 63
- [12] J.R. Low, F Garofalo, *Proc. Soc. Exper. Stress Anahys.* 1947, 44, 16
- [13] D.C. Ludwigson, *Metall. Trans.* 2 (1971) 2825
- [14] X. Tian, Y. Zhang, *Mater. Sci. Eng.* A174 (1994) L1-L3
- [15] Y.G. Kim, C.Y. Lim, *Metal. Trans.* 19A (1988) 1625

## Chapter 7

# 17-4 PH Stainless Steel produced by Selective Laser Melting

### 7.1 Microstructures

As previously stated in Chapter 2, the 17-4 PH (AISI 630) grade is a high chromium martensitic steel. In the range of stainless steel, it is well-known as a trade-off between mechanical strength and wear and corrosion resistance.

Its martensitic microstructure results from the transformation of austenite on cooling and is stabilized by the chemical composition of the alloy. Martensite laths are heavily faulted and contain stacking fault and twinings. Twins are also generated by the strain accommodation between adjacent laths.

Nevertheless, an amount of austenite can be retained. This metastable  $\gamma$  phase, known as reversed austenite, forms along the martensite laths because of the segregation of copper (which is a  $\gamma$  stabilizer) towards the lath boundaries (where copper-rich phases precipitate).

Depending on the cooling rate and possible segregations,  $\delta$ -ferrite can be present as an additional stringer-shaped phase.

The commercial AISI 630 alloy produced by hot working usually undergoes a solution treatment (austenite conditioning) at 1040 °C for a time varying with the part size. Oil quenching, water quenching or even air cooling are then applied. After solutioning, however, the material is not employable, since it is too brittle. Then, an aging treatment (precipitation hardening) for 1-4 h at a temperature between 480 °C (H900 treatment) and 620 °C (H1150 treatment) follows. In some cases a homogenization at 1175 °C can be carried out for more than 2 h before the solution annealing [1]. During the solution treatment, the solutioning of the copper (the hardening element)

---

takes place; then, on cooling, a supersaturated solid solution is obtained. Usually, oil or air quenches are rapid enough to reach this condition. Then, during aging, a sub-microscopic precipitation of Cu compounds occurs. As discussed in Chapter 2, aging temperature and time influence the precipitation stages. As a consequence, the H900 aging results in high hardness but brittleness, while the H1150 allows a good toughness to be obtained, to detriment of hardness. Obviously, many intermediate temperatures can be applied.

The microstructure of the solution annealed material is shown in Figure 7.1.

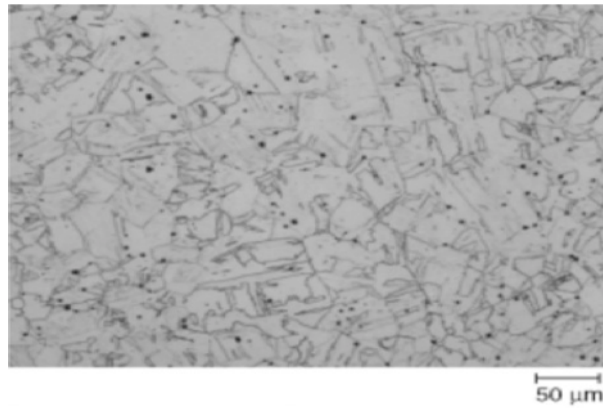


*Figure 7.1. Microstructure of the wrought and solution annealed material.*

The picture evidences the martensitic microstructure resulting from cooling after solution treating.

After an H900 temper, the microstructure appears as in Figure 7.2a. On the other hand an H1150M aging, in which (after annealing) the part is heated up to 760 °C for 2 h, air cooled and then heated up to 620 °C for 4 h, results in the microstructure shown in Figure 7.2b.

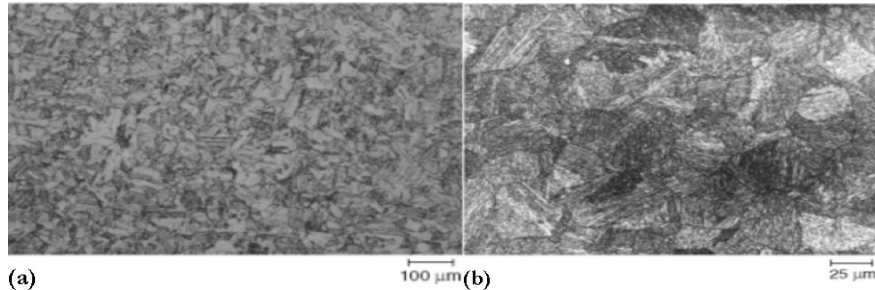


Figure 7.2. Microstructure of the wrought, solution annealed and aged material; (a) H900 condition, (b) H1150M condition.

In the second one, both martensite and reverted austenite are present [2].

Copper precipitates cannot be detected under an optical microscope, since they are sub-microscopic. However, it is here noteworthy to remember that the precipitation of copper compounds only can take place in the martensitic matrix. The solubility of Cu in the austenite, in fact, is higher than the copper amount in the alloy: consequently, Cu in the austenite totally remains in solution.

The microstructure of the 17-4 PH grade produced by Selective Laser Melting is reported in Figure 7.3. The microstructure makes reference to the material after a stress relief treatment carried out at 600 °C for 2 h. The machine producers, in fact, believed these were the best treatment conditions in order to relieve the thermal stresses induced by the process and easily remove the parts from the working plate avoiding deformations and breakings. As a consequence, the material was not in strictly as-built conditions. However, the stress relief treatment was considered part of the process itself.

The microstructure consists of large and oriented grains with a very fine dendritic substructure, which is typical of the SLM process. The microstructure does not contain residual pores.

Some authors [3] called the microstructure obtained by this way a bimodal (duplex) microstructure. Effectively, it is similar to the microstructure shown above (Fig. 7.2b), more than to the martensitic microstructure of Fig. 7.1.

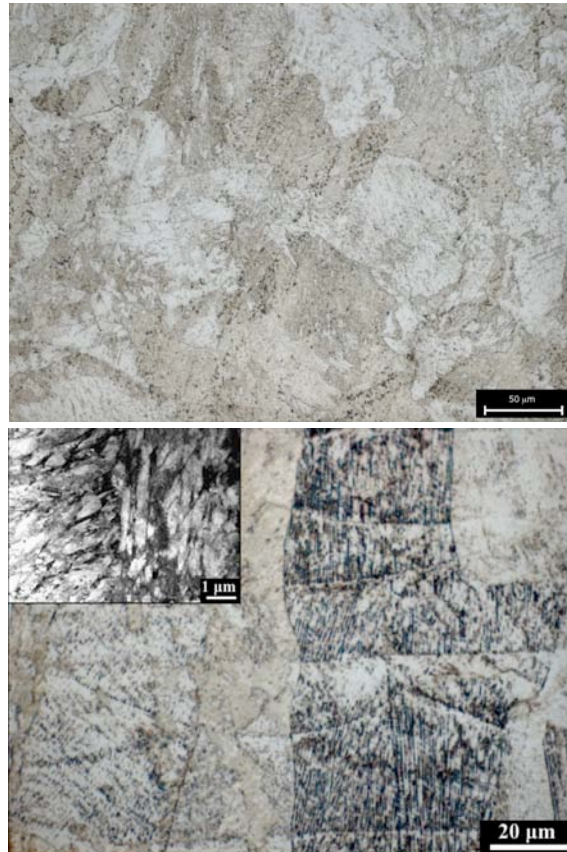


*Figure 7.3. Microstructure of the 17-4 PH grade produced by Selective Laser Melting.*

Some considerations about the process are then necessary. As previously discussed, the severe undercooling, which is a feature of the Selective Laser Melting process, can be responsible for the formation of metastable structures. Then, the material microstructure unlikely can appear as in the common way. However, the material undergoes a heat treatment immediately after the production. Then the point is, at first: is the SLM alloy in a solution treated condition after stress relief? And if not, what is its condition?

Early investigations on the microstructure were carried out by XRD analysis. What this analysis pointed out is that, after the stress relief treatment, the material is mostly austenitic. Only 28% of martensite was indeed noticed. The acquired XRD pattern is shown in Figure 7.4.

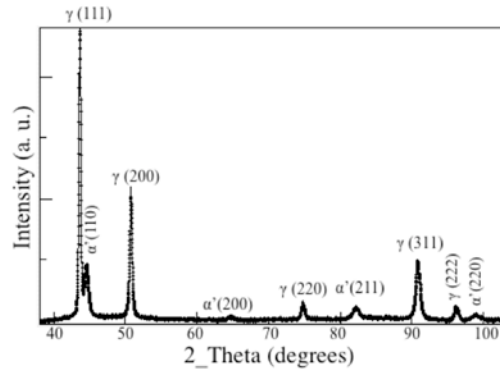


Figure 7.4. XRD pattern acquired on 17-4 PH Stainless Steel produced by Selective Laser Melting and stress relieved at 600 °C for 2 h.

In the TEM bright field image of Figure 7.5, a highly twinned martensite plates and untwinned regions near the martensitic grains with a high density of defects (stacking faults and dislocations) can be individuated. Selected area diffraction pattern of Fig. 7.5c shows retained austenite between martensite plates.

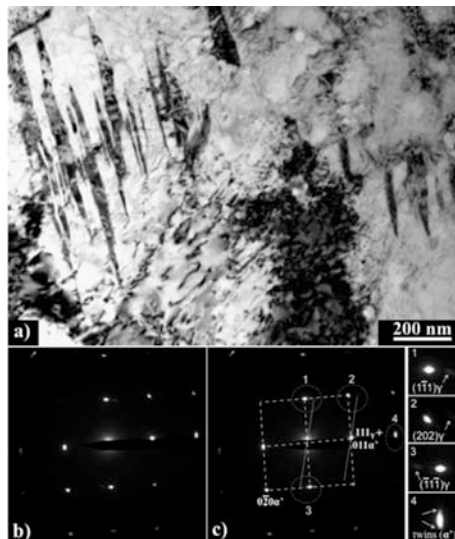


Figure 7.5. TEM bright field image acquired on 17-4 PH Stainless Steel produced by Selective Laser Melting and stress relieved at 600 °C for 2 h; selected area diffraction pattern shows retained austenite between martensite plates.

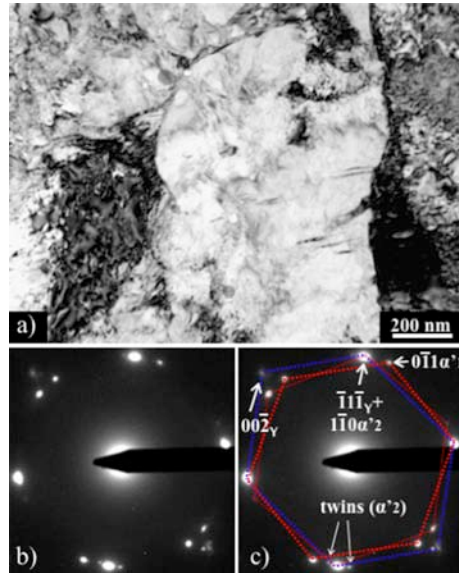


Figure 7.6. TEM bright field image acquired on 17-4 PH Stainless Steel produced by Selective Laser Melting and stress relieved at 600 °C for 2 h; evidences of Kudrjumov-Sachs relationship between austenite and formed martensite are reported.

The orientation relationship between the retained austenite and the formed martensite was found to be compatible to Nishiyama-Wasserman (N-W) relationship [4]. However, evidences of Kudrjumov-Sachs (K-S) relationship between austenite and formed martensite, confirming that the austenite is present in both distinct orientations, are reported in Figure 7.6.

Table 7.1. XRD analysis: crystallite size, microstructural strain, stacking fault probability and dislocation density in the austenite.

(hkl)	Crystallite size [nm]	R.m.s. strain [ $\times 10^3$ ]	$\alpha$ [ $\times 10^{-3}$ ]	$\rho$ [ $\times 10^{15} \text{ m}^{-2}$ ]
111	127(11)	0.00252(6)	$6.2 \pm 0.7$	1.38(15)
200	97(9)	0.00231(7)		
220	108(9)	0.00233(7)		
311	115(10)	0.00214(8)		

Table 7.2. XRD analysis: crystallite size, microstructural strain, twinning probability and dislocation density in the martensite.

(hkl)	Crystallite size [nm]	R.m.s. strain [x10 <sup>3</sup> ]	$\tau$ [x10 <sup>-3</sup> ]	$\rho$ [x10 <sup>16</sup> m <sup>-2</sup> ]
110	118(12)	0.00831(9)	2.1(4)	1.27(14)
200	83(8)	0.00704(12)		
211	81(7)	0.00717(10)		

The results of the elaboration of the XRD patterns of the stress relieved material are reported in Tables 7.1 and 7.2. Both austenite and martensite are nanometric in term of substructure, and the crystallite size does not depend significantly on the crystallographic direction. The austenite contains quite a low density of dislocations ( $1.38 \times 10^{15} \text{ m}^{-2}$ ), but arranged with a high stacking faults probability (about 6%). On the other hand, the martensite contains a larger density of dislocations ( $1.27 \times 10^{16} \text{ m}^{-2}$ ) and also a significant twinning probability (about 2%).

The strain in austenite is due to the thermomechanical stresses accumulated during solidification and cooling down to room temperature in SLM [5], as previously disclosed, as well as to the accommodation of the strain associated to the formation of the martensite.

Since it was not available in literature, SFE of the 17-4 PH steel austenite was calculated from the average electron vacancy number  $\langle NLE \rangle$ . Then, the  $\langle NLE \rangle$  value was obtained through the equation

$$\langle NLE \rangle = [0.61Ni + 4.66(Cr + Mo) + 2.66Fe + 3.66Mn + 6.66Si]/100$$

and then correlated to the SFE following the trend suggested by Reick et al. (Fig. 7.7) [6].

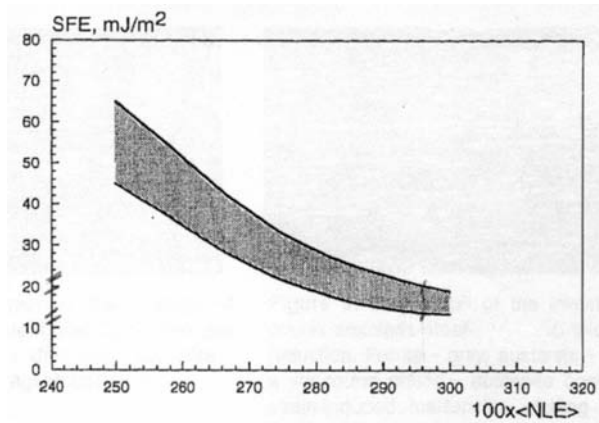


Figure 7.7. Correlation between Stacking Fault Energy and electron vacancy number after Reick *et al.* [6].

Stacking Fault Energy resulted 15-20 mJ/m<sup>2</sup>, but it could be slightly greater since SFE increases with decreasing grain size [7,8]. Such a Stacking Fault Energy is consistent with the large density of stacking fault detected in the austenite. On the other hand, the martensite is highly defective, and contains both twins and dislocations. Usually twinning prevails on dislocation gliding during the formation of martensite plates at low temperature, as in high carbon steels (in which it is due to their low  $M_s$  and  $M_f$  temperatures). Martensite start temperature of 17-4 PH stainless steel is nominally 150 °C, which is consistent with the coexistence of the two deformation mechanisms in martensite.

Under an opportune driving force, the metastable austenite can transform into stable martensite. This driving force can be provided mainly by three ways. Further cooling below room temperature (i.e., towards  $M_f$ ) represents the first way. The second possibility regards mechanical aspects. A strain-induced martensitic transformation can in fact take place during deformation, resulting in the well-known Transformation Induced Plasticity (TRIP) phenomenon. TRIP is exploited in some steel grades, namely the low alloyed Si-Mn steels as well as the high alloyed Mn-Si-Al steels, to improve their plastic ductility in cold forming. TRIP is also displayed by austenitic stainless steels. Its occurrence depends on the Stacking Fault Energy of austenite [6]. On decreasing SFE, deformation occurs by perfect and partial dislocation gliding, by twinning and then by martensitic transformation. When the SFE lies below 15-20

mJ/m<sup>2</sup>, austenite transforms in  $\epsilon$  and  $\alpha'$  martensite, resulting in an increase in strain hardenability and, in turn, in ductility. Finally, heating represents the third way to provide driving force for the transformation. Upon heating, in fact, the strain stabilizing the retained austenite can be relieved, allowing the  $\gamma$ -to- $\alpha'$  transformation to take place.

The discussion concerning the study of the material structure by XRD and TEM is sound, and is confirmed by literature. Nevertheless, an in-depth analysis in transmission allowed the material structure to be better investigated and understood. Neutron diffraction spectroscopy, in fact, evidenced the fully austenitic composition of the bulk material.

So, there is a strong difference between the results of the two diffraction analyses, and a further reflection on this difference becomes necessary. The starting point for such a reflection is the only just discussed metastability of the austenite. Then, two new questions stand up: why is the retained austenite stabilized? What mechanisms are involved?

In principle, the presence of metastable austenite in steels can be due to three possible causes. The first is the very large undercooling, which suppresses the austenite-to-martensite transformation on cooling. In this case, this mechanism can be excluded, since the application of the stress relief treatment after the process should allow the transformation to occur. The second cause is the segregation of solute atoms, according to the mechanism of thermal stabilization occurring between  $M_s$  and  $M_f$  temperatures [9,10]. For certain chemical compositions, in fact, the transformation can be stabilized by isothermal holding, making an additional supercooling necessary in order to start the transformation again [11]. To verify this mechanism, a deep cryogenic treatment was carried out at -196 °C in liquid nitrogen. Since no martensitic transformation was detected after the treatment, also this possibility was excluded. The last possible reason is the presence of a large strain in the austenite. The large undercooling typical of the SLM process, in fact, is related to the formation of thermal stress, as explained in Chapter 1. This stress is associated to the presence of residual strain. Such a strain can be responsible for a mechanism of mechanical stabilization [11,12]. The stabilization of austenite is further enhanced by its nanometric structure, which reduces its ability to accommodate the transformation strain. As a consequence of this explanation, the detection of retained austenite in the 17-4 PH stainless steel produced by SLM becomes strictly related to the features of the process: the presence

---

of the metastable austenite is intrinsic of the process itself.

Concerning the detecting of martensite by XRD analysis, its justification is one more time provided by the discussion on the residual strain. On the external surface, the material earns a degree of freedom in comparison with the bulk. As a consequence, the residual strain close to the surface can be released. Then, the austenite-to-martensite transformation is able to occur; furthermore, the transformation can be helped by the mechanical modification of the surface (i.e., cutting, polishing, etc.). When analyzed by X-Ray Diffraction, the material is investigated in the neighbourhood of the surface: martensite, which is only there present, is found. As stated in Paragraph 4.9, during a neutron diffraction spectroscopy the bulk material is directly analyzed, since the neutrons have a high penetration and then the analysis is carried out in transmission. Then, a more realistic, fully austenitic microstructure is pointed out.

## 7.2 Hardness and tensile properties

The most important mechanical property for the application of the 17-4 PH grade in the production of surgical instruments is hardness. In fact, the steel is employed in the production of surgical instruments, and so it has to be hard in order to be sharpened and keep the edge. Hardness is usually relatable to the tensile properties of the material. In particular, hardness of steels is generally proportional to their Ultimate Tensile Strength.

After the stress relief treatment (2 h at 600 °C), the processed material scores  $27.4 \pm 0.5$  HRC. Because of the discussed presence of the martensitic phase on the surface, the Vickers microhardness measured on the same materials results to be, in proportion, slightly higher than the Rockwell hardness (Tab. 7.3).

Table 7.3. Microhardness of 17-4 PH Stainless Steel produced by Selective Laser Melting and stress relieved at 600 °C for 2 h.

	Vickers microhardness [HV <sub>0.05</sub> ]	converted Rockwell <sup>1</sup> [HRC]	Rockwell hardness [HRC]
<b>Stress-relieved material</b>	304±16	30	27.4±0.5

This can be explained remembering that the microhardness affects a few microns (and then remains tied up to the surface), while the Rockwell hardness deepest penetrates the material. Since the martensitic surface can be slightly harder than the austenitic bulk, the little difference between the theoretical (converted) and the measured Rockwell hardness can be justified.

From the point of view of the tensile properties, the stress-relieved material exhibits the stress-strain curve shown in Figure 7.8.

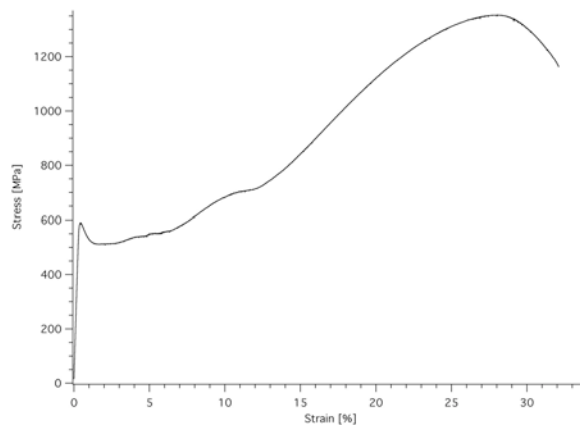


Figure 7.8. Stress-strain curve of 17-4 PH Stainless Steel produced by Selective Laser Melting and stress relieved at 600 °C for 2 h.

<sup>1</sup> Rockwell hardness converted from the measured Vickers microhardness.

Table 7.4. Tensile properties of 17-4 PH Stainless Steel produced by Selective Laser Melting and stress relieved at 600 °C for 2 h; standard references reported for H900 and H1150M aging.

	17-4 PH SLM	ASTM A564M for H900	ASTM A564M for H1150M
<b>Elastic Modulus [GPa]</b>	187±7	-	-
<b>Upper Yield Point [MPa]</b>	590±5	} 1170 <sup>2</sup>	} 520 <sup>2</sup>
<b>Lower Yield Point [MPa]</b>	512±7		
<b>Ultimate Tensile Strength [MPa]</b>	1343±11	1310	795
<b>Elongation [%]</b>	29.0±2.5	10	18

The material yields at 600 MPa (Upper Yield Point). This value is lower than it could be expected from the microhardness. A 5% Lüders deformation at 500 MPa (Lower Yield Point) follows. Such a sharp yield point is typical of alloys possessing a very low content of interstitial elements (but also of nanocrystalline metals; and the studied 17-4 PH grade has a nanometric substructure, as disclosed above). After yielding, a uniform plastic deformation up to 25%, where a fast transition from diffused to localized necking occurs, takes place. The unsteady plastic deformation is poor. Such a plastic deformation behaviour is typical of materials with negative strain rate sensibility (i.e., nanocrystalline materials). The work hardening during the plastic flow is large and carries on up to 1300 MPa. This accounts for the discrepancy between microhardness and yield stress but is, at the same time, in contrast with both the sharp yield point and the very fine structure of the steel. The plastic field has two different subsequent steps: the strain hardening rate decreases nearby 10% of elongation, and then increases again.

The material is characterized by large ductility and high UTS. An increase in toughness due to the presence of retained austenite in a 17-4 PH stainless steel was already reported by Nakagawa and Miyazaki [11]; up to 30% austenite was stabilized in the microstructure by a special heat treatment. However, a mostly austenitic 17-4 PH stainless steels was never been investigated before.

Both the work hardenability and the large density of stacking faults in the austenite are

<sup>2</sup> ASTM A564M standard makes general reference to “Yield Strength” as a single value.

consistent with the TRIP effect, where plasticity is aided by the strain-induced martensitic transformation and then is (in its turn) transformation-induced. Spencer et al. [13] studied the mechanism of the strain-induced martensitic transformation by neutron diffraction experiments in an austenitic 304L stainless steel. The sequence of martensite formation, after Spencer, can be  $\gamma \rightarrow \epsilon \rightarrow \alpha'$  or  $\gamma \rightarrow \alpha'$ . The presence of the stacking faults supports the hypothesis of the transformation from fcc austenite to hcp  $\epsilon$  martensite; then, the intersections between the  $\epsilon$  sheets act as nucleation sites for the transformation  $\epsilon \rightarrow \alpha'$  [14]. No  $\epsilon$  martensite was detected in the present study, likely because of the less amount of Ni in comparison to the 304L stainless steel. However, Spencer observed that after the first transformation step at intersections between  $\epsilon$  sheets, a remarkable quote of  $\alpha'$  phase nucleates directly from austenite. In particular twins, due to the low Stacking Fault Energy of the  $\gamma$  phase, were found to be preferred nucleation sites for  $\gamma \rightarrow \alpha'$  direct transformation. Furthermore, twins result to be more effective sites than grain boundaries in the proceeding of this mechanism.

The strain hardenability not only depends on the transformation, but also on the deformation mechanisms of the untransformed austenite and martensite. This aspect of the question was in a first time deepened by an XRD analysis of the material before and after the uniform plastic deformation. So, two tensile samples where elongated up to 8% and 23% of strain, respectively, and then unloaded and analyzed by X-Ray Diffraction. Part of the obtained results is reported in Figure 7.9.

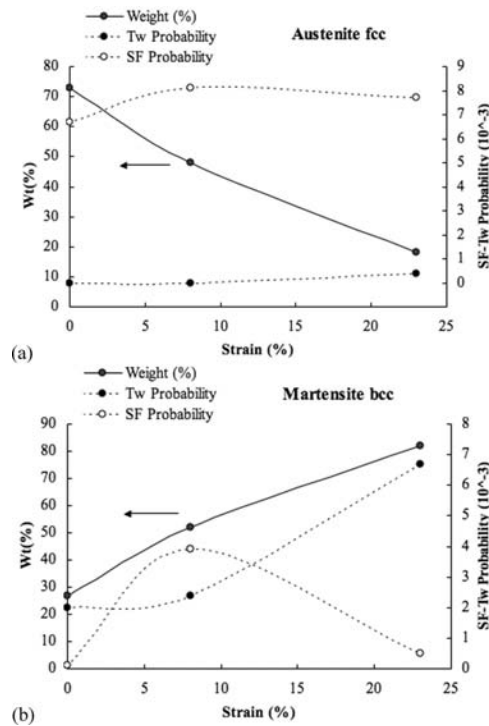


Figure 7.9. XRD analysis: twinning (Tw) and stacking faults (SF) probability in untransformed austenite (a) and martensite (b) vs. plastic strain. The solid and dashed lines are guidance for eyes.

Figure 7.9a shows that untransformed austenite accumulates stacking faults in the first plastic step (up to 8% strain), with a slight transition to twinning in the second step. Martensite (Fig. 7.9b) shows the same trend, with the transition from stacking faults accumulation to twinning accentuated. The low twinning probability in austenite may be explained as a rapid nucleation of the martensite plates within the high twinned austenitic regions, which accounts for the continuous strain-induced transformation along the whole plastic field. On the other side, accumulation of twins in martensite enhances its resistance to plastic flow and provides an additional contribution to the increase in strain hardenability in the second step.

The *in-situ* data collecting confirmed the outlined trends. Figure 7.10 shows the evolution of the strain-induced transformation during loading. As evidenced, martensite starts to form already in the elastic step. The transformation rate decreases around 5% of elongation (i.e., where the specimen begins to plastically deform) and

then increases again.

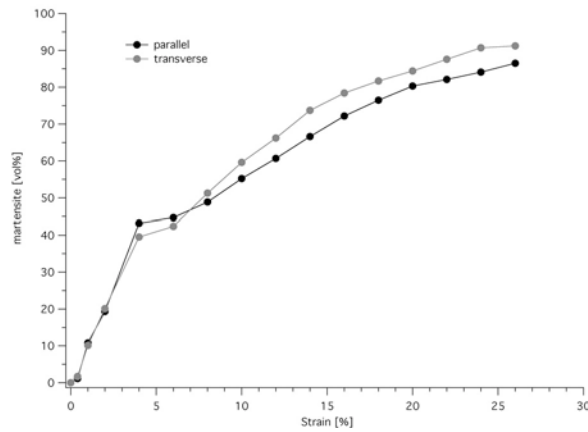


Figure 7.10. SMART: evolution of the strain-induced martensitic transformation on loading.

The stacking fault (SF) probability of the austenitic phase continuously increases, while its twinning probability remains below 1% (Fig. 7.11). On the contrary, the SF probability of the forming martensite roughly decreases after 10% of elongation, where (contemporarily) the twinning probability rapidly increases. The sudden change in the defect probabilities of  $\alpha'$  takes place to coincide with the change in strain hardening rate. Such a change is in accordance with the faulting sequence during deformation (i.e., twins form in correspondence with large dislocation pile-ups). The obtained values of transformed martensite amount, stacking fault probability and twinning probability for both the phases during deformation are summarized in Table 7.5.

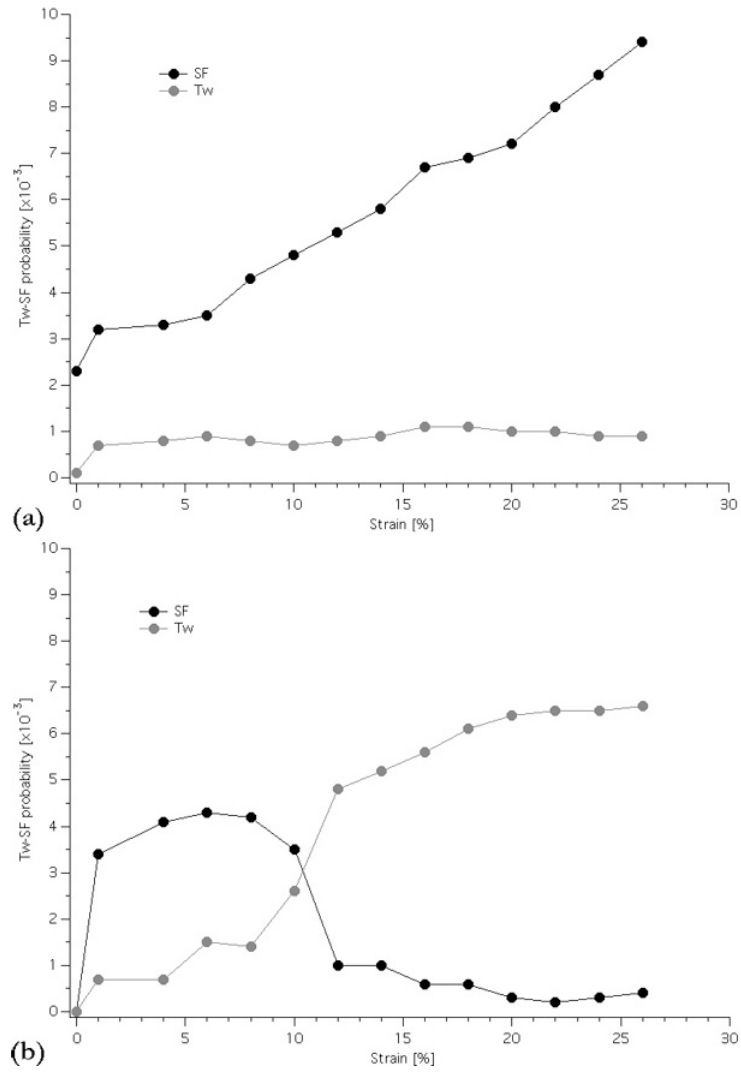


Figure 7.11. SMARTS: twinning (Tw) and stacking faults (SF) probability in untransformed austenite (a) and martensite (b) vs. plastic strain.

Table 7.5. SMARTS: amount of martensite, austenite and martensite faulting of 17-4 PH Stainless Steel on loading.

Strain [%]	Transf. martensite		Austenite		Martensite	
	parallel	transverse	$\alpha$ [ $\times 10^{-3}$ ]	$\tau$ [ $\times 10^{-3}$ ]	$\alpha$ [ $\times 10^{-3}$ ]	$\tau$ [ $\times 10^{-3}$ ]
0.0	0.0	0.0	2.3(2)	0.1(2)	0.0(0)	0.0(0)
0.4	1.1(3)	1.7(2)	-	-	-	-
1.0	10.8(2)	10.1(3)	3.2(3)	0.7(2)	3.4(3)	0.7(2)
2.0	19.3(4)	20.1(3)	-	-	-	-
4.0	43.2(5)	39.5(4)	3.3(3)	0.8(2)	4.1(3)	0.7(2)
6.0	44.7(5)	42.4(5)	3.5(4)	0.9(3)	4.3(4)	1.5(2)
8.0	48.9(4)	51.3(4)	4.3(3)	0.8(2)	4.2(3)	1.4(1)
10.0	55.2(4)	59.6(6)	4.8(4)	0.7(3)	3.5(3)	2.6(2)
12.0	60.7(5)	66.2(5)	5.3(5)	0.8(3)	1.0(2)	4.8(3)
14.0	66.6(5)	73.7(6)	5.8(4)	0.9(2)	1.0(2)	5.2(3)
16.0	72.2(6)	78.4(6)	6.7(5)	1.1(2)	0.6(3)	5.6(4)
18.0	76.5(5)	81.7(5)	6.9(5)	1.1(2)	0.6(2)	6.1(4)
20.0	80.3(6)	84.4(6)	7.2(6)	1.0(3)	0.3(2)	6.4(3)
22.0	82.1(6)	87.6(7)	8.0(5)	1.0(2)	0.2(2)	6.5(4)
24.0	84.1(5)	90.7(6)	8.7(6)	0.9(2)	0.3(2)	6.5(5)
26.0	86.5(5)	91.2(6)	9.4(6)	0.9(2)	0.4(2)	6.6(4)

Concerning the poor unsteady plastic deformation of the material, some considerations about austenite can be done. Bhadeshia, in fact, observed [15] that the failure of nanostructured steels undergoing a TRIP mechanism occurs when the austenite becomes geometrically isolated between martensite plates, i.e. when its amount falls below a certain percolation threshold. Such an explanation seems to be applicable to the present case.

In the attempt of combine the stress relief in the as-built material with an energy saving, the machine producers have tweaked the previously mentioned heat treatment at 600 °C for 2 h. However, they operated with the only aim of avoiding damages on removing the parts from the working plate. Nevertheless, taking a step forward, a heat

---

treatment can be conceived: a new heat treatment after which the material is both stress relieved and solution annealed (i.e., its microstructure is martensitic). The second condition, in fact, is crucial in order to directly age harden the material after the removal of the parts from the working plate.

Using the neutron diffraction spectroscopy, a study of the thermal stability of the as-built material was carried out. The steel underwent a heating up to 750 °C (and then up to the austenitic field) and a following air cooling. No transformation was observed neither on heating, nor on cooling, down to 100 °C. Below this temperature, martensite started to form, and the transformation went on down to the room temperature, even if the cooling rate was really slow. Martensite begins to form at 69 °C and its amount at 30 °C is 75.2% (Tab. 7.6). The same effect is represented in Fig. 7.12 where, on varying temperature, the peak intensity variations for austenite and martensite are reported. The change in the intensity of the lines makes account of the change in phase amounts.

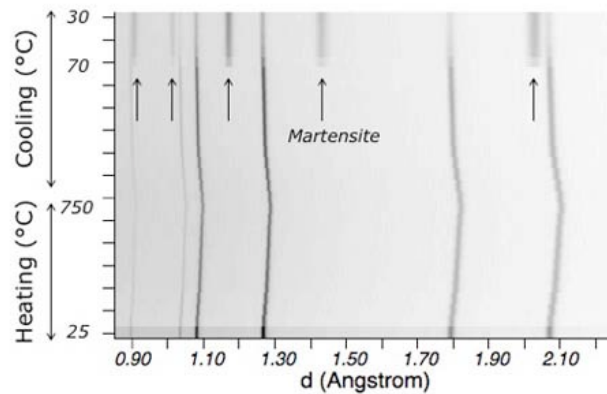


Figure 7.12. Variation of the phase amounts during heating and cooling: martensite begins to form on cooling at 69 °C. Deformation of the peaks is due to change in cell parameter associated to the temperature change.

Table 7.6. SMARTS: amount of martensite forming on cooling in 17-4 PH Stainless Steel produced by Selective Laser Melting; in-situ analysis.

Temperature [°C]	martensite %
100	0
90	0
80	0
70	28.3(2)
60	59.7(4)
50	67.7(4)
40	72.1(5)
30	75.2(5)

The taking-place of the transformation was associated to the destabilization of the metastable austenite. This destabilization occurred when the material was heated up nearby the austenitic field. References about this subject are reported in literature. Commonly, in fact, the austenite destabilization is carried out when a retained austenite must be transformed into martensite, e.g. in high-chromium white irons [16,17,1]. Usually, as just disclosed, it consists in a heat treatment in the neighbourhood of the austenitic field. The bcc to fcc transformation of the 17-4 PH grade is positioned around 700 °C. Since a treatment of 2 h at 600 °C turned out ineffectual from the point of view of the martensite formation on cooling, only a heat treatment above this temperature can be effective for the destabilization of the austenite. Then, the material was at first heated (at a rate of 15 °C/min) up to 750 °C in the TAV furnace, and then cooled with a 2 bar Ar pressure (condition AC0). This temperature was chosen since it falls in the austenitic field and is the same reached during the *in-situ* neutron diffraction. An XRD analysis carried out on the material thus treated gave back an austenite amount of  $64.9 \pm 0.9\%$ . Evidently, austenite started to destabilize, but the treatment was not enough to obtain a fully martensitic microstructure on cooling. Actually, such a treatment cannot reproduced the SMART conditions, since in neutron diffraction spectroscopy, during the data acquiring, the material stands at the acquisition temperature for tens of minutes: this is not, really, direct heating and cooling between RT and 750 °C. As a consequence, an isothermal step in temperature was applied. A second heat treatment was then carried out, in the

same just mentioned conditions, stopping at 750 °C for 2 h (condition AC1). After this, the amount of retained austenite fell down to  $13.2\pm 0.4\%$ , and the improvement in hardness was significant (Tab. 7.7). In the reference condition A (i.e., wrought alloy after solution annealing), the 17-4 PH Stainless Steel usually has a Rockwell hardness of 35-38 HRC, mainly depending on the very fine substructure size. Then, in the AC1 condition the alloy has features comparable with those of the classical solution annealed material. In order to evaluate the trend of the retained austenite with the temperature, two other temperatures were chosen for the austenite conditioning: 780 °C (condition AC2) and 800 °C (condition AC3).

*Table 7.7. Amount of austenite and hardness of 17-4 PH Stainless Steel produced by Selective Laser Melting and stress relieved at different conditions.*

	<b>Treatment temperature [°C]</b>	<b>Treatment time [min]</b>	<b>fcc %</b>	<b>Hardness [HRC]</b>
<b>AC0</b>	750	-	$64.9\pm 0.9$	$24.4\pm 0.5$
<b>AC1</b>	750	120	$13.2\pm 0.4$	$39.1\pm 0.6$
<b>AC2</b>	780	120	$15.3\pm 0.3$	$40.1\pm 0.5$
<b>AC3</b>	800	120	$13.7\pm 0.3$	$39.3\pm 0.3$

It is evident that, even if the treating temperature increases, no further martensite can form on cooling. This can be interpreted with reference to the martensite finish temperature. If the position of  $M_f$ , in fact, is below the room temperature, the martensitic transformation cannot completely run out. The martensite finish temperature lowering is attributed to the constraining effect of the strains induced by the martensitic displacive transformation [15]. The same effect was observed after the *in-situ* analysis carried out on cooling on the as-built material (Tab. 7.6).

The hardness of the material in the AC0 condition is slightly lower than that of the material heat treated at 600 °C for 2 h (Tab. 7.7), even if an amount of martensite has formed. Evidently, the effect of the martensite is less effective than the recovery of the defects.

The solution annealing, however, is the first step in the direction of the alloy hardening. The following is, as stated above, the precipitation of Cu during the martensite aging. Consequently, two aging treatments were applied at each and every of the conditioned samples: H900 and H1150. The obtained Rockwell hardness is

summarized in Table 7.9.

*Table 7.8. H900 and H1150 aging conditions.*

	Treatment temperature [°C]	Treatment time [min]
<b>H900</b>	480	1
<b>H1150</b>	620	4

*Table 7.9. Hardness of 17-4 PH Stainless Steel produced by Selective Laser Melting after stress relieving and aging.*

	H900	H1150
<b>AC0</b>	24.0±0.5	27.3±0.2
<b>AC1</b>	43.3±0.2	37.9±0.2
<b>AC2</b>	44.7±0.2	36.6±0.4
<b>AC3</b>	44.0±0.6	35.9±0.2
<b>ASTM A564M</b>	40	28

The hardness values after an H900 treatment are very high for AC1-AC3 conditions. They are furthermore combined with the presence of an amount of austenite. This can result in interesting toughness.

It is noteworthy to point out that the austenite conditioning is typical of Precipitation Hardening Stainless Steels such as 17-7 PH, in which an austenitic structure is obtained after solution treating (at 1040 °C) and water quenching [18]. This conditioning can be brought into effect by different ways. The first (condition T) is heating up to 760 °C: carbides precipitate, unbalancing the austenite and then making it transform into martensite upon cooling to a temperature below 15 °C; the second (condition R) consists in heating to a higher temperature (925 °C), at which the precipitation of fewer carbides occurs, and the martensite forms by cooling to room temperature and then refrigerating at -75 °C. After conditioning, the alloy is usually aged at a temperature between 480 °C and 620 °C. In the 17-7 PH grade, the austenite is stabilized by the amount of nickel, which is a g stabilizer; in the 17-4 PH produced by SLM, on the other hand, the residual strain induced by the large undercooling is responsible for the retention of the austenite. Nevertheless, after the stabilization, the

---

conditioning operates quite in the same conditions for both the alloys.

### 7.3 Final remarks

The 17-4 PH Stainless Steel produced by Selective Laser Melting is characterized by a microstructure containing large and oriented grains and a very fine dendritic substructure. Analyzed by neutron diffraction spectroscopy, such a microstructure results to be fully austenitic. After a heat treatment of 2 h at 600 °C, carried out with the aim of relieving the residual stress, austenite is still the only present phase. The austenite is stabilized through the strain induced by the large undercooling characterizing the process. However, an amount of martensite forms on the surface, since the residual strain close to the surface can be released.

The presence of the retained austenite allows a TRIP mechanism to take place during the tensile deformation of the material. Actually, the stress-strain curve of the stress-relieved alloy has a very peculiar behaviour. In particular, it is distinguished by the presence of sharp yield point and by significant strain hardenability (due to the strain-induced martensitic transformation). In this condition, the material is ideal for mechanical applications in which resistance to overloading is required. In fact, the alloy early begins to yield, undergoing a 5% deformation below 600 MPa; then, it is able to store a large amount of energy up to 1300 MPa.

However, the stress-relieved material cannot be hardened. Precipitation hardening involving copper, in fact, can only take place in a martensitic matrix (since Cu solubility in the austenite is higher than its amount in the alloy). Since hardness is the most important requirement for the application of the alloy in the biomedical field (i.e., for the production of surgical instruments), a heat treatment able to make the martensitic transformation effective on cooling had been studied. Based on an in-situ analysis, three temperature above 700 °C have been chosen. Heat treatments for 2 h at 700 °C, 780 °C and 800 °C on the as-built material guarantee the obtaining of both stress relieving and martensitic transformation. After them, aging produces the required hardness.

## References

- [1] *ASM Metals Handbook*, 9th ed., American Society for Metals, Metals Park, Ohio 44073, Vol. 4, 1985
- [2] *ASM Metals Handbook*, 9th ed., American Society for Metals, Metals Park, Ohio 44073, Vol. 9, 1985
- [3] M. Shellabear, “IUM 2007 Heat treatment of EOSINT M parts”, EOS e-Manufacturing solutions
- [4] Z. Lu, R. G. Faulkner and T. S. Morgan, *J. Nucl. Mater.* 382 (2008) 223
- [5] S. Allain, J.P. Chateau, O. Bouaziz, S. Migot, N. Guelton, *Mater. Sci. Eng.* 387-389A (2004) 158
- [6] W. Reick, M. Pohl, A.F. Padilha, *Steel Res.* 67 (1996) 253
- [7] P.Y. Volosevich, V.N. Gridnev, Y.N. Petrov, *Phys. Met. and Metallography* 42 (1976) 126
- [8] Kocks, H. Mecking, *Prog. Mater. Sci.* 48 (2003) 171
- [9] R.E. Reed-Hill, R. Abbaschian, “Physical metallurgy principles”, PWS Publishing Company, 1994
- [10] P.P. Sinha, D. Sivakumar, S. Babu, K.T. Tharian, A. Natarajan, *Steel Res.* 66 (1995) 490
- [11] H. Nakagawa, T. Miyazaki, *J. Mater. Sci.* 1999, 34, 3901
- [12] S. Chatterije et al., *Mat. Sci. Tech.* 22(6) (2006) 641
- [13] K. Spencer, M. Véron, K. Yu-Zhang, J.D. Embury, *Mat. Sci. Tech.* 25 (2009) 7
- [14] K. Spencer, J.D. Embury, K.T. Conlon, M. Véron, Y. Bréchet, *Mater. Sci. Eng.* 387-389A (2004) 873
- [15] H.K.D.H. Bhadeshia, *Mater. Sci. Eng.* 481-482A (2008) 36
- [16] A.E. Karantzalis, A. Lekatou, and H. Mavros, *Journal of Materials Engineering and Performance*, 18(2) (2009) 174
- [17] H.S. Yang, J. Wang, B.L. Shen, H.H. Liu, S.J. Gao, S.J. Huang, *Wear* 261 (2006) 1150
- [18] *ASM Metals Handbook*, 9th ed., American Society for Metals, Metals Park, Ohio 44073, Vol. 1, 1985

## Conclusions

The present Ph.D. work, developed on the basis of a collaboration with Eurocoating s.p.a., regarded the study of three alloys (Ti-6Al-4V, ASTM F75, 17-4 PH stainless steel) produced by two Rapid Manufacturing technologies (Electron Beam Melting, EBM, and Selective Laser Melting, SLM).

Within the period of its carrying out, at first, the microstructural and mechanical characterization of the as-built materials has been performed. This characterization allowed some critical features, mainly concerning microstructure and ductility, to be highlighted. In a second time, consequently, in order to address the evidenced issues, an in-depth study of the behaviour of the alloys on heat treatment has been carried out.

The obtained results can be summarized as follows.

### **On Ti-6Al-4V alloy**

Ti grade 5 alloy produced either by Selective Laser Melting and Electron Beam Melting has been studied. In both the cases, the microstructure results to be very fine: biphasic for EBM (Fig. 5.2), monophasic (martensitic) for SLM (Fig. 5.5). These microstructures are associated to the mechanical properties reported in the following table (together with the properties of wrought and annealed material and the standard requirements).

	EBM	SLM	wrought and annealed	ISO 5832-3
<b>Elastic Modulus [GPa]</b>	118±5	112±2	104±2	-
<b>Yield stress [MPa]</b>	830±7	1005±7	790±17	> 780
<b>Ultimate Tensile Strength [MPa]</b>	914±10	1166±3	872±7	> 860
<b>Elongation [%]</b>	13.1±0.4	8.9±0.2	18.1±0.8	> 10
<b>Limit at 50% of resistance probability [MPa]</b>	391±21	381±27	445±7	-

The microstructures characterizing the as-built materials do not satisfy the requirements of the ISO 5832-3 standard. Moreover, the ductility of the alloy produced by SLM does not match the prescription of the standard. Nevertheless, the microstructure and the tensile properties can be changed by heat treating the as-built grades.

When heat treated at 950 °C for 30 min, the Ti-6Al-4V alloy produced by Selective Laser Melting undergoes a significant modification: its microstructure becomes biphasic, with coarser columnar  $\alpha$ -phase crystals formed at the boundaries of the original martensitic plates and an  $\alpha+\beta$  mixture within. After this treatment, the strength of the material is reduced, but contemporarily the elongation to fracture reaches the 12.2±0.2%. Because of the microstructural evolution, the fatigue limit slightly increases, too. Even the Ti-6Al-4V grade produced by Electron Beam Melting undergoes a microstructural coarsening and a fatigue-life improvement on heating. Besides, after heat treatment the microstructures still do not satisfy the standard requirements. The references, in fact, are mainly  $\alpha$ -globular rather than fine lamellar. Such microstructures result from hot working processes, in which dynamic recrystallization is promoted by deformation. The role of the stored strain in the microstructural evolution, indeed, is discussed in Chapter 5. Nevertheless, the mechanism cannot be applied in a near-net shape process. Consequently, the very fine microstructures remain an intrinsic feature of the RM techniques. It may be concluded that the microstructures of the Ti-6Al-4V alloys produced by EBM and SLM, related to good mechanical properties, have to be received by the international standard community.

---

Future work on Ti-6Al-4V alloy produced by Rapid Manufacturing should regard the deepening of the aspects concerning fatigue crack nucleation and propagation. The peculiarity of the microstructures obtained by EBM and SLM, in fact, can be reflected on the resistance to crack nucleation as well as on the propagation behaviour of short cracks and long cracks. A deeper comparing between the fatigue crack responses related to the microstructures obtained by RM (i.e., fine and acicular) and to the traditional (globular or lamellar) microstructures could reveal interesting results. Moreover, the corrosion resistance of the alloy is also related to the microstructure and its phase composition. Standard potentiostatic testing (according to the ISO 16428 and ISO 16429 standards) as well as *ad hoc* testing (e.g., taking into account particular surface topographies) can be carried out.

## On ASTM F75 alloy

As well as Ti-6Al-4V processed by RM technologies, the CoCrMo ASTM F75 alloy produced by Electron Beam Melting is characterized by a peculiar microstructure. This is strongly oriented in the building direction and affected by the presence of largely diffused intergranular and interdendritic carbides (Fig. 6.4). The mechanical properties of the material in the as-built condition are unsatisfactory, since the fracture occurred just above the yield point and no plastic flow is observable. A HIPping treatment improves ductility, but not enough for matching the ISO standard requirements. Moreover, HIPping has a negative effect on the fatigue endurance, as shown in the table below.

	as-built	hipped	ISO 5832-4
<b>Elastic Modulus [GPa]</b>	165±6	190±7	-
<b>Yield stress [MPa]</b>	719±17	545±5	> 450
<b>Ultimate Tensile Strength [MPa]</b>	796±12	812±17	> 665
<b>Elongation [%]</b>	1.0±0.2	7.0±1.1	> 8
<b>Limit at 50% of resistance probability [MPa]</b>	308±25	241±14	-

Even in the case of ASTM F75 alloy, the study of its thermal stability has been useful for understanding how the microstructure can change, and how the mechanical properties can be affected by the microstructural evolution. The results of this study are reported in Chapter 6. The solution annealing of the as-built material strongly improves its ductility; nevertheless, it causes a significant reduction in the yield stress. These tensile properties are suited for mechanical components rather than biomedical parts; moreover, the reduction in the yield stress can be detrimental for the fatigue resistance. Then, a partial solution treatment has been arranged. After this, a very good combination of yield stress and ductility is obtained.

	<b>partially solution treated</b>	<b>solution treated</b>
<b>Elastic Modulus [GPa]</b>	209±9	206±1
<b>Yield stress [MPa]</b>	722±1	579±6
<b>Ultimate Tensile Strength [MPa]</b>	989±11	1073±25
<b>Elongation [%]</b>	9.8±0.8	27.3±1.6

The future objective of the work on ASTM F75 alloy produced by Electron Beam Melting is the verification of the fatigue properties of the alloy after the partial solution treatment, in order to correlate them with the tensile response of the material.

## On 17-4 PH Stainless Steel

The characterization of the studied 17-4 PH grade produced by Selective Laser Melting pointed out very peculiar mechanical properties and microstructural features. First of all, the alloy is austenitic rather than martensitic (contrary to what might be expected), since the austenite is stabilized by the large undercooling characterizing SLM. After a heat treatment of 2 h at 600 °C, performed in order to relieve the residual stress and avoid damages in the removing of the parts from the working plate, the material presents (i) sharp yield point, (ii) uniform plastic deformation up to 25% and 1300 MPa and (iii) poor unsteady plastic deformation. Its tensile properties are summarized in the following table (with a reference to two limit conditions after aging

from ASTM A564M standard).

	17-4 PH SLM	ASTM A564M for H900	ASTM A564M for H1150M
<b>Elastic Modulus [GPa]</b>	187±7	-	-
<b>Upper Yield Point [MPa]</b>	590±5	}1170 <sup>1</sup>	}520 <sup>2</sup>
<b>Lower Yield Point [MPa]</b>	512±7		
<b>Ultimate Tensile Strength [MPa]</b>	1343±11	1310	795
<b>Elongation [%]</b>	29.0±2.5	10	18

The plastic field of the stress-strain curve has two different subsequent steps: the strain hardening rate decreases nearby 10% of elongation, and then increases again. The work hardening is large. Since even in the stress-relieved condition the steel is fully austenitic, such a particular strain hardenability is related to a strain-induced martensitic transformation mechanism. However, the strain hardenability not only depends on the strain-induced transformation, but also on the deformation mechanisms of the untransformed austenite and martensite.

The noticed tensile properties are very interesting in terms of resistance to overloading and shock absorption; nevertheless, after the heat treatment at 600 °C for 2h the hardness of the material is poor. Commonly, in fact, the alloy is hardened by solution annealing (after which a supersaturated martensite is obtained) and aging (during which the precipitation of Cu compounds takes place). Copper, which is responsible for hardening, can only precipitate in the martensite, since its solubility in the austenite is high: then, no precipitation occurs in the austenitic material. The noticed low hardness, unfortunately, is unsuited for employing the material in the production of surgical instruments. Then an alternative heat treatment, able to induce the formation of martensite on cooling, had to be studied. Since an in-situ analysis demonstrated the formation of supersaturated martensite on cooling after a heating in the austenitic field (above 700 °C), finally a treatment of 2 h at 780 °C has been chosen for combining the stress relieving with the martensitic transformation. An

<sup>1</sup> ASTM A564M standard makes general reference to “Yield Strength” as a single value.

H900 aging after this treatment improves the hardness up to 45 HRC. Even if the 17-4 PH Stainless Steel is traditionally employed for applications in which its high hardness is exalted, the properties of the steel produced by SLM open new perspectives. The material, in fact, is able to store a large quantity of energy by deformation, resulting in a high resistance to overloading and a noteworthy damping and shock absorption capability. New applications have to be thought.



## Congresses

**National congress of the Società Italiana di Biomateriali;** Bologna (Italy), May 28th-29th, 2007. “Mechanical and microstructural characterization of Ti-6Al-4V biomedical parts produced by electron beam melting”. Oral presentation.

**European congress of the European Society for Biomaterials;** Brighton (UK), September 9th-13th, 2007. “Microstructural and mechanical characterization of Ti-6Al-4V biomedical components produced by electron beam melting”. Oral presentation.

**8th World Biomaterials Congress;** Amsterdam (The Netherlands), May 28th-June 1st, 2008. “Mechanical properties and microstructural features of CoCrMo alloys produced by Electron Beam Melting for biomedical components”. Poster presentation.

**PM 2008 World Congress;** Washington D.C. (U.S.A.), June 8th-12th, 2008. “Mechanical properties and microstructural features of biomedical components produced by Electron Beam Melting of CoCrMo powders”. Oral presentation.

**16th congress of the European Society of Biomechanics;** Luzern (Switzerland), July 6th-9th, 2008. “Mechanical and microstructural characterization of ASTM F75 alloy produced by Selective Laser Melting”. Oral presentation.

**32nd AIM national congress;** Ferrara (Italy), September 24th-26th, 2008. “Microstruttura e proprietà meccaniche della lega biomedica Ti-6Al-4V prodotta per Selective Laser Melting”. Oral presentation.

**World of Photonics 2009 congress - application panels;** Munich, June 17th, 2009.  
“Selective Laser Melting and Electron Beam Melting of Ti-6Al-4V alloy: microstructural features and thermal stability. A comparison.”. Oral presentation.

## Publications

S. Libardi, M. Leoni, L. Facchini, M. D’Incau, P. Scardi, A. Molinari; “Effect of the dispersion of nanometric silica particles on the thermal stability of a nanostructured iron based powder”, *Mater. Sci. Eng.* 445-446A (2007) 244

L. Facchini, E. Magalini, P. Robotti, A. Molinari; “Microstructure and mechanical properties of Ti-6Al-4V produced by Electron Beam Melting of pre-alloyed powders”, *Rapid Prototyping J.* 15(3) (2009) 171

L. Facchini, S. Hoeges, E. Magalini, P. Robotti, K. Wissenbach, A. Molinari; “Ductility of a Ti-6Al-4V alloy produced by Selective Laser Melting of prealloyed powders”, *Rapid Prototyping J.*, in press

L. Facchini, N. Vicente Jr., I. Lonardelli, E. Magalini, P. Robotti, A. Molinari; “Metastable austenite in 17-4 Precipitation Hardening stainless steel produced by Selective Laser Melting of powders and its effect on tensile properties”, *Adv. Eng. Mater.*, in press



## **Acknowledgements**

A thought to Pierfrancesco, Emanuele and the Eurocoating team.

A thought to Alberto and Stefano: my reference and my mentor, respectively.

A thought to Simone and Andrea, my good fellows.

A thought to my colleagues.

A thought to Andrea, Renata, Matteo: my home.

A thought to the friends of mine: in Trento, in Padova, or even in Portugal! A thought to my companions. A thought to Chiara.

A thought like a plume.

